



TECHNISCHE
UNIVERSITÄT
WIEN

Vienna University of Technology

DISSERTATION

Approach for Modelling the Initiation Process of Low-Speed Pre-Ignition in Downsized SI-Engines

ausgeführt zum Zwecke der Erlangung des akademischen Grades eines
Doktors der technischen Wissenschaften unter der Leitung von

Assoc. Prof. Dr. Thomas Lauer

E315

Institut für Fahrzeugantriebe und Automobiltechnik

und (Zweitgutachter)

apl. Prof. Dr.-Ing. habil. Christian Schwarz

BMW Group, München

eingereicht an der Technischen Universität Wien

Fakultät für Maschinenwesen und Betriebswissenschaften

von

Dipl.-Ing. Michael Heiß

Matrikelnummer 0425598

Dorf 13, 3352 St. Peter/Au

Vorwort

Die vorliegende Arbeit entstand während meiner Tätigkeit als Projektassistent am Institut für Fahrzeugantriebe und Automobiltechnik der Technischen Universität Wien.

Dem Institutsvorstand Univ. Prof. Dr. Bernhard Geringer danke ich für die Möglichkeit, dass ich im Simulations-Team des Instituts an aktuellen Forschungsthemen im Motorenbau mitwirken durfte. Ein besonderer Dank gilt Assoc. Prof. Dr. Thomas Lauer für die wissenschaftliche Betreuung und seine fachliche Unterstützung bei der Erstellung dieser Arbeit.

Prof. Dr.-Ing. habil. Christian Schwarz von der BMW Group danke ich für sein reges Interesse an meiner Dissertation und die Bereitschaft die Funktion des Zweitprüfers zu übernehmen.

Meinem Projektkollegen Nikola Bobicic möchte ich für seinen besonderen Einsatz bei der Durchführung der experimentellen Untersuchungen am Motorprüfstand danken. Unserem Projektpartner aus der Industrie, Herrn Dipl.-Ing. Stefan Pritze von GM Powertrain, danke ich für die hervorragende Zusammenarbeit und die gewährte Freiheit bei der Methodenwahl.

Allen Institutskollegen, insbesondere Simon Fischer, Henrik Smith, Markus Zöchbauer, Friedrich Forsthuber und Werner Holly danke ich sehr herzlich für die tolle gemeinsame Zeit im Büro und die unzähligen fachlichen und freundschaftlichen Gespräche. Ich bin froh, jeden von ihnen kennengelernt zu haben und freue mich auf ein baldiges Wiedersehen.

Meinen Eltern danke ich für ihr Vertrauen, ihre Warmherzigkeit und dass sie mir trotz der räumlichen Distanz immer das Gefühl gegeben haben, fest verwurzelt zu sein. Meiner Schwester danke ich für die Herzlichkeit in ihrer Familie und dafür, stets willkommen zu sein.

Ein ganz besonderer Dank gilt meiner Frau Babsi, die mich durch alle Phasen meiner Arbeit begleitet hat und immer für mich da ist. Unsere aufregende gemeinsame Zeit in Wien, in der wir zueinander gefunden haben, wird für mich immer unvergesslich bleiben.

St. Peter/Au, Juni 2016

Michael Heiß

Abstract

For spark ignited engines, a low fuel consumption demands advanced operation strategies. A step towards future CO₂ emission limits are downsized gasoline engines with direct injection and high boost pressures. Experiences so far showed that at high loads and particularly at low engine speeds, spontaneous pre-ignitions randomly occur already before the regular spark timing. The resulting super-knocking combustion can lead to severe engine damage already after a single event. Previous activities on the pre-ignition phenomenon suggest that the presence of separated oil or oil-fuel droplets is the most probable explanation for the observed pre-ignition events.

This work comprises a systematic study of the entire process chain leading to droplet induced pre-ignition. High-speed images of pre-ignition events recorded with optical diagnostics are interpreted to describe the spatial characteristics of the autoignition processes and to derive an appropriate modelling approach. For that reason, engine process simulation, 3D-CFD simulation and reaction kinetic models are combined to account for the physical as well as the chemical processes leading to a premature ignition of the charge.

The detailed evaporation behaviour of fuel and oil in the hot cylinder charge is considered by introducing multi-component surrogate fluids for CFD. Due to the obvious importance of wall film regarding pre-ignition, a considerable effort is invested to gain a realistic representation of the fuel impingement process. Critical wall wetting leading to oil dilution is further analysed in view of a potential separation of oil-fuel droplets. The resulting dispersion of such droplets and their probability to survive until compression-end and to serve as an igniting spot is investigated. An approach is developed to capture the complex autoignition behaviour of oil with detailed chemical kinetics. A calibration with experimental single droplet studies is conducted to allow statements about the critical oil vapour fraction which is necessary for pre-ignition. Furthermore, a statistical approach is employed to evaluate the impact of the droplet separation timing on the probability for high oil evaporation rates.

It was found that the drop temperatures adjusting towards TDC are largely independent on the moment of droplet entrainment. In fact, the drop size and the gas temperatures during compression are the determining factors for the droplet thermal state at a potential pre-ignition timing. The resulting local oil fractions originating from the evaporating droplet were further evaluated. It was shown that critical conditions for a premature ignition are most likely met by droplets lying within a defined diameter range. Earliest pre-ignition, however, could exclusively be stated for drop sizes lying close to a specific critical diameter. This explains why early events are generally observed extremely rare at the test bench and a significantly higher pre-ignition probability is stated towards TDC.

The presented method and the validated numerical models allow a detailed investigation of each sub-process leading to pre-ignition. In addition, it can be adopted as a development procedure to study the pre-ignition tendency of future SI engines already in the early concept phase.

Kurzfassung

Um die scharfen CO₂ Grenzwerte mit modernen Ottomotoren einhalten zu können, haben sich Downsizing-Konzepte mit Direkteinspritzung und Turboaufladung als wirkungsvoll erwiesen. Speziell bei niedriger Drehzahl und hoher Last können jedoch frühzeitige Selbstzündungen deutlich vor dem regulären Zündzeitpunkt auftreten. Die daraus resultierende stark klopfende Verbrennung kann bereits innerhalb kürzester Zeit zum Motorschaden führen. Vorangegangene Studien zum Thema Vorentflammung weisen darauf hin, dass abgelöste Schmierstoff- bzw. Kraftstofftropfen als wahrscheinlichste Ursache in Frage kommen.

Die vorliegende Arbeit beschreibt einen systematischen Ansatz zur Untersuchung der gesamten Vorentflammungs-Prozesskette, die durch Tropfen ausgelöst wird. Mittels optischer Messtechnik aufgenommene Vorentflammungsvorgänge dienen als Grundlage zur Ableitung eines geeigneten Modellierungsansatzes. Um sowohl die physikalischen, als auch die chemischen Vorgänge, die zur vorzeitigen Zündung führen, berücksichtigen zu können, werden Motorprozessrechnungen, 3D-CFD Simulationen und Reaktionskinetikmodelle kombiniert eingesetzt.

Um das detaillierte Verdampfungsverhalten von Kraftstoff und Öl in der heißen Zylinderladung abzubilden, werden Mehrkomponenten-Kraftstoffmodelle eingeführt. Eine kritische Wandbenetzung, die zu einer Verdünnung des Schmierfilms am Zylinderrohr führt, wird in Hinblick auf eine potentielle Ablösung von Tropfen untersucht. Die räumliche Verteilung abgelöster Tropfen wird ausgewertet um die Wahrscheinlichkeit zu ermitteln, mit der sie als Zündquelle dienen können. Um die komplexen und weitgehend unbekannten Reaktionen bei der Selbstzündung von Öl abbilden zu können, wird ein Ansatz auf Basis detaillierter Reaktionskinetik vorgestellt. Ein Abgleich mit RCM-Einzeltropfenexperimenten ermöglicht dabei die Bestimmung vorentflammungskritischer Ölkonzentrationen. Mit einem statistischen Ansatz wird zudem der Einfluss des Tropfen-Ablösezeitpunkts auf die resultierenden Ölkonzentrationen bewertet.

Mit Hilfe der eingesetzten Simulationsmethode kann verdeutlicht werden, dass die Tropfentemperatur, die sich während der Kompression einstellt, weitgehend unabhängig vom Ablösezeitpunkt ist. Die Tropfengröße und die Ladungstemperatur zeigen sich hingegen als bestimmende Größen für die Verdampfungsneigung des Tropfens. Es wird festgestellt, dass kritische Ölkonzentrationen für eine vorzeitige Selbstzündung nur von Tropfen erreicht werden, die innerhalb eines bestimmten Durchmesserbereichs liegen. Früheste Vorentflammungen können hingegen ausschließlich durch Tropfen verursacht werden, die sehr nahe an einem kritischen Durchmesser liegen. Dadurch konnte erklärt werden, warum frühe Vorentflammungen generell selten auftreten und die Wahrscheinlichkeit für spätere Zeitpunkte deutlich höher liegt.

Der dargestellte Modellierungsansatz erlaubt eine detaillierte Untersuchung der einzelnen Teilprozesse in zur Entstehung von Vorentflammungen führen. Im Motorentwicklungsprozess kann er dazu verwendet werden, um die Vorentflammungsneigung neuer Ottomotoren bereits in der Konzeptphase bewerten zu können.

Contents

1. Introduction: Fuel Economy Potentials of Downsizing	1
2. State of Knowledge and Research	6
2.1. Types of Irregular Combustion in SI-Engines	6
2.2. Pre-Ignition Mechanisms.....	9
2.2.1. Hypothesis of Droplet Induced Autoignition	10
2.2.2. Hypothesis of Hot Solid Particle Induced Ignition.....	14
2.3. Overview about the current Knowledge on Pre-Ignition.....	17
2.4. Pre-Ignition Modelling Strategies.....	18
3. Objective of the Investigation	20
4. Autoignition Fundamentals	21
4.1. Oxidative Characteristics of Hydrocarbons	21
4.1.1. Low Temperature Chemistry	24
4.1.2. Intermediate Temperature Chemistry.....	27
4.1.3. High Temperature Chemistry	29
4.2. Single Droplet Ignition	31
4.3. Requirement for Thermal Ignition	33
4.4. Initial Flame Kernel and Flame Propagation.....	34
4.5. Detonation and Intensity of Super-Knock.....	37
5. Experimental Evaluation of Pre-Ignition Characteristics	39
5.1. Description of the Test Bench Setup.....	39
5.2. Pre-Ignition Statistics and Analysis of Cyclic Variations.....	40
5.3. Observations with a High-Speed Endoscopic Access	43

6. Determination of Charge Inhomogeneities with CFD	46
6.1. Description of the CFD Model	46
6.2. Fuel Injection and Spray Validation	47
6.3. Implementation of a Multi-Component Fuel.....	49
6.4. Validation of the Liquid Film Formation.....	51
6.5. Impact of Fuel Evaporation on Temperature Inhomogeneities	59
7. Analyses on the Reactive Impact of Fuel on Pre-Ignition	63
7.1. Implementation of a Gasoline Surrogate in a Stochastic Reactor Model.....	63
7.2. Determination of the Autoignition Limit via Knock Cycles.....	64
7.3. Validation of the Surrogate Fuel's Autoignition Sensitivity.....	67
7.4. Modelling of Remaining Fuel Droplets.....	70
8. Analyses on Oil Droplet Induced Pre-Ignition	74
8.1. Pre-Ignition Process Chain.....	74
8.2. Evaluation of Fuel Deposition and Oil Dilution.....	75
8.3. Modelling of Detached Oil-Fuel Droplets.....	77
8.4. Validation of the Single Droplet Evaporation	81
8.5. Determination of the Oil Reactivity.....	89
8.6. Modelling of the Oil Droplet induced Pre-Ignition Process.....	94
8.6.1. Critical Oil Vapour Fraction for Pre-Ignition.....	94
8.6.2. Critical Droplet Evaporation Behaviour	97
8.7. Discussion of the Oil Droplet Hypothesis.....	103
8.7.1. Hot Solid Particles	103
8.7.2. Supercritical Effects	104
9. Conclusion	106
10. Bibliography	109

Nomenclature

Symbols

A	Pre-exponential Arrhenius factor	—
A	Surface area	m^2
a	Speed of sound	m/s
AFR	Air to fuel ratio	—
A_T	Turbulent flame surface	m^2
B	Spalding transfer number	—
B	Empirical regime limit factor for Bai model	—
c_p	Specific heat capacity	$\text{J}/(\text{kg} \cdot \text{K})$
D	Droplet diameter	m
\mathfrak{D}	Molecular diffusivity	m^2/s
E_a	Activation energy	J/mol
f	Frequency	$1/\text{s}$
h	Heat transfer coefficient	$\text{W}/(\text{m}^2 \cdot \text{K})$
h_R	Enthalpy of reaction per unit volume	J/m^3
h_{vap}	Specific heat of vaporisation	J/kg
I	Livengood-Wu-integral	—
i	Number of revolutions per stroke	—
k	Rate constant	—
k	Turbulent kinetic energy	m^2/s^2
LHV	Lower heating value	J/kg
L_{st}	Stoichiometric air mass	kg
Le	Lewis number	—
M	Molecular weight	kg/mol
n	Engine speed	$1/\text{s}$
Nu	Nusselt number	—
n	Order of reaction	—
p	Pressure	N/m^2
P_e	Effective power	W
p_{me}	Brake Mean effective pressure	N/m^2
p_{mi}	Indicated Mean effective pressure	N/m^2
q	Exponent for Rosin-Rammler distribution	—
R	Universal gas constant	$\text{J}/(\text{mol} \cdot \text{K})$
r	Radius	m
r_c	Critical radius for autoignition	m
Re	Reynolds number	—
r_f	Critical radius for flame propagation	m
Sc	Schmidt number	—

Sh	Sherwood number	—
s_L	Laminar flame speed	m/s
s_T	Turbulent flame speed	m/s
T	Torque	Nm
T	Temperature	K
t	Time	s
T_L	Leidenfrost Temperature	K
T_{sat}	Saturation temperature	K
u	Velocity	m/s
u_a	Velocity of the autoignition reaction front	m/s
V_H	Engine displacement	m ³
w	Mass fraction	kg/kg
We	Weber number	—
\tilde{x}	Mole fraction	mol/mol
X	Factor for Rosin-Rammler distribution	m
x, y, z	Coordinates	m
Ze	Zeldovich number	—

Greek Symbols

α	Thermal diffusivity	m ² /s
β_v	Evaporation coefficient	m ² /s
δ_c	Critical Frank-Kamenetskii parameter	—
δ_l	Laminar flame thickness	m
ε	Reactivity coefficient for detonation	—
ε	Turbulent dissipation	m ² /s ³
η_i	Indicated fuel conversion efficiency	—
η_m	Mechanical efficiency	—
ρ	Density	kg/m ³
λ	Lambda	—
λ	Thermal conductivity	W/(m · K)
λ_l	Volumetric efficiency	—
ν	Kinematic viscosity	m ² /s
ξ	Resonance parameter for detonation	—
ψ	Rosin-Rammler probability density function	1/m
σ	Surface tension	kg/s ²
τ	Ignition delay time	s
τ_1	First induction time	s
τ_2	Second induction time	s

Abbreviations

<i>BDC</i>	Bottom dead centre
<i>CFD</i>	Computational fluid dynamics
<i>DDM</i>	Discrete droplet model
<i>DI</i>	Direct injection
<i>DOE</i>	Design of experiment
<i>EGR</i>	Exhaust gas recirculation
<i>FE</i>	Finite Element Method
<i>FID</i>	Flame Ionisation Detector
<i>FSN</i>	Filter smoke number
<i>HC</i>	Hydrocarbons
<i>HCCI</i>	Homogeneous charge compression ignition
<i>IVC</i>	Intake valve closing
<i>LES</i>	Large eddy simulation
<i>LSPI</i>	Low speed pre-ignition
<i>MFB</i>	Mass fraction burned
<i>MON</i>	Motor octane number
NEDC	New European Driving Cycle
NO_x	Nitrogen oxides
<i>NTC</i>	Negative temperature coefficient
<i>PCEO</i>	Passenger car engine oil
<i>PDA</i>	Phase Doppler anemometry
<i>PFI</i>	Port fuel injection
<i>PI</i>	Pre-Ignition
<i>PM</i>	Particulate matter
<i>PN</i>	Particulate number
<i>PRF</i>	Primary reference fuel
<i>RANS</i>	Reynolds-average Navier-Stokes
<i>RCM</i>	Rapid compression machine
<i>RDE</i>	Real driving emissions
<i>RON</i>	Research octane number
<i>SI</i>	Spark ignition
<i>SMD</i>	Sauter mean diameter
<i>SOI</i>	Crank angle position at start of injection
<i>SRM</i>	Stochastic reactor model
<i>TDC</i>	Top dead centre
<i>TPA</i>	Three pressure analysis
<i>TRF</i>	Toluene reference fuel
<i>WLTP</i>	Worldwide harmonized Light vehicles Test Procedure
$^{\circ}CA_{aTDC}$	Degree-crank-angle after top dead centre firing

1. Introduction: Fuel Economy Potentials of Downsizing

A central element of modern vehicle development is the reduction of tailpipe emissions. Toxic components like carbon monoxide (CO), nitrogen oxides (NO_x), hydrocarbons (HC) and particulate matter (PM) have been successfully reduced within EU regulations during the last decades. Beginning in September 2015 the Euro 6 emission standard became mandatory for all new vehicles in the EU. Euro 6 sets emission limits for gasoline vehicles that are up to 68% lower (CO) than those established under Euro 1 in 1992. Additionally, a key challenge is certainly the newly specified particulate number limit (PN) for direct injected gasoline engines. Generally, harmful exhaust gas components of modern engines increasingly approach levels that lie within the range of measuring accuracy what represents a challenge for new measuring devices.

Beside other emissions, the greenhouse gas CO₂ is non-toxic but an important factor influencing the often cited climate change. This fact has caused a growing debate in social and political life about energy consumption and particularly with regard to personal and commercial traffic. In 2010, the global road transport sector was responsible for almost 17 % of all anthropogenic CO₂ emissions, as depicted in [Figure 1.1](#). Light duty vehicles, passenger cars and two-wheelers running on fossil fuels are the major contributors in this field.

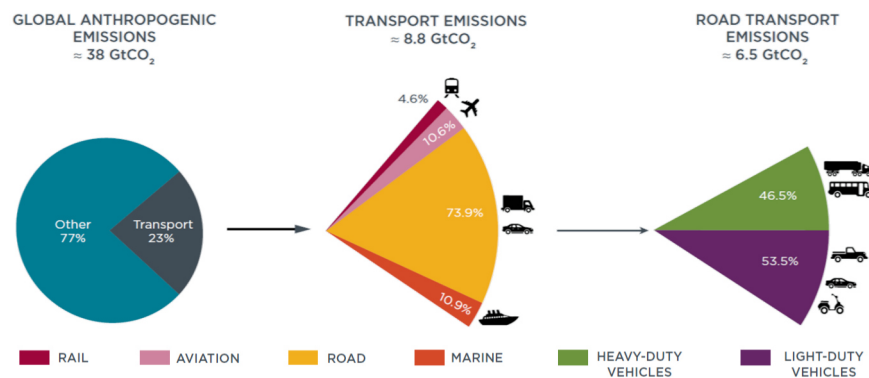


Figure 1.1: Global transport sector lifecycle CO₂ emissions in 2010 [1]

As can be seen in [Figure 1.2](#), most of the world's markets have adopted regulations requiring automotive manufacturers to improve their vehicle fleet's fuel consumption which is directly linked to CO₂ emissions. The European Commission adopted an emission target for 2020, which provides a limit value of only 95 g CO₂ per kilometre driven. Translated into fuel consumption this equates to 4.1 litres of gasoline per 100 km, what represents an enormous challenge to automotive engineers. Failure to comply with the CO₂ target results in expensive penalties for car manufacturers. Therefore, the automobile industry has made significant improvements in the development of fuel-efficient vehicles.

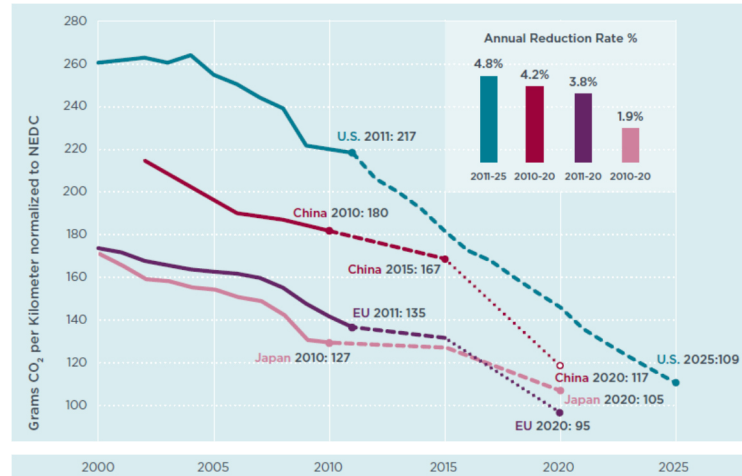


Figure 1.2: Global comparison of passenger car CO₂ emission standards [2]

While transportation volume has continued to rise, carbon emissions trend downwards since many years. Besides enhancing vehicle design and driving resistance, strongly promoted technologies like hybrid-electric or battery-electric powertrains may help improving the CO₂ balance. These concepts, however, can only be advantageous if the electric energy is provided from sustainable sources and the ‘well to wheel’ process chain is considered entirely. However, the vast majority of the world transport market will still be dominated by spark-ignited (SI) engines the next decades. Therefore, effective measures have to be developed to further improve the efficiency of internal combustion engines.

Downsizing is an example of such an improvement strategy that has been successfully implemented the last years. At low loads, a significant part of the indicated work is spent to overcome friction and pumping losses due to throttling in SI engines. The idea of downsizing is to shift the main operating range to higher mean pressures via reducing engine displacement. In order to maintain the dynamic driveability, air boosting is necessary to increase the charge mass and hence the brake mean effective pressure p_{me} and torque T . [Figure 1.3](#) clearly illustrates the effect of downsizing over the last years. A decreasing trend can be noticed for the average passenger car engine displacement and especially CO₂ emissions whereas engine power increased distinctly.

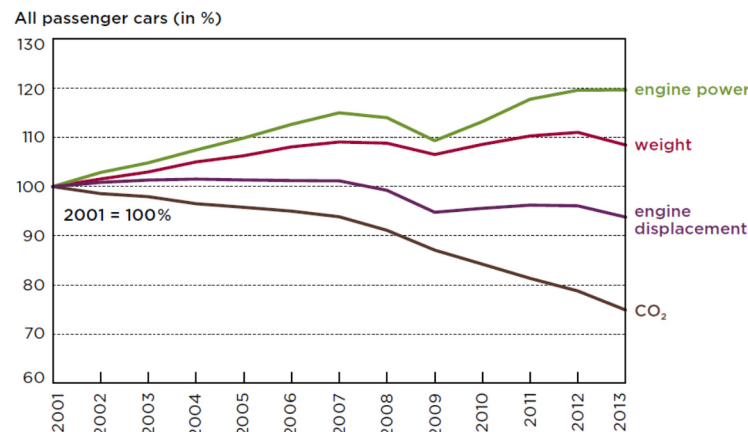


Figure 1.3: Development of passenger car CO₂ emissions and technical parameters [3]

Usually, engines are denoted as downsizing concepts when they exhibit a reduced displacement V_d while the resulting loss in power and torque is compensated by a higher power density P_e/V_d . This can be accomplished either by increasing the engine speed n or the engine's specific torque T/V_d , via the equation:

$$\frac{P_e}{V_d} = \frac{n \cdot p_{me}}{i} = 2\pi \cdot n \cdot \frac{T}{V_d} \quad (1.1)$$

Thereby, i is the number of crankshaft rotations per working cycle, P_e the effective power and T the brake torque. At constant load, the engine efficiency decreases for higher speeds due to a disproportionate increase of mechanical losses. Therefore, a significant reduction of fuel consumption can only be achieved through high-load concepts with high mean effective pressures p_{me} that can be derived from the equation:

$$p_{me} = \rho_L \cdot \frac{LHV}{L_{st}} \cdot \frac{1}{\lambda} \cdot \eta_i \cdot \eta_m \cdot \lambda_a \quad (1.2)$$

Engines with high-load concepts usually employ a charging system with charge air cooling to effectively increase both the volumetric efficiency λ_a and the charge density ρ_a . This effect can ideally be enhanced by combining with gasoline direct injection leading to lower charge temperatures due to the evaporative cooling effect of the fuel. This, in addition, allows an increase of the geometric compression ratio and the boost level what results in higher indicated fuel conversion efficiency η_i over the entire speed range. A reduction of friction losses further supports downsizing measures via increasing the mechanical efficiency η_m . A low relative air-fuel ratio λ would be favourable but has to be kept close to stoichiometry because of the three-way catalyst exhaust aftertreatment. Fuel parameters, as the lower heating value LHV and the stoichiometric air mass L_{st} cannot be varied arbitrarily and can therefore be seen as constant boundaries.

To give an impression about the efficiency potential of such downsizing measures, several engine concepts are compared by means of the New European Driving Cycle (NEDC) in [Figure 1.4](#).

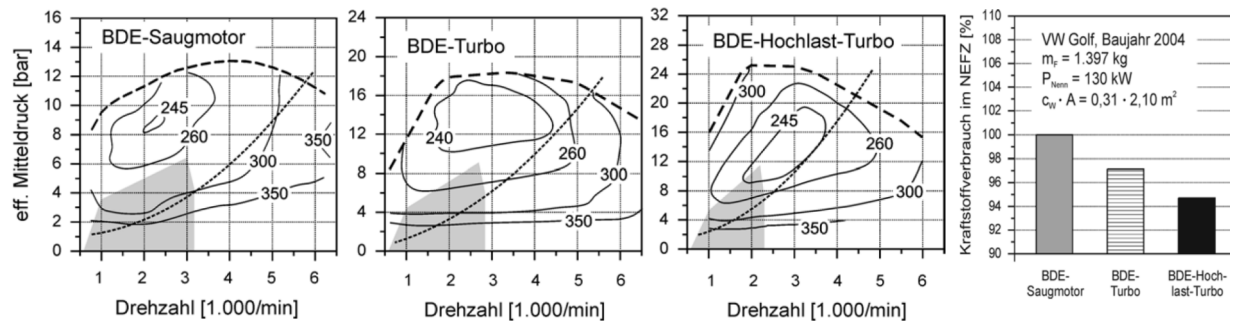


Figure 1.4: Operating maps including contour lines of specific fuel consumption of different engine concepts and their respective fuel consumption in the NEDC (right); the typical operating range within the NEDC is displayed on a gray background; the driving resistance in the fifth gear is depicted as a dotted line [4]

From the operating maps it becomes clear that only an appropriate charging system allows specific fuel consumptions below 245 g/kWh within the operating range of the NEDC (grey areas). Additionally, high-performance turbocharging with high boost pressures enables a longer residence time within favourable conditions of highest fuel efficiency. This effect can be enhanced with the concept of downspeeding. With higher feasible transmission ratios, the required operating area can be shifted to higher loads at lower speeds. This is shown exemplarily by dotted lines in Figure 1.4, representing the respective driving resistance in the fifth gear.

Especially for high downsizing levels with high boost pressures, the thermal and mechanical loading rises excessively, especially under full load. Under certain conditions of temperature, pressure, mixture composition and speed, the risk of irregular autoignition phenomena, like knocking and pre-ignition rises sharply. A common method for lowering the reactivity of autoignition processes is to decrease the charge temperature via operation at under-stoichiometric fuel-rich conditions. The additional heat of vaporisation helps to cool down the mixture and also protects engine components like the exhaust valves, the turbocharger or the three-way catalyst from thermal overstress. Furthermore, knock control is implemented to automatically retard spark timing to avoid autoignition critical operation at the cost of combustion efficiency. Although these measures are effective, they are counterproductive to the downsizing concept and considerably impair fuel efficiency close to full load, as can be seen by the specific fuel consumption approaching values beyond 300 g/kWh for the high-performance concept in Figure 1.4.

High load operating points are not included in the NEDC, which is why highly downsized engines can reach exceptionally low fuel consumption rates. As was shown in [5], the real fuel consumption of typical passenger car engines is about 10 – 20 % higher compared to the normalised NEDC values. Thus, downsizing is further increasing the deviation, what is difficult to communicate to the customer. Therefore, it is proposed that from September 2017 onwards, the more dynamic Worldwide harmonized Light vehicles Test Procedure (WLTP) will be the main cycle for type approval. In addition, it is intended that vehicles must comply with emission limits under real driving test conditions (RDE). The left diagram in Figure 1.5 reveals that more dynamic test cycles lead to an extended operating range towards full load, especially at low engine speeds.

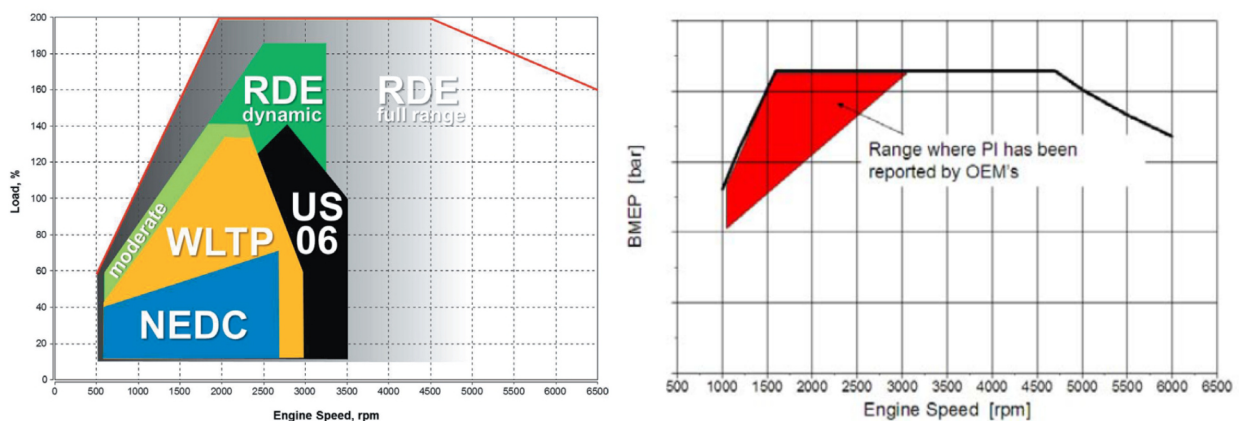


Figure 1.5: Operating ranges of different test cycles for type approval (left) [6]; Critical range for the occurrence of pre-ignition (right) [7]

Therefore, stoichiometric operation is highly necessary but emphasises the occurrence of pre-ignition, which is an autoignition phenomenon that is linked to the full load speed range between 1000–2500 rpm, see right diagram in Figure 1.5.

In contrast to knocking or surface ignition, pre-ignition is a relatively recent phenomenon that has emerged from elevated compression ratios and high boost levels of downsizing concepts. It is characterised by a spontaneous autoignition of the charge before the regular spark timing. Due to its stochastic nature it can be neither predicted by pressure indication nor influenced by knock control. The premature ignition of the mixture results in maximum cylinder pressures beyond 200 bar. The resulting mechanical overstress can lead to severe damages of engine components already after one pre-ignition event, see [Figure 1.6](#).

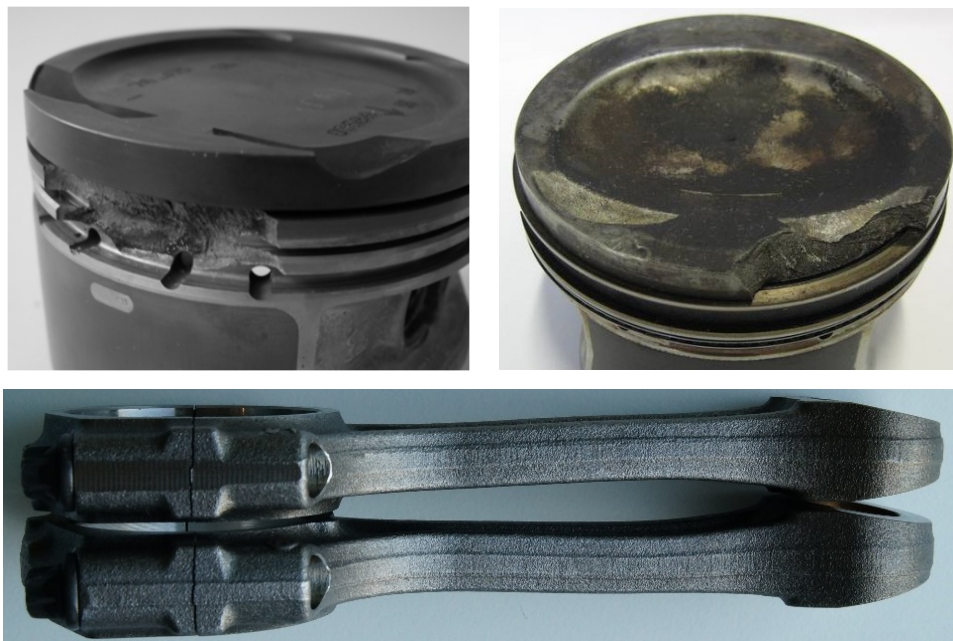


Figure 1.6: Damages of different engine components due to the thermal and mechanical overload caused by pre-ignition: broken piston lands close to oil drain holes [8] (upper left), broken piston top land close to a valve pocket (upper right), deformed connecting rods (bottom)

An effective control of the combustion process is crucial for engines with high power density, especially under full load. Although moderate downsizing, what might be called “rightsizing” is widely applied, uncontrollable irregular combustion phenomena will be a main focus to ensure reliability. Therefore, the mechanisms leading to pre-ignition are of major interest to find appropriate countermeasures to fully exploit the potentials of downsizing.

2. State of Knowledge and Research

2.1. Types of Irregular Combustion in SI-Engines

Knock

Since the invention of the spark ignition engine, irregular combustion phenomena have always been a special focus for researchers and engine manufacturers. The striving towards higher engine power density and efficiency has led to the occurrence of combustion irregularities already at the end of the 19th century. In 1882 Clerk [9] documented for the first time that a characteristic metallic pinging sound transmitted through the engine structure indicated abnormal combustion and so he called the phenomenon “knock”. This occurs especially under extreme full load conditions when unburned gas ahead of a regular spark-triggered flame front spontaneously burns under rapid heat release with very high local pressures. The resulting pressure waves are reflected on the combustion chamber walls and excite its eigenmodes which usually lie between 5 to 10 kHz. The resulting high-pressure oscillations which become evident in [Figure 2.1](#) cause high mechanical and thermal loading that can lead to erosion or melting of the chamber walls and valves, sticking or breakage of piston rings and other severe damages.

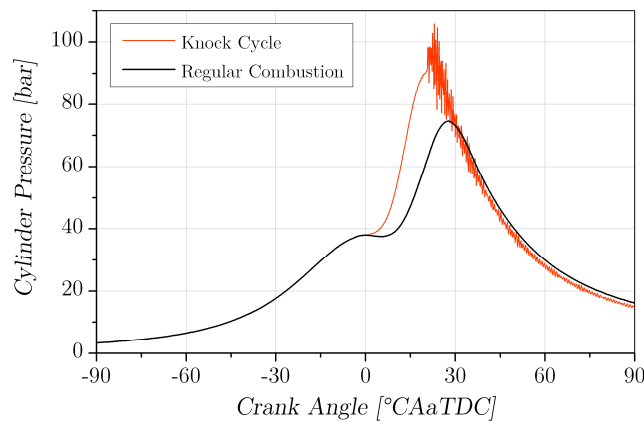


Figure 2.1: Typical cylinder pressure trace of a heavy knocking cycle [10]

In several publications around 1920 [11,12] Ricardo was the first who described the “autoignition theory”. He assumed that knocking was triggered by a spontaneous and nearly simultaneous autoignition of the unburned zone caused by its compression due to the regular propagating flame. Around that time also contrary explanations emerged that described knocking to be caused by an acceleration of the regular flame front until detonation without any end gas autoignition. Therefore this was called the “detonation theory”.

One of the first high speed images of knocking combustion recorded at 5,000 Hz carried out by Withrow and Rassweiler [13] in 1936 revealed that spontaneous ignition can originate in local regions within the end-gas what confirmed the “autoignition theory” of Ricardo [11,12]. With an improved optical measurement system Miller [14] employed the Schlieren photography in the 1940s for

combustion analysis at frame rates up to 200,000. With his experiments Miller described a combined “autoignition-detonation theory”, which implied that one or more exothermic centres in the end-gas might develop to a knocking reaction front of detonative character propagating with speeds up to 2,000 m/s. At this time it was widely accepted that pre-reactions in the end-gas decide about the occurrence of knock.

During the early 1980s piezoelectric knock sensors were introduced detecting the structure-borne sound of knock events. If knock amplitudes exceed a certain threshold, spark timing is retarded for the next cycles. In this way knocking gets controllable at the cost of thermal efficiency. Thus the knock propensity of an engine constrains engine efficiency, since it prevents operation with optimum combustion phasing and also limits the maximum possible compression ratio. Designing a knock proof combustion process is therefore crucial, which is why it is still subject of extensive research work.

Surface Ignition

An even higher damaging potential than that of knocking arises if autoignition occurs already before spark timing, triggered by hot surfaces and is referred to as “surface ignition”. According to Ricardo [15], one of the first premature ignition phenomena were already recorded in 1904 by Prof. Hopkinson from Cambridge University, who also suspected different mechanisms between knocking and surface ignition. In 1925 Sparrow [16] was the first to state that surface ignition is a consequence of knocking combustion what agrees well with present-day knowledge: The pressure wave resulting from knocking combustion interacts with the thermal boundary layer what increases the heat transfer to the wall, as shown with wall temperature measurements by Grandin and Denbratt [17]. In this way certain critical wall regions with insufficient cooling can heat up significantly, causing earlier autoignition in the subsequent cycle with even stronger knock, as illustrated in [Figure 2.2](#). As this effect can act self-amplifying with continuously advancing autoignition timing, surface ignition is potentially the most damaging type of irregular combustion. However, with an appropriate choice of the spark plug heat range to prevent overheating and adapted engine design features like radiused metal edges or removal of exposed components, surface ignition can be avoided effectively.

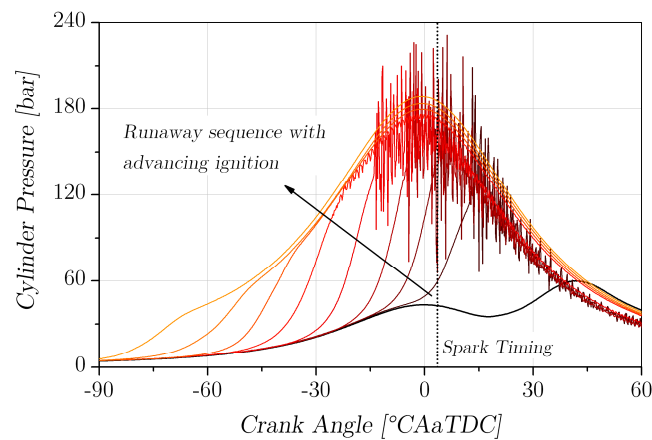


Figure 2.2: Cylinder pressure traces for a self-amplifying surface ignition [10]

Pre-Ignition

As was pointed out by Kapus et al. [18], a new autoignition phenomenon arose around 2005 when downsizing concepts were introduced to improve the global engine efficiency. High compression ratios and high boost levels promote the sporadic occurrence of autoignition before spark timing, especially at speeds around 1500–2500 rpm and $p_{me} > 20$ bar. Hence it is referred to as “low-speed pre-ignition” (LSPI) or as “stochastic, sudden, random or spontaneous pre-ignition” to characterize its inherently different behaviour to other premature ignition phenomena. In contrast to surface ignition, this kind of irregular combustion is generally induced locally in the gas phase resulting from inhomogeneities being present in the charge, as was shown in early optical investigations on this topic by Kapus et al. [18] and Han et al. [19]. The authors concluded that these may result from the presence of detached deposits, liquid droplets or inhomogeneities of temperature and fuel vapour.

Vangraefschèpe and Zaccardi [20] noted that the initial flame propagation is relatively slow and of deflagrative nature like a regular combustion. As can be seen in the left diagram of Figure 2.3, a premature ignition leads over to a sudden heat release of detonative character with violent pressure amplitudes and peak values greater than 200 bar. For that reason, this phenomenon is also termed as “super-knock” that sometimes can cause substantial engine breakdown already after a single event.

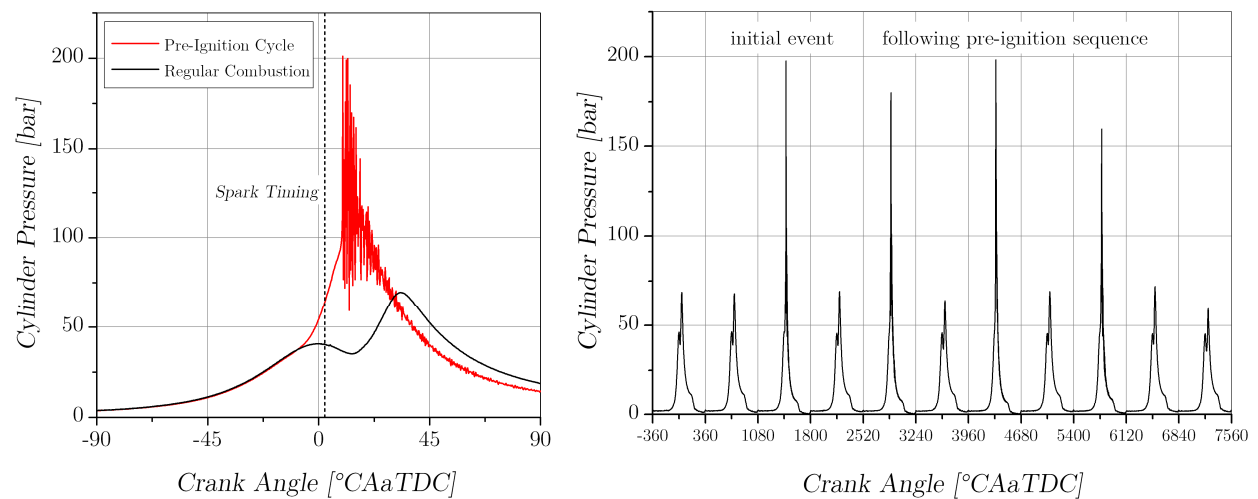


Figure 2.3: Pressure trace of a typical pre-ignition event resulting in super-knock (left) and an alternating pre-ignition sequence with several follow-up events (right) [10]

Generally, pre-ignitions are not self-amplifying like surface ignitions but frequently occur in clusters of usually 1–5 events (also up to 20 are reported) in an intermittent pattern, where a regular combustion follows after a pre-ignition cycle before a follow-up pre-ignition event sets in again. The right diagram of Figure 2.3 shows the cylinder pressure of a pre-ignition sequence of four events alternating with regular cycles. Generally, a single pre-ignition or a pre-ignition sequence is very rare and occurs only once every 10,000 to 30,000 cycles while operation under critical full load conditions. Due to its stochastic nature, pre-ignition cannot be predicted by pressure indication or knock sensors before an event and thus it is a strong limitation for higher boost levels and further efficiency improvements. Consequently, there is a main focus on pre-ignition what led to numerous

theoretical and experimental studies. The following chapter gives an overview of the current state of research and knowledge about the mechanisms leading to pre-ignition.

2.2. Pre-Ignition Mechanisms

Many experimental investigations were carried out in order to determine the statistical influence of different operating conditions or engine parameters on the pre-ignition rate. Optical accesses and high speed imaging have proved as suitable to localise possible trigger mechanisms and to gain knowledge about fundamental processes which led to several conclusions and theoretical approaches attempting to describe pre-ignition.

First major findings about pre-ignition were carried out with optical diagnostics and concerned the localisation of the early irregular flame kernel: Investigations of Zahdeh et al. [21] with a fibre optical spark plug and lateral injection shows a general tendency of pre-ignitions to occur randomly distributed in the combustion chamber. However, a focus of pre-ignition spots is found close to the spark plug and the exhaust valve faces when the coolant temperature is lowered or spark timing is retarded. A similar behaviour is reported by Kieberger [22] who replaces the conventional ignition system with a laser spark plug without any exposed electrodes. He detects that the pre-ignition spots are moving from the spark plug area to the overall charge but still with a slight focus at the exhaust valve faces. Hülser et al. [23] confirm the same behaviour when using a fuel with higher latent heat, like ethanol, instead of gasoline. Günther et al. [24] compare pre-ignition rates of a DI engine and a port fuel injected (PFI) engine. In contrast to PFI, DI is known for the increased charge cooling effect due to fuel evaporation directly inside the cylinder. This leads to pre-ignition spots that are localised more likely in vicinity of the spark plug electrodes whereas with PFI they are distributed all over the combustion chamber. These independent findings suggest that all measures that lead to a cooler charge, make the hottest components to the major source of pre-ignition. Although, heated areas seem to promote autoignition, surface ignition is rather unlikely: Günther et al. [24] carry out fundamental experiments on a single cylinder research engine with a glow plug that serves as an artificial hot spot. It is shown that a minimum plug temperature of about 820 °C is necessary to effectively trigger surface ignition for RON95 at a speed of 1500 rpm and 16 bar p_{mi} . Kieberger [22] applies a thermocouple at the end face of a spark plug that obviously triggers pre-ignition. In a full engine at comparable operating conditions but even somewhat higher p_{mi} of about 22 bar a rather low temperature of about 370 °C is measured at the base of the ground electrode. Assuming that the temperature at the tip of the ground electrode is certainly higher, it is still very unlikely that it reaches the critical temperature for surface ignition. This is supported by the fact that Kieberger [22] finds no improvement in pre-ignition tendency when he uses a colder heat range spark plug. Finally, Dahnz et al. [25] and Palaveev et al. [26] detect solely pre-ignition spots that are spread over a wide range without significant accumulations at hot surfaces, but with the majority located less than 5 mm above the piston crown, see [Figure 2.4](#). As a consequence, the authors categorically exclude hardware hot-spots as root cause for pre-ignition.

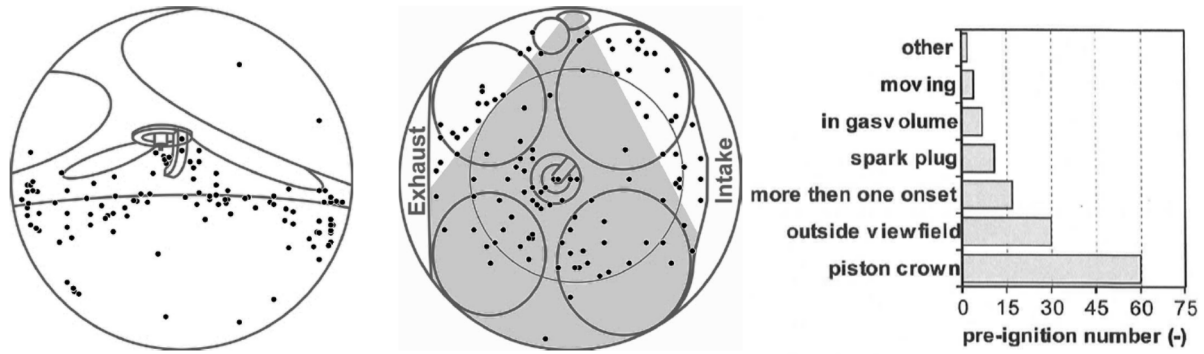


Figure 2.4: Spatial distribution of pre-ignition kernels (marked as dots), from Palaveev et al. [26]

2.2.1. Hypothesis of Droplet Induced Autoignition

The comprehensive studies of Dahnz et al. [25], Zahdeh et al. [21] and Birkigt [27] indicate the presence of oil or oil-fuel droplets as the most probable explanation for the observed pre-ignitions: It is assumed that impingement of the injected spray on the cylinder liner results in an oil-fuel wall film that collects in the piston crevice volume of the top land during the compression stroke. Obviously, portions of the oil-fuel mixture are released from the top land due to inertia forces acting on the liquid during the deceleration phase before the piston reaches top dead centre (TDC), see [Figure 2.5](#).

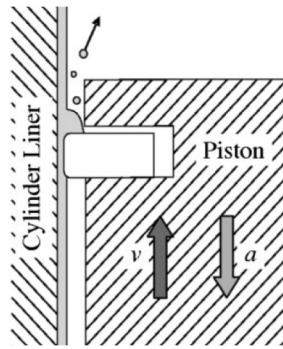


Figure 2.5: Hypothesis of droplet release from the piston top land, from Dahnz et al. [25]

This effect is facilitated as the surface tension and viscosity of the liner oil is lowered by the absorption of impinging fuel. Oil mixing with the fuel is suspected to lower the autoignition temperature of the detached droplets and hence would cause premature ignition.

Zahdeh et al. [21] employ a 3D piston ring dynamics model considering fluid cavities to analyse the compression ring behaviour with the finite element method. It is found that the axial ring acceleration can be more than one order of magnitude higher relative to the piston, what is explained by the ring bouncing in the ring groove. A similar model of Hadler et al [28] predicts that reverse blow-by exists during intake and the beginning of the compression stroke. Hence gas is pushed into the combustion chamber over the crevice for a significant amount of time.

Amann et al. [29] observe a large increase of exhaust richness and a spike in HC emissions directly after a PI event. With a suddenly advancing spark timing to provoke hard engine knock very similar to LSPI, no significant increase in richness or HC emissions is detected. Hence the authors believe that HC based compounds, especially from the lubricant, are accumulating in the piston top land crevice and are consumed during LSPI events.

Furthermore, the impact of the crevice on pre-ignition is demonstrated in a further experimental study by Amann et al. [30]. With a chamfered piston crown, a remarkable reduction of PI events up to 90 % was achieved, keeping in mind a marginally reduced compression ratio of 0.25 due to the removed volume. It is believed that an increased top land crevice allows deeper flame propagation into the crevice without quenching and thus burning the majority of accumulated hydrocarbons.

The previous findings imply that fuel transported to the liner and mixing with lube oil seems to be decisive for pre-ignition. Hence, studies about the impact of both liquids are discussed separately in the following:

Fuel Impact

Since pre-ignition is an autoignition phenomenon it seems obvious to test fuels with different octane ratings. Zahdeh et al. [21] observe that a high research octane number (RON) is beneficial for reducing PI. However, the authors note that this effect was mainly due to the lower necessary boost pressure and charge density for fuels with higher knock resistance to maintain constant p_{me} . For several fuels, a significantly lower PI characteristic is found than would have been expected according to their octane rating. A plausible reason is attributed to the high volatility of these fuels in the temperature range between 130 and 150 °C representing typical surface temperatures at the top of the cylinder liner. It is concluded that, the higher the fraction of fuel being in liquid state at that temperatures, the higher the resulting oil dilution due to a deeper spray penetration and more intensified wall wetting. Without giving details about the operating strategy, this is confirmed by Dahnz et al. [25] who find a correlation between the boiling behaviour of different fuels and the resulting PI rate, independently of their octane rating. The proposed mechanism is also in accordance with the observation that PI frequencies are reduced with higher coolant temperatures and deactivated piston cooling because of a more enhanced evaporation of the liquid fuel.

Strong uncertainty exists about the effects of the fuel's chemical composition. This becomes evident in experiments carried out by Amann et al. [29] who compare fuels with similar RON and motor octane number (MON) but fundamentally different chemical compositions. Fuels with high aromatic content obviously haven't changed PI frequency significantly, although aromatics such as toluene are known for their inhibiting effect on autoignition, as described by Dec and Sjöberg [31]. Moreover, no LSPI events are encountered for low-aromatics fuel blends, although they exhibit an increased tendency for low-temperature heat release and knock due to the higher amount of paraffins. During testing, the physical properties like surface tension, latent heat or boiling behaviour may superimpose with the fuel's autoignition characteristic. So far, no study is known that is able to single out specific fuel components to be decisive for preventing LSPI from only a chemical point of view.

Oil Impact

The base stock of typical engine oils generally consists of long-chain paraffinic hydrocarbons. Higher alkanes $> C_{16}H_{34}$ are the most essential components of modern high-quality base oils which are characterised by a relatively low autoignition resistance. The reactive behaviour of lubricating oil is demonstrated by Palaveev et al. [32] in a rapid compression machine (RCM). As can be seen from Figure 2.6 (left), the ignition delay time is about one order of magnitude shorter when typical engine oil is introduced as wall film compared to neat iso-octane.

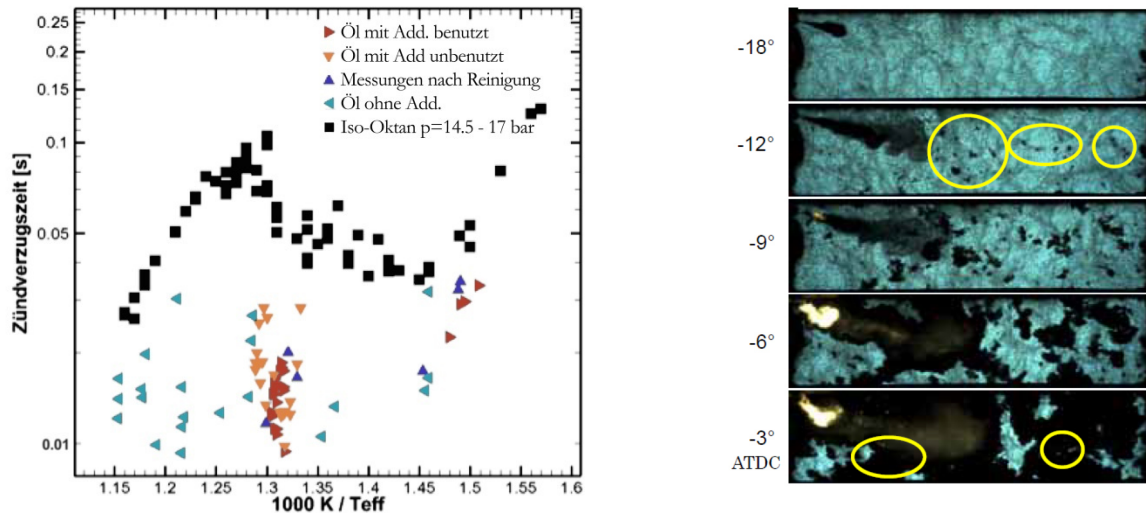


Figure 2.6: RCM measurements:
left: Autoignition delay times τ_i for a stoichiometric iso-octane-air mixture between 14.5 -17 bar (squares) and with addition of lubricating oil (triangles), from Palaveev et al. [32]
right: Shadowgraph images of irregular flame kernels (marked with circles) originating from oil droplets in front of the regular flame, from Yasueda et al. [25]

Yasueda et al. [33] performs high speed imaging on an RCM while placing lube oil on the piston surface to mimic HC accumulation. The results make clear that several irregular flame kernels develop originating from separated lube oil droplets leading to an accelerated combustion with knocking, see Figure 2.6 (right). Although this test is carried out with natural gas, a similar mechanism may also be valid for operation with gasoline.

Further experimental studies show strong influence of the oil composition on PI rates. As shown by Luef et al. [34] and Takeuchi et al. [35], the molecular structure of the base stock oil is decisive. In general, mineral and hydrocrack oils are more sensitive to pre-ignition than synthetic base oils like polyalphaolefines (PAO) or ester oils. Furthermore, oil additives with typical proportions ranging from 5 to 25 % can have a significant impact on PI tendency. Detergents on Calcium basis are shown to have a strong promoting effect on pre-ignition whereas anti-wear additives on zinc basis and friction modifiers like molybdenum compounds seem to reduce the PI tendency. The interactions between these additives are relatively complex what makes an optimisation difficult. Changing the different proportions also influences the oil durability, as shown by Fujimoto et al. [36]. This in turn

leads to an undesirable effect, as deteriorated or strongly aged oils are found to have a PI tendency that is about two times higher than that of fresh oil, see Luef et al. [34]. This is explained by oxidation processes taking place in the oil under persistent thermal load promoting the formation of acids. At the same time, the adsorption of reactive partially burned components, like radicals, is supposed to facilitate pre-ignition.

Besides the chemical factors influencing PI, especially the oil viscosity is found to have a significant impact on the evaporation loss and hence on PI frequency. Luef et al. [34] determine a critical viscosity range of 8–23 cSt at 40°C which turns out to be appropriate for several types of oils. It is argued that for lower viscosities a high evaporation tendency leads to a diesel-like homogeneous distribution of oil and hence local concentrations are too low for autoignition. On the other hand, for a higher viscosity, the resulting high boiling range will impede evaporation and hence sufficiently high concentrations of oil are also not given for autoignition. However, it should be stated that Luef et al. [34] apply oil dosing in the intake manifold leading to a fine oil mist entering the combustion chamber instead of a single drop. Therefore, it seems that these results are more related to the effect of dispersed oil that is contained in the breather gas than separated droplets from the piston crevice. However, the light-end components which are responsible for lower viscosity indices and higher evaporation losses are suspected to have a higher autoignition resistance than lower volatile components from the mid-boiling range. This effect seems to be the reason why Takeuchi et al. [35] and Palaveev et al. [26] do not find a general correlation between the evaporation behaviour and PI rates.

An experimental study on the process of single oil droplet ignition is carried out by Ohtomo et al. [37] in an RCM. An optical window allows observing the injected lubricant droplet and the subsequent formation of a flame kernel. The authors find that the ignition consistently originates from a stationary point in the vapour plume far behind the moving droplet, as can be seen from the sequence in [Figure 2.7](#).

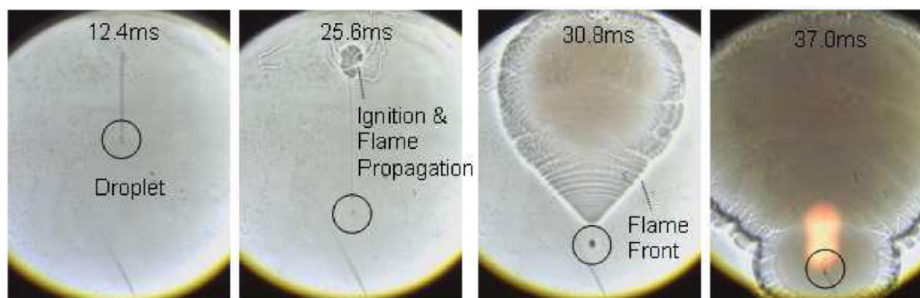


Figure 2.7: Shadowgraph images in an RCM showing ignition and subsequent flame propagation originating in the vapour cloud behind a falling oil droplet ($D_0 = 410 \mu\text{m}$, $T_{D0} = 610 \text{ K}$), from Ohtomo et al. [37]

The recordings suggest that a sufficiently high evaporation rate of the oil droplet, driven by its temperature, is the essential basis for the following autoignition reactions. Hence, the reactivity of the oil can only be decisive if the conditions for vapour ignition are already critical. Due to the fact that the boiling behaviour of typical fully formulated engine oils is in essence similar and cannot be modified arbitrarily, diminishing the reactivity of autoignitive spots seems to be a promising way to

avoid pre-ignitions. It is shown by Amann et al. [38] that already small amounts of cooled EGR between 6 % and 10 % significantly lower the likelihood as well as the intensity of LSPI. Ohtomo et al. [37] find that oil vapour autoignition and irregular flame propagation is observed regardless of dilution. In fact, the presence of inert gases retards the autoignition timing and reduces the flame speed of the developing flame kernel but cannot fully inhibit the ignition process itself. In this context it is stated that all parameters determining the flame speed of the background fluid like fuel type, stoichiometry or EGR are also influential factors for the severity of pre-ignition.

2.2.2. Hypothesis of Hot Solid Particle Induced Ignition

Although separated oil-fuel droplets with a high autoignition tendency are a plausible explanation for many experimental observations, there are several other studies claiming that hot particles play a key role for pre-ignition:

Already in the 1950s Withrow and Bowditch [39] applied flame photography and identified glowing airborne objects as premature source of ignition leading to “wild ping”. This was explained by a deteriorated fuel quality during wartime that caused heavily sooted combustion chamber walls. Pre-ignitions were observed primarily at the moment after switching to full-load operation. Bright spots appeared at arbitrary points in the combustion chamber just before autoignition occurred. Obviously detached deposit flakes were glowing and initiated irregular flame propagation accompanied by knocking.

Although fuels and deposition characteristics have significantly improved in the meantime, similar mechanisms still seem to be relevant: With high-speed endoscopy, Schünemann et al. [40] are able to capture the separation process of a single deposit flake from the combustion dome during the compression stroke. If such a particle is not completely consumed by the end of the combustion process and survives the exhaust stroke, it can become visible as a glowing moving spot that can act as a potential pre-ignition source. However, Schünemann et al. [40] state that glowing particles are only visible in 40 – 50 % of all recorded pre-ignition events. Okada et al. [41] describe that luminous flames occurring in regions with intensified wall wetting may indicate an excessive formation of deposits that can strip off and remain hot due to surface reactions until the next cycle. Other authors, like Palaveev et al. [26] fully exclude glowing particles as reason, since optical sensors detect no light emissions before an event that would indicate any combustion radiation. Consequently, the prevention of deposits seems to lower the risk of pre-ignition but may not to be the primary cause.

An impressive process occurring in the regular cycle prior to pre-ignition is captured by Döhler and Pritze [42] with high-speed endoscopy, see [Figure 2.8](#). It is found that a diffusively burning lump forms at the end of a regular burning cycle (image sequence in first row). The lump moves across the combustion chamber and subsequently breaks up into several smaller glowing objects (image sequence in second row). One of these bright spots is shown to survive gas exchange and to remain glowing during fuel injection and compression in the following cycle. Obviously, this spot subsequently serves as pre-ignition origin, preferably in the vicinity of hotter areas, like exhaust valves or spark plug (image sequence in third row).

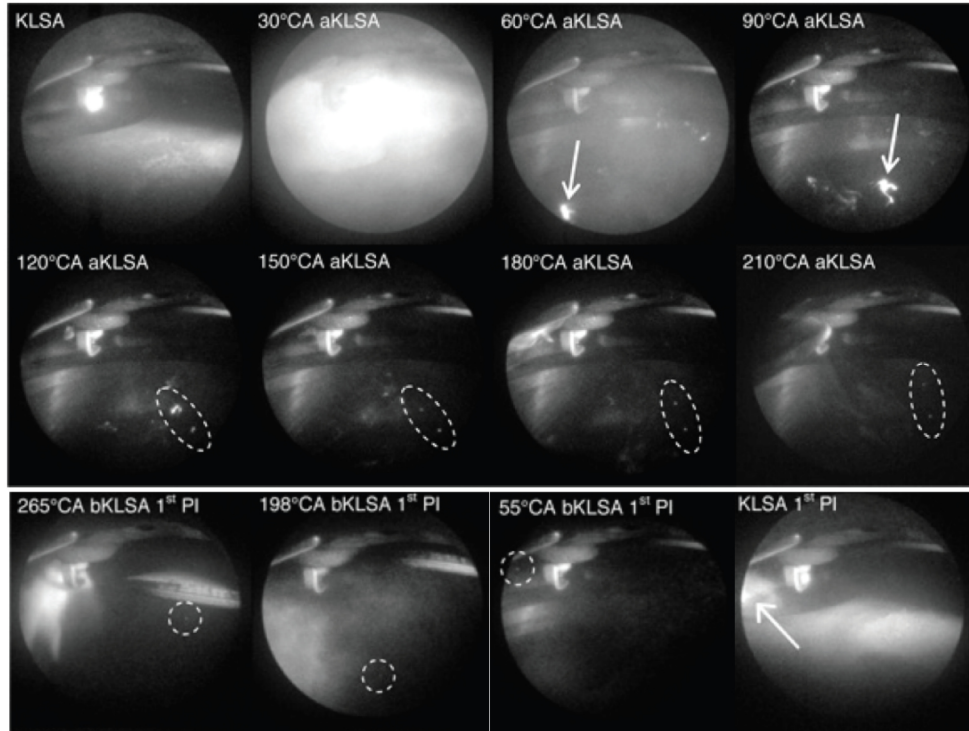


Figure 2.8: Formation of a moving diffusively burning lump after a regular combustion, generating smaller glowing objects that can act as pre-ignition source in the following cycle, from Döhler and Pritze [42]

The authors conclude that the vicinity of the initially burning lump to the cylinder liner supports the hypothesis of oil-fuel droplets being expelled from the piston crevice. However, the subsequent formation of glowing objects raises the question if these are burning liquid ligaments coming from the bursting lump or if the diffusive combustion leads to a rapid agglomeration of solid carbon. Bae and Avedisian [43] carry out single droplet combustion experiments with a kerosene derivative that has a boiling range between gasoline and engine oil. The results suggest that the burn duration of droplets with $D_0 \approx 500 \mu\text{m}$ would be largely sufficient to act as ignition source provided that it is not being discharged during the exhaust stroke. Furthermore, the analysis of the remaining soot shows that the maximum size of the individual near spherical aggregates is below 100 nm. This is significantly smaller than the diameter of 0.3 – 0.4 mm that was estimated by Döhler and Pritze [42] for the glowing object in Figure 2.8 apparently acting as pre-ignition source. The burning droplet theory, however, raises the question why the pre-ignition didn't set in substantially earlier towards IVC. Since lengthy processes, such as the ignition delay and the formation of a flame kernel are already finished for a remaining burning drop, the ignition of the charge would have been expected to be completed much earlier than around TDC.

The detailed mechanism leading to glowing objects is obviously challenging to be clarified. However, several studies reveal that bright moving spots may not necessarily have to be solid particles but rather burning droplets. This finding may relativizes other studies where glowing spots are interpreted as carbonaceous solid particles.

Due to the high complexity of the pre-ignition phenomenon, the relevant mechanism can be dependent on the examined engine configuration, operating parameters and boundary conditions. The behaviour of sophisticated liquid mixtures like fuel or oil during the physical and chemical processes leading to autoignition and flame propagation make it difficult to attribute experimental findings to the respective mechanism. However, in summary, recent work on the pre-ignition phenomenon suggests that it is characterised by:

- a) high boost levels and compression ratios causing a critical thermodynamic state of the charge
- b) injector sprays impinging on the liner and mixing with lube oil; influence of the fuel volatility
- c) HC accumulation in the piston crevice and droplet separation due to oil dilution
- d) droplet evaporation and mixing with the main hot charge leading to autoignition due to the lower ignition temperature of oil (droplet hypothesis)
- e) chemical composition of the base stock oil and oil additives
- f) burning droplets or particles creating hot spots that can ignite the main charge locally (particle hypothesis)
- g) Lambda, EGR rate and fuel type being present in the charge determining the stability of the propagating irregular flame kernel

2.3. Overview about the current Knowledge on Pre-Ignition

The following [Figure 2.9](#) provides a brief overview about the main results of previous research activities that were presented in the last sections. The study at hand focuses on an appropriate modelling strategy to clarify and to evaluate the plausibility of the droplet hypothesis.

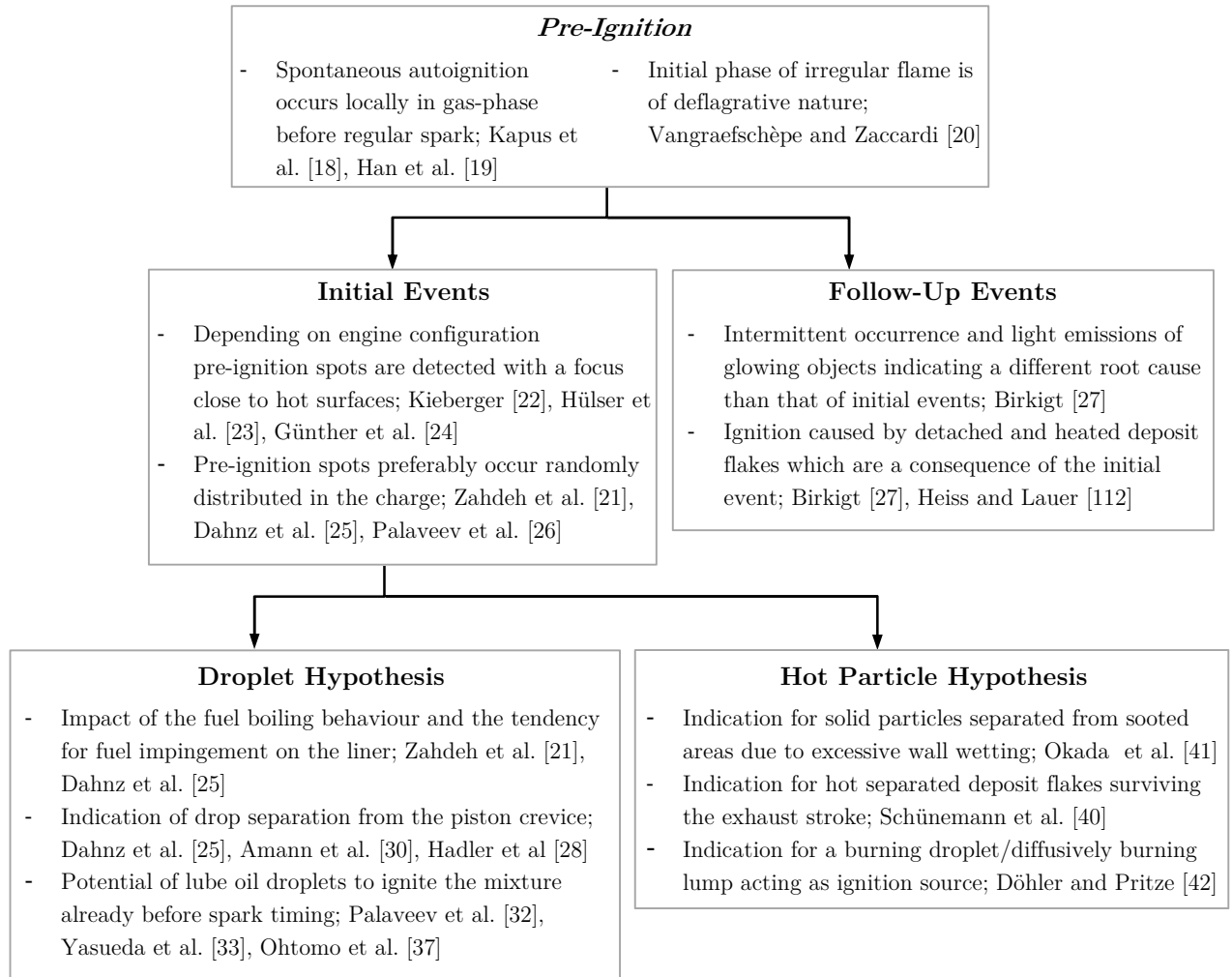


Figure 2.9: Overview about the main results of previous research projects

2.4. Pre-Ignition Modelling Strategies

Besides extensive experimental investigations on pre-ignition, only little attention was given to the development of theoretical modelling approaches. This is due to the uncertainty that exists on the formation of the autoignitive spot induced by complex chemical and physical mechanisms.

Several publications try to work out a general trend for the autoignition tendency of the charge on the basis of the ignition delay time τ . In order to deal with the varying conditions of pressure and temperature, the well-known Livengood-Wu-integral [44] for the prediction of knock timing can be applied for the charge during compression:

$$I(t) = \int_0^{t_0} \frac{1}{\tau(t, p, T)} dt \quad (2.1)$$

Assuming that the autoignition chemistry is cumulative, the value of the integral I describes the reaction progress and reaches unity at the moment of autoignition. Dahnz and Spicher [45] argue that for turbocharged engines under full load the autoignition characteristics is better represented by an integral ignition delay time τ_{int} that accounts for the thermodynamic history of the mixture. Results that are carried out in a homogeneous reactor model with a toluene reference fuel suggest that pre-ignition is impossible for mean conditions as well as for typical variations of the thermodynamic charge properties. Dahnz and Spicher [45] conclude that stochastic effects such as oil droplets are most likely responsible for a local reduction of the ignition delay time leading to premature ignition.

A numerical model for single fuel droplet ignition and combustion under constant boundary conditions is presented by Stauch et al. [46] considering the detailed transport processes between liquid and gaseous phase but without any experimental validation. This model is adopted by Palaveev et al. [32] to study the autoignition timing of lubricant droplets under engine relevant conditions. Even at elevated gas temperatures at compression-start up to 380 K and droplet temperatures up to 470 K no ignition can be observed before TDC. However, physical properties of n-hexadecane $C_{16}H_{34}$ and chemical kinetics of n-heptane C_7H_{16} are used to mimic the evaporation and autoignition behaviour of long-chain lubricating oil without experimental validation, what seems to be a severe simplification. It is argued that the ignition delay of linear n-alkanes between C7 and C16 is of the same order, as demonstrated by Westbrook et al. [47]. It is further stated that n-alkanes are generally not reactive enough to trigger pre-ignition. Based on experimental observations, organometallic substances included in oil-additives are suspected to accelerate oil chemistry and to promote pre-ignition.

Blin-Simiand et al. [48] identify experimentally that stable intermediate species like highly reactive ketohydroperoxide decrease the ignition delay of hydrocarbons. Such partially oxidised species are likely to accumulate in crevices close to walls and thus can enter the combustion chamber via detached droplets. Further numerical studies by Palaveev et al. [32] in a homogeneous reactor model confirm the accelerating influence of ketohydroperoxides on autoignition. The ignition delay time is shown to decrease about one order of magnitude with the addition of lowest mass fractions of ketohydroperoxide.

Ohtomo et al. [37] simulate the single droplet evaporation and ignition process with a numerical model in order to study the RCM experiment of a falling oil droplet. The autoignition characteristic of the oil is represented by n-heptane C_7H_{16} , the boiling behaviour is modelled with a six component approach ranging from C8 to C27. With the simple chemistry of n-heptane again no ignition is noticed before TDC. In their RCM experiments, Ohtomo et al. [37] find a minimum initial droplet temperature of 470 – 520 K that is necessary for droplet vapour induced ignition before TDC. For the calculations on an SI engine, a very low initial droplet temperature of 330 K is assumed at IVC. The results suggest that a droplet cannot be sufficiently heated for autoignition during compression. However, it is unclear whether autoignition would have been possible for droplets with an initial temperature lying closer to typical surface temperatures inside the combustion chamber.

From the previous studies it can be concluded that beside the autoignition behaviour of oil, the evaporation and hence the droplet and gas temperatures are the driving factors for a premature ignition. The complex physical and especially chemical properties of oil are often approximated with simple hydrocarbons without detailed experimental validations. Furthermore, most modelling approaches do not account for temperature inhomogeneities or other stochastic influences, what is especially critical when examining temperature dependent autoignition processes.

3. Objective of the Investigation

The general task of the present work is to find a modelling strategy to validate the hypothesis of droplet induced low speed pre-ignition. Endurance tests on a turbocharged direct injection spark-ignition engine under pre-ignition critical operating conditions are the basis to statistically evaluate the phenomenon. Additionally, high-speed images of pre-ignition events recorded through an endoscopic access are interpreted to describe the spatial characteristics of the ignition processes and to derive an appropriate modelling approach. For that reason, engine process simulation, 3D-CFD simulation and reaction kinetic simulation are combined to account for the physical as well as the chemical processes leading to a premature ignition of the charge.

In a first step, a three-pressure-analysis is conducted to account for cyclic fluctuations of possible influential charge properties on pre-ignition. To account for inhomogeneities, such as emerging from droplets, sub-models for injection and droplet-wall interaction are validated for the CFD simulations.

Though attempts have been published about droplet evaporation and ignition, there is still a lack of knowledge on the particular behaviour of oil droplets inside the combustion chamber and their reactive impact. Therefore, the present work will include a systematic study of the entire process chain leading to droplet induced pre-ignition. To account for the detailed evaporation behaviour of fuel and oil in the hot cylinder charge, multi-component surrogate fluids are introduced for CFD. Critical fuel impingement leading to oil dilution is analysed in view of a potential separation of oil-fuel droplets. The resulting dispersion of such droplets and their probability to survive until compression-end and to serve as an igniting spot is further investigated.

The autoignition chemistry of oil is yet unclear. Therefore, an approach will be developed to capture the autoignition behaviour of oil with detailed chemical kinetics. A calibration with experimental single droplet studies is conducted to allow statements about critical oil vapour fractions which are necessary for pre-ignition. Critical droplet properties are finally determined in a statistical way.

The presented work should provide a basic understanding of the physical and chemical processes that lead to pre-ignition. Based on the gained knowledge, appropriate measures may be implemented in future engine developments for an improved exploitation of the fuel-economy while significantly reducing the damage potential of pre-ignition.

4. Autoignition Fundamentals

Findings from the literature survey suggest that pre-ignitions most likely occur distant from surfaces. Additionally, it is stated that obviously a flame of deflagrative character propagates away from the autoignition centre leading to a second autoignition in the end-gas accompanied by heavy knock. For this to occur, four conditions must be satisfied according to [49]:

- a) The autoignition delay time τ must be small enough for autoignition to occur at a reactive spot on a sufficiently short time scale
- b) The size of the reactive spot must not be less than the critical radius for autoignition r_c
- c) For the autoignited spot to initiate a flame, its radius must not be less than the critical radius for flame propagation, r_f
- d) For a premature flame propagation to trigger super-knock, end-gas autoignition has to lead over into a developing detonation

The fundamentals and theoretical background of each individual condition are presented in the following sections.

4.1. Oxidative Characteristics of Hydrocarbons

Knocking and pre-ignition are both autoignition phenomena but occur at considerable different conditions of pressure and temperature. Basically, the chemical mechanisms behind hydrocarbon oxidation can be subdivided into low, intermediate and high temperature regimes see [Figure 4.1](#). The transitions between these areas are smooth and dependent on the molecular structures of the fuel, temperature and pressure.

For the initiation of knocking, both the low and intermediate chemistry is of importance, what can be seen by means of the red end gas trajectory depicted in [Figure 4.1](#) which was calculated in a stochastic reactor model. The timing of autoignition is characterised by a yellow symbol and arises in the intermediate region. In contrast, for pre-ignition that usually occurs towards the end of the compression stroke, the low-temperature regime is of highest importance, see the green trajectory in [Figure 4.1](#).

The ignition of hydrocarbon-air mixtures is a complex process that involves a large number of chemical reactions. In a first chain initiating step, highly reactive radicals are produced from stable molecules. These radicals react in several chain-propagating paths, whereby the overall number of radicals is constant. Only an increase of radicals due to chain-branching reactions can lead to fast reactivity of the system. Furthermore, chain reactions can terminate if two radicals form a stable molecule. The excess energy is then absorbed by a chemically non-involved collision partner. The requirement for chain explosion and hence ignition is met if the rate of chain-branching becomes greater than the rate of chain termination [50].

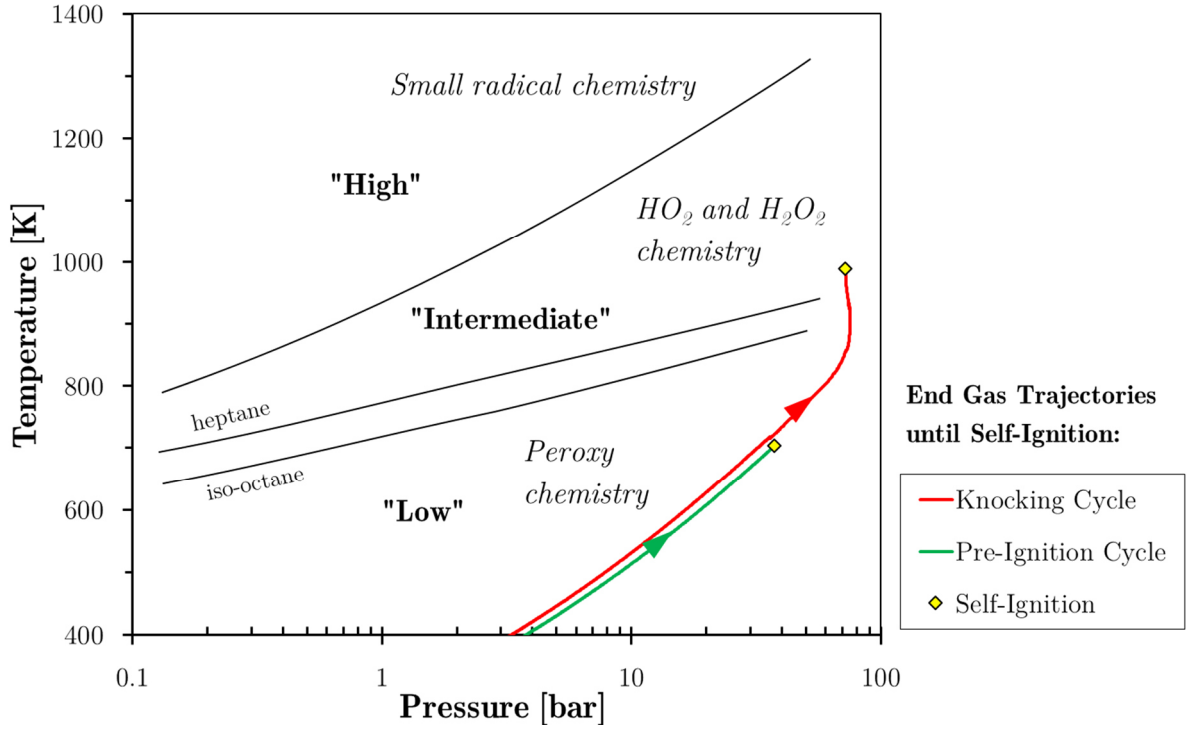


Figure 4.1: Regimes of hydrocarbon oxidation depending on pressure and temperature [51] supplemented by typical trajectories of end-gas mean conditions until self-ignition for knocking and pre-ignition

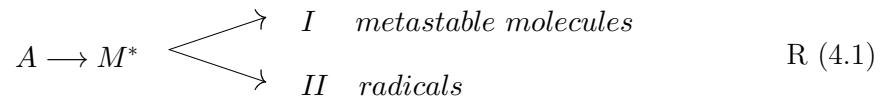
The reaction rates of chemical reactions show a strong temperature dependency and hence also the heat release of exothermic reactions. The rate constant k usually follows the exponentially law of Arrhenius:

$$k = A \cdot \exp\left(-\frac{E_a}{RT}\right) \quad (4.1)$$

A is the kinetic pre-exponential factor that has a mild temperature dependency ($A = A'T^n$) for most binary elementary reactions which is generally neglected [50]. To launch a reaction, an energy barrier must be exceeded. This energy is referred to as activation energy E_a of the reaction. If the heat released by a reaction exceeds the heat loss to the surroundings, the temperature of the system increases. This leads to a rapid acceleration of the reaction rate due to its exponential dependence and is called thermal explosion [52].

Chain-branching explosions are mostly coupled with exothermic reactions. Therefore a thermal feedback exists that leads to a self-acceleration of the reaction rates and the formation of radicals. This means that chemical and thermal explosion are occurring simultaneously [52].

Under certain conditions of pressure and temperature the reaction progress in hydrocarbon oxidation can be decelerated or inhibited even though the temperature increases. This is due to so called degenerate branching reactions [52]:



At low temperatures, unstable intermediates M^* formed from the fuel A react along route II to form radicals via chain-branching. The released energy increases the temperature of the system. As the temperature is raised, the non-chain-branching route I is preferred as its activation energy is higher than that of route II [50]. This leads to an accumulation of metastable intermediates that need even higher temperatures to decompose. This occurs after a certain induction time to finally provide chain-branching and ignition. An induction time is typical for hydrocarbons and is responsible for the so called negative temperature coefficient (NTC) of rate of reaction.

The kinetic behaviour of hydrocarbon oxidation is often evaluated in logarithmic Arrhenius plots where the reaction rate k or the ignition delay time τ is depicted over the reciprocal of absolute temperature $1/T$. [Figure 4.2](#) shows that the NTC behaviour of n-heptane just occurs below 1000 K. With increasing pressure the NTC region shifts to higher temperatures and gets less pronounced. The two solid lines in Figure 4.2 indicate the slopes corresponding to the activation energies for the high temperature route along I and the low temperature route along II , respectively of R (4.1) [53].

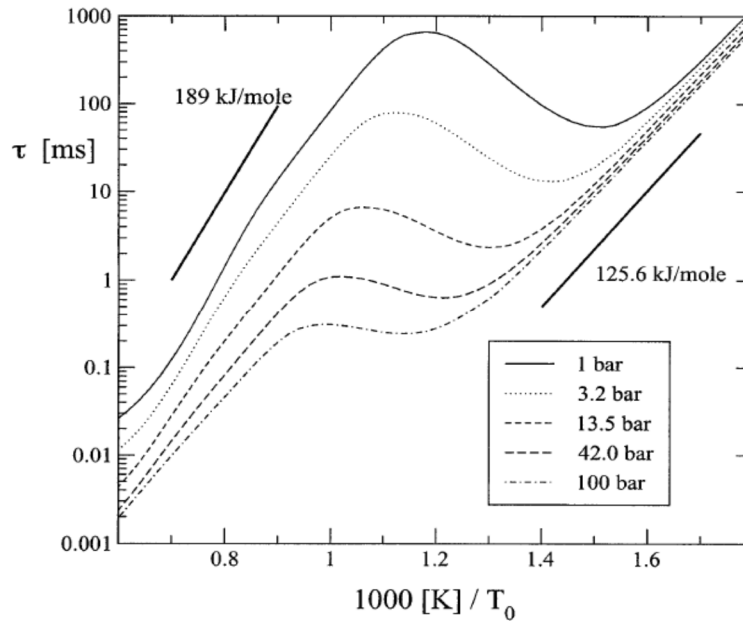


Figure 4.2: Ignition delay times of n-heptane for different pressures [53]

The following chapters deal with the chemical mechanisms and the kinetic aspects that are responsible for the NTC behaviour. The ignition delay decides about the occurrence and severity of irregular autoignition in an engine cycle. Detailed knowledge about the thermo-kinetic processes is therefore crucial.

4.1.1. Low Temperature Chemistry

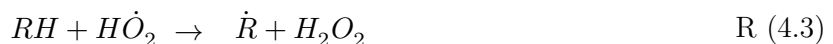
In the following, the considered hydrocarbon is denoted as RH , whereas an active radical is characterised by a dot ($\dot{}$). Organic radicals with free valences due to internal hydrogen abstraction are denoted via ($\dot{}'$).

Basically, the oxidation of hydrocarbon fuels RH starts with a chain initiation step, where an initial active radical is formed from a stable species, most likely via the reaction:



This initiation reaction is relatively endothermic ($> 160 \text{ kJ mol}^{-1}$). Therefore, sensitisation or initiation at the surface may be necessary at low temperatures [51]. Furthermore, the reaction rate of R (4.2) is slow at low temperatures and therefore responsible for long induction periods [52].

If there are other radicals available in the low temperature region, typically OH or HO_2 , they react with the fuel to form alkyl radicals R :



Since these reactions are very fast, the concentrations of OH or HO_2 remain low what inhibits thermal ignition [54].

The next oxidation step is the addition of molecular oxygen to form peroxy radicals RO_2 :



The activation energy of the addition reaction is almost zero [52], whereas the reverse dissociation reaction shows a high activation energy of $\approx 120 - 150 \text{ kJ mol}^{-1}$ [51]. This suggests that the equilibrium of R (4.5) is strongly dependent on temperature. At low temperature the equilibrium lies to the right and subsequent chemistry of RO_2 leads to branching. With increasing temperature, the equilibrium shifts to the left and termination through R is favoured, what leads to retarded reactions. This thermo-kinetic dependency is the reason for the NTC behaviour. Because of its importance for the processes in oxidation mechanisms R (4.5) is called the “heart of combustion chemistry” [51]. [Figure 4.3](#) gives a good overview of the adjacent reactions centred around the reversible step $R + O_2 \rightleftharpoons RO_2$, exemplarily for n-heptane.

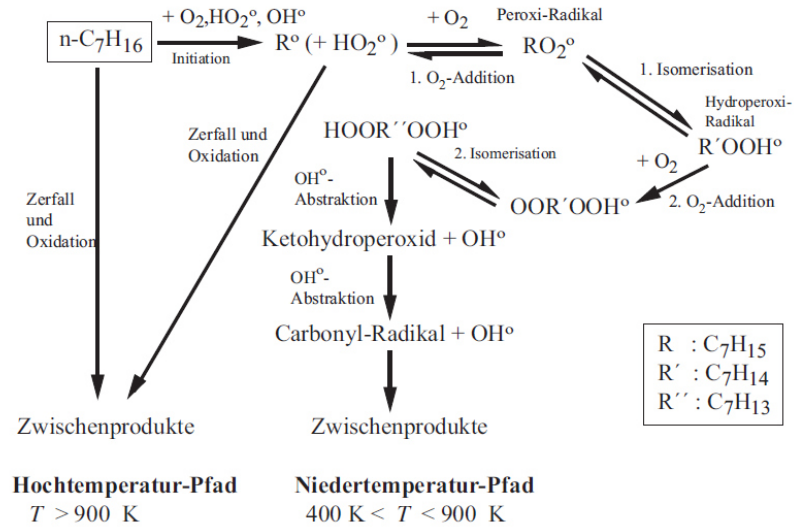


Figure 4.3: Principle of low and high-temperature oxidation of n-heptane [54]

In the low temperature range, R (4.5) is followed by reactions with RO_2 . These can abstract hydrogen atoms from other molecules in an external hydrogen abstraction to form hydroperoxy compounds $ROOH$. Possible hydrogen donors are fuel molecules or intermediates like formaldehyde:



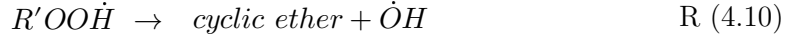
The following homolysis reaction of $ROOH$ gives highly reactive alkoxy and OH radicals:



This chain branching reaction is relatively slow contributing to a lengthy first induction period [51]. As the temperature is raised, the production of $ROOH$ declines and the fast internal hydrogen abstraction with higher activation energy becomes more important to form the alkylhydroperoxy radical $R'OOH$:



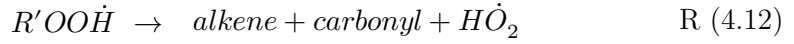
The rate and number of reactions leading to $R'OOH$ increases with the fuel molecule size and are fastest in long linear alkanes. This is a crucial point determining the autoignition sensitivity of fuel or oil. For more complex fuels consisting of highly branched molecules R (4.9) gets slow and hence impedes or even inhibits ignition. Such fuels are characterised by high octane numbers [55]. The formed hydroperoxy radical can react in several ways, the most important are R (4.10)–R (4.12) [56]:



or



or

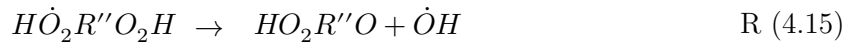


The reactions R (4.10)–R (4.12) only produce a single OH or HO_2 radical and are effectively chain propagation steps. Ignition is only possible along another path with a second oxygen addition, see R (4.13). The formed dihydroperoxy radical $O_2R'O_2H$ is the basis for further branching:



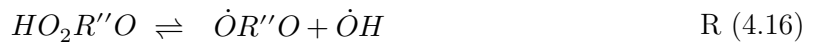
The reactions of $R'OOH$ play a central role in the low temperature kinetics. Especially the competition of R (4.10)–R (4.12) with R (4.13) has a notable influence on the first induction time [56].

After the second hydrogen abstraction in R (4.14) the formed $HO_2R''O_2H$ decomposes into alkylketohydroperoxide $HO_2R''O$ and a hydroxyl radical OH due to its weak O-O bond:



The OH radical formed in R (4.15) reacts preferably with the fuel according to R (4.4) and starts a new chain via the alkyl radical R . In this way a slow decomposition of the fuel takes place, what becomes obvious in a long first induction period τ_1 of the ignition process, especially at low temperatures, see [Figure 4.4](#) [54].

Up to this point, the reactions along the path of $R'OOH$ only served for the propagation of the chain without branching. Alkylketohydroperoxide is relatively stable and needs a high activation energy of ca. 180 kJ mol⁻¹ [57,58] to decompose into a carbonyl radical $OR''O$ and a hydroxyl radical OH :



Because of the high activation energy of R (4.16) it can be seen as a “bottleneck” for the ketohydroperoxide concentration to build up until the fuel is consumed by OH radicals of R (4.15) [58]. When the fuel is increasingly depleted, OH radicals can accumulate and chain branching takes place via R (4.16). The subsequent decomposition products help to accelerate the overall rate of fuel oxidation, raising the temperature and allowing the remaining ketohydroperoxide species to decompose more easily [58]. This leads to a rapid heat release, being visible as a moderate step in the pressure trace in [Figure 4.4](#) at the end of the first induction period τ_1 . This first heat release is accompanied by moderate light emissions which are also denoted as a “cool flame”.

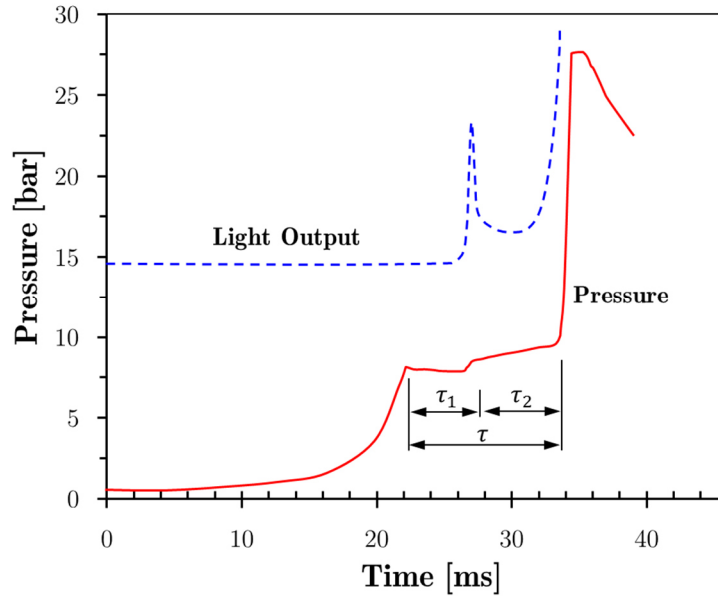
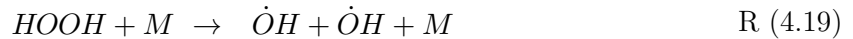


Figure 4.4: Measured ignition delay time in an RCM for n-pentane for a compressed gas temperature of 740 K (left) [59]

4.1.2. Intermediate Temperature Chemistry

With the temperature increase caused by the cool flame, the products of the chain propagating reactions R (4.10)-R (4.12) become more important what retards the overall reaction rate [60]. Furthermore, the equilibrium of R (4.5) shifts increasingly to the left leading to reactions of HO_2 and H_2O_2 .



The decomposition of H_2O_2 in R (4.19) proceeds very slow. The resulting OH radicals react with the fuel at almost constant temperature until the latter is fully depleted [53]. This is the reason for the flat rise of the pressure in the second induction period τ_2 , see Figure 4.4. Once the fuel is consumed, the OH radical concentration rises abruptly leading to a hot ignition of the second stage [53]. This effectively occurs at higher temperatures, typically 900 to 1200 K at a pressure of 7 to 60 bar [51,61].

The reasons for the increase of τ_2 as the compressed gas temperature is raised (see [Figure 4.5](#)) are connected to the equilibrium shift of the degenerate branching reaction R (4.5), which is one of the major exothermic reactions in the low temperature region [62]. With increasing equilibrium to the

left, the heat release of the first stage is significantly reduced leading to lower reactant temperatures at the onset of the second stage and therefore longer periods of τ_2 [63,59].

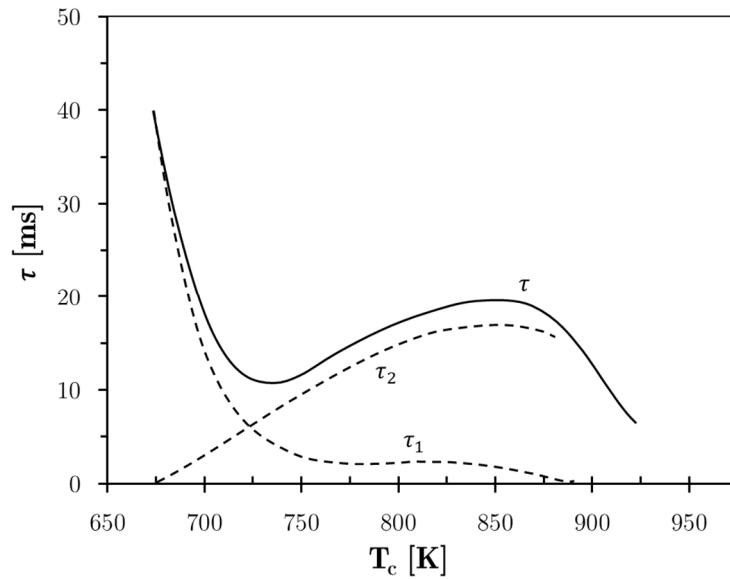


Figure 4.5: Variations of τ_1 and τ_2 as a function of compressed gas temperature in an RCM at a pressure of 7 bar [51,59]

Figure 4.6 illustrates ignition delay times for several n-alkanes, iso-octane and toluene. Basically, with decreasing carbon chain length and more complex molecule structures, the reactivity diminishes what is reflected by longer ignition delays [51]. The distinct difference in reactivity of the two primary reference fuels n-heptane and iso-octane can be found in their tendency for internal isomerisation in R (4.9) and R (4.14). Iso-octane has a strong primary C-H bond which can hardly be broken whereby an abstraction of the H-atom gets slow. N-heptane in contrast has a long linear chain of only secondary C-H bonds and can undergo the isomerisation reactions more easily [64]. Aromatic hydrocarbons, such as toluene neither exhibit degenerate branching via R (4.5) nor isomerisation. This leads to inhibited low temperature reactions below ~ 850 K and causes a high autoignition resistance.

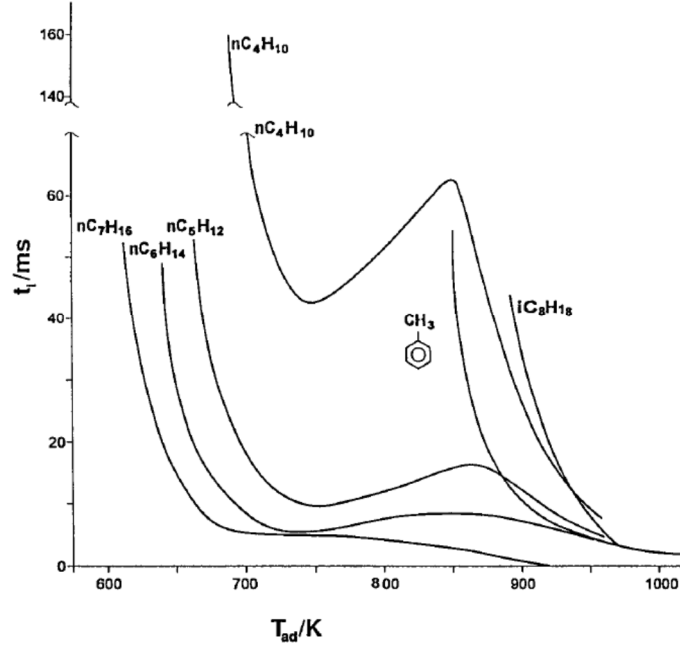


Figure 4.6: Measured ignition delay times in an RCM for normal alkanes, iso-octane and toluene at a pressure of 7 bar [63]

4.1.3. High Temperature Chemistry

After first and second stage ignition, high temperatures above 1000 K are prevailing and the small radical chemistry takes over leading to an evolution of a flame kernel with subsequent flame propagation. In lean and moderately rich flames the hydrocarbon is immediately attacked by radicals which are due to R (4.19) and thermal decomposition. These radicals are O , H , and primarily OH and are denoted as X :



The resulting alkyl radicals R originating from higher order alkanes are unstable at high temperatures and break down to even smaller alkyl radicals as long as the stable methyl CH_3 or ethyl radical C_2H_5 is reached, see [Figure 4.7](#). Thus, the problem of even higher order alkane oxidation can be reduced to methyl and ethyl radicals which are well known from vast studies about methane CH_4 and ethane C_2H_6 oxidation [65].

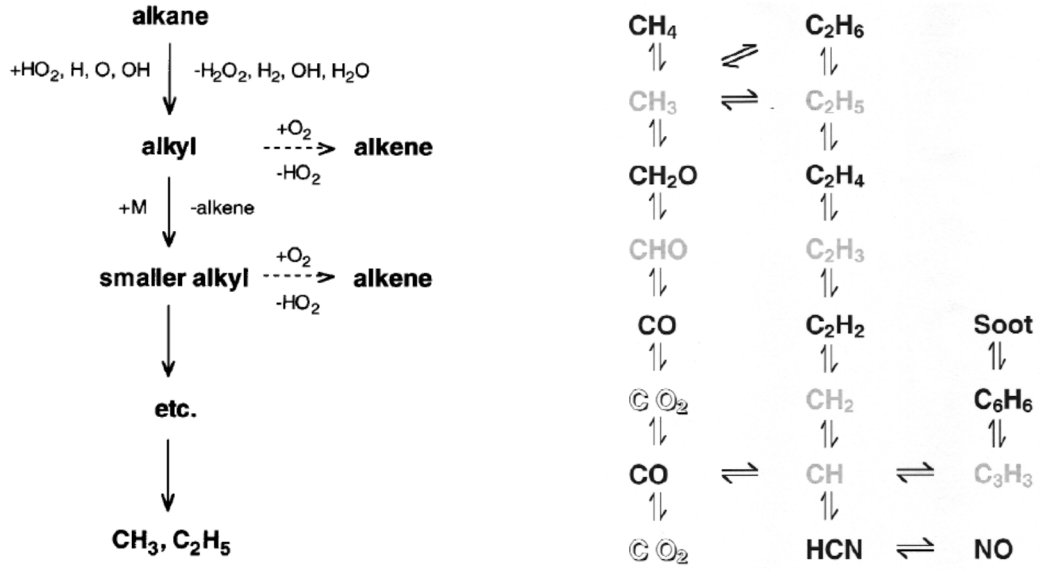


Figure 4.7: High temperature decomposition of alkanes into small methyl CH_3 and ethyl radicals C_2H_5 with successive oxidation steps [65]

The decomposition of the methane molecule with OH via R (4.20) is relatively slow in comparison to the oxidation of carbonmonoxide CO :



This is the reason why early in the methane system CO accumulates and later, when the CO concentration rises, it effectively competes with methane for OH radicals and the fuel consumption rate is slowed. Finally, the large amounts of carbon monoxide formed are oxidized to carbon dioxide and most of the heat released from the overall reaction is obtained [50].

4.2. Single Droplet Ignition

Droplet ignition and combustion is frequently encountered in various applications such as diesel engines or gas turbines. In gasoline engines, droplet ignition does not occur under normal conditions, but is rather a potential source of irregular premature ignition.

For droplet ignition to occur, fuel and oxidiser must be well mixed in an environment with sufficiently high temperature. The process involves heat transfer to the droplet, evaporation to produce fuel vapour, mixing with air and heating of the mixture until chemical reaction become fast enough for thermal runaway and combustion of the vapour.

Droplet Evaporation

The performance of the ignition process depends mostly on the vaporisation and heating of the droplet. As shown in [Figure 4.8](#) (left), a droplet exposed to a hot environment is heated up by conduction and vaporises the liquid at the surface. The vapour produced diffuses outwards from the surface because of the arising concentration gradient.

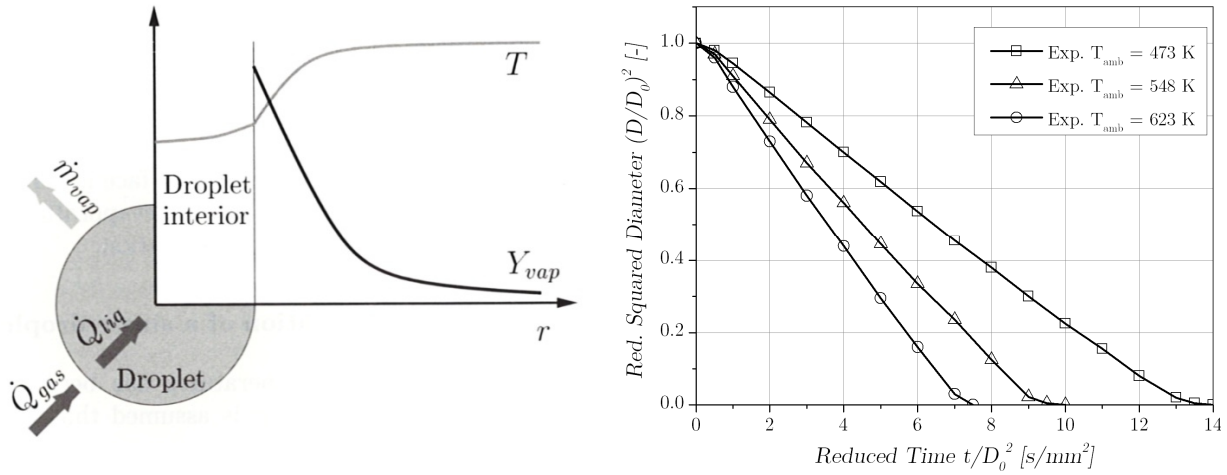


Figure 4.8: Schematic representation of droplet evaporation with temperature and fractions of fuel shown qualitatively as a function of radial distance (left) [66]; N-heptane droplet evaporation experiments showing that the square of the droplet diameter decreases linearly with time, $D_0 = 0.25$ – 0.7 mm (right) [67]

In the 1950s Godsave [68] and Spalding [69] formulated the D^2 -law, stating that the square of the droplet diameter decreases linearly with time during evaporation, as shown in Figure 4.8 (right):

$$D^2(t) = D_0^2 - \beta_v t \quad (4.2)$$

$$\text{with} \quad \beta_v = \frac{8\rho_a \mathfrak{D}_{12}}{\rho_{liq}} \cdot \ln(1 + B) \quad (4.3)$$

In these considerations β_v is the evaporation coefficient that is depending on ρ_a the density of the gas surrounding the droplet, ρ_{liq} the density of the droplet liquid and \mathfrak{D}_{12} the diffusion coefficient of the evaporated liquid as substance 1 in the gas with index 2. B is the Spalding transfer number, given by:

$$B \equiv \frac{w_{1,\infty} - w_{1,S}}{w_{1,S} - 1} \quad (4.4)$$

In this equation, $Y_{1,S}$ denotes the fuel mass fraction at the surface and $w_{1,\infty}$ the fuel mass fraction far away from the droplet. The evaporation process can be approximated with the D^2 -law over wide ranges. However, when heat conduction within the droplet is taken into account, deviations are found. This becomes obvious in the initial phase of droplet heating, as can be seen in Figure 4.8 (right).

Droplet Ignition

As fuel vapour moves away from the droplet surface due to diffusion and convection (Stefan flow), ambient air has to diffuse in the other direction to keep the pressure constant. In this way, a zone of roughly stoichiometric proportions forms at some distance from the surface. Chemical reactions begin in this mixture and ignition occurs in a similar manner as in the homogeneous gas phase (see Section 4.1), as shown for an n-heptane droplet in Figure 4.9 (left).

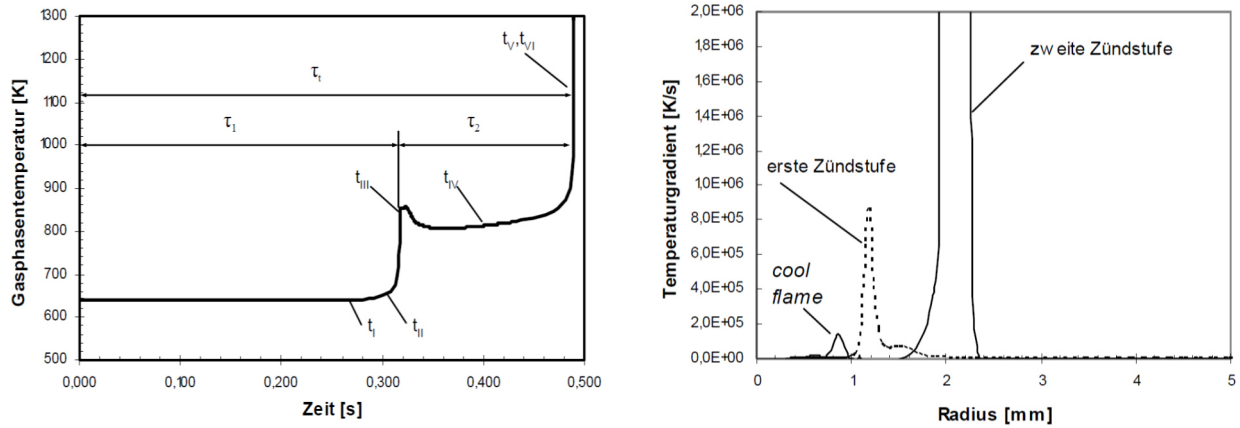


Figure 4.9: Gas-phase temperature during the droplet autoignition process (left) [70]; Temperature gradient showing the radial position of different stages during autoignition of an n-heptane droplet with $D_0 = 0.7$ mm (right) [70]

However, the heterogeneous distribution of vapour and temperature in the vicinity of the droplet surface results in a highly transient behaviour of the chemical reactions, as shown by Schnaubelt [70] with a detailed reaction kinetic droplet ignition model:

Exothermal pre-reactions in the low temperature regime lead to an accumulation of relatively stable alkylketohydroperoxide $HO_2R''O$ that gets depleted in the cool flame, see reaction R (4.16). The initial occurrence of the cool flame indicates the first stage of ignition with a local maximum of the temperature gradient in a certain distance to the drop surface, see the dashed line in Figure 4.9 (right). During an induction time, the cool flame continues to burn and steadily moves towards the

droplet surface where lower air-fuel ratios are prevailing. This increasingly heats the droplet surrounding what finally leads to the rapid hot ignition further away from the surface. A remarkable characteristic of droplet ignition is the fact that the cool flame still persists after ignition during the entire combustion phase, as can be seen by the second lower peak of the temperature gradient in Figure 4.9 (right) with a solid line. Obviously, the temperature close to the liquid surface remains below the threshold temperature what enables the low-temperature pathway of reaction R (4.2) along the peroxy radical chemistry to form alkylketohydroperoxide $HO_2R''O$. Convection and diffusion processes move this species outwards where it is consumed in the cool flame. In this way the first stage of ignition is continuously active where the fuel gets decomposed and pre-heated for the final combustion in the hot flame.

4.3. Requirement for Thermal Ignition

When the rate of thermal energy release is greater than the rate of thermal energy dissipation, an explosive condition exists. The same holds for chain explosion, when the rate of chain branching becomes greater than the rate of chain termination. This concept was first presented in analytical form by Semenov [71] and later in more exact form by Frank-Kamenetskii [72], who considered a spatial variation of the temperature T within the reacting system.

Frank-Kamenetskii [72] proposed the heat conduction equation for a spherical volume with radius r , as:

$$\underbrace{\frac{\lambda}{r} \cdot \frac{d}{dr} \left(r^2 \frac{dT}{dr} \right)}_{\text{thermal loss}} + \underbrace{A \cdot H_R \cdot \exp \left(-\frac{E_a}{RT} \right)}_{\text{chemical heat production}} = 0 \quad (4.5)$$

Where λ is the thermal conductivity, A the Arrhenius reaction rate, H_R the enthalpy of reaction in unit volume and E_a the activation energy. The term on the left describes the heat loss solely by conduction what is the major mode for gaseous systems. The heat loss is balanced by chemical heat generation expressed in an Arrhenius manner. Details on the solution of equation (4.5) can be reviewed for example in Glassman [50]. Finally, the thermal ignition theory yields a critical radius r_c for a reactive spot:

$$r_c = \sqrt{\frac{\delta_c \lambda T_a}{A Q E_n \exp(-E_n)}} \quad (4.6)$$

Where δ_c is the critical Frank-Kamenetskii parameter and $E_n = E/RT_a$ with the ambient temperature T_a . The value for δ_c is depending on the shape of the reactive volume and was numerically determined as $\delta_c = 3.43$ for a sphere.

It follows, that for a reactive centre with a radius $r > r_c$, exothermal reactions are sufficient to increase temperature. This further accelerates chemistry and finally thermal runaway leads to autoignition. The term $E_n \exp(-E_n)$ in equation (4.6) is dominant and increases rapidly with higher temperatures T_a or lower activation energies E . Consequently, the critical radius for autoignition

gets smaller for more reactive mixtures and higher ambient temperatures T_a . The pressure dependency is included in the pre-exponential factor A , with $A \propto p^n$, where n is the order of the reaction.

Kalghatgi and Bradley [49] calculated that for a stoichiometric n-heptane air mixture under critical conditions for pre-ignition ($T_a = 682$ K at $p = 37$ bar) equation (4.6) gives a value of $r_c = 0.54$ mm. For even more critical conditions ($T_a = 763$ K at $p = 37$ bar) r_c is reduced to 5.6 μm . These values reveal that a reactive zone is able to trigger autoignition already at very small scales.

4.4. Initial Flame Kernel and Flame Propagation

Requirement for a Self-Sustaining Flame Kernel

Gas-phase autoignition is a necessary but not a sufficient condition for the formation of a flame kernel that can propagate outward in a sustained manner. The amount of heat and radicals deposited in the kernel must be sufficient to raise the kernel temperature otherwise the resulting flame kernel decays rapidly because of heat conduction and radicals recombine faster than they are generated by chemical reactions. Zeldovich et al. [73] propose that a reactive spot must exceed a critical radius r_f in order to initiate flame propagation:

$$r_f = \delta_l \cdot \exp\left(\frac{Ze}{2}\left(1 - \frac{1}{Le}\right)\right) \quad (4.7)$$

Where, the laminar flame thickness δ_l is given by the kinematic viscosity divided by the laminar flame speed ν/s_L . The dimensionless Lewis number Le and Zeldovich number Ze are defined as:

$$Le = \frac{\alpha}{\mathfrak{D}} \quad , \quad Ze = \frac{E(T_b - T_u)}{RT_b^2} \quad (4.8)$$

The Lewis number Le describes the relation between thermal diffusivity α and mass diffusivity \mathfrak{D} and hence the balance between heat and radicals in the reaction zone. The Zeldovich number characterises laminar flames depending on the burned T_b and unburned T_u gas temperature.

For given values of Le (close to 1 for stoichiometric mixtures) and Ze (order of 10), r_f is proportional to the thickness of the laminar flame δ_l . It follows, that the necessary size for an autoignitive spot to initiate flame propagation decreases for a lower kinematic viscosity ν and a higher laminar flame speed s_L . For a stoichiometric iso-octane air mixture at pre-ignition critical conditions ($T_a = 763$ K at $p = 37$ bar), Kalghatgi and Bradley [49] obtain a critical radius of $r_f = 4.1$ μm . The minimal radius for autoignition $r_c = 5.6$ μm that was presented in the last section already exceeds this value and hence it is possible for a flame to propagate from the reactive spot. Besides, considering values of different fuels is justified in this case because of the similar laminar flame speed s_L of iso-octane and n-heptane that yields comparable values of r_f .

Thermodynamic and Physical Effects on Flame Propagation

In the early stage of flame development, the flame propagates roughly spherical in shape with laminar flame speed s_L . This is an important property of a combustible fuel-air mixture and is often defined with an empirical approach depending on the mole fraction of burned gas \tilde{x}_b , pressure p and unburned zone temperature T_u :

$$s_L(\tilde{x}_b) = s_{L,o}(\tilde{x}_b = 0) \left(\frac{T_u}{T_0} \right)^\alpha \left(\frac{p}{p_0} \right)^\beta (1 - 2.06 \tilde{x}_b^{0.77}) \quad (4.9)$$

Where $s_{L,o}$, α and β are fuel dependant constants for a given air-fuel ratio which are determined experimentally and can be found for gasoline in Metgalchi and Keck [74]. The burning velocity peaks slightly rich of stoichiometric for many hydrocarbons and gasoline. Exponent α is usually positive what leads to an accelerated flame speed at higher temperatures. This can be explained by the relatively high activation energy of hydrocarbon oxidation processes what makes flame speed quite sensitive to the flame temperature. In contrast, for higher pressures the flame speed decreases and thus exponent β gets negative. This can be explained by the diffusion coefficient that is inversely proportional to the pressure [61]. Thus, radical diffusion into the reaction zone gets slower with increasing pressure. This effect is further enhanced by strong pressure dependant third-order reactions involving three molecules, such as:



Where M is the usual third body that takes away the energy necessary to stabilise highly reactive H and O_2 in form of the relatively unreactive hydroperoxy radical HO_2 . At higher pressures, the possibility for trimolecular reactions increases essentially what inhibits overall reactions and hence reduces flame speed.

Beside thermodynamic effects, the flame speed heavily depends on the turbulence of the flow field. The Reynolds averaged approach is the classical way to describe turbulence as the local velocity u to consist of a mean velocity \bar{u} and a fluctuation u' :

$$u_\alpha(x, y, z, t) = \bar{u}_\alpha(x, y, z, t) + u'_\alpha(x, y, z, t), \quad \text{where } \overline{u'_\alpha} = 0 \text{ and } \alpha = 1, 2, 3 \quad (4.10)$$

Assuming isotropic turbulence ($u' = u'_1 = u'_2 = u'_3$), the turbulent intensity u' may be expressed as the root-mean-square velocity fluctuation u' depending on the turbulent kinetic energy k :

$$u' = \sqrt{2k/3} \quad (4.11)$$

In a turbulent flow field, a propagating flame front gets increasingly deformed with higher turbulent intensity u' . Damköhler [75] proposed that turbulent eddies which are significantly larger than the laminar flame thickness δ_l can distort the flame front while maintaining the local laminar flame structure, see [Figure 4.10](#) (left). This leads to a considerably larger turbulent flame surface A_T and hence a faster turbulent flame speed s_T .

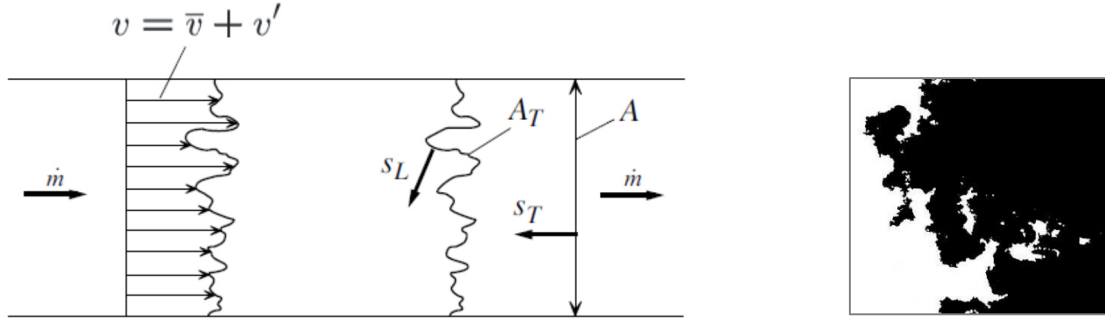


Figure 4.10: Wrinkling of a laminar flame front in a turbulent flow field: Schematic description of the turbulent flame speed s_T (left) [54]; Optical measurement of a turbulent flame front in an SI engine (right) [76]

The interaction between turbulence and chemistry is strongly dependent on the respective time and length scale ratios. This yields different turbulent combustion regimes that can be plotted descriptively in the Borghi diagram, see [Figure 4.11](#). As turbulence increases and turbulent intensity gets of the order of the laminar flame speed ($u'/s_L = 1$), eddies can wrinkle the flame more easily what leads to so called “corrugated flamelets”. If turbulence is raised further, smallest turbulent structures fall below the scale of the laminar flame thickness δ_l and are able to enter the flame zone. In this way small flame pockets are separated from the flame front that can possibly lead to partial flame extinctions, see [Figure 4.10](#) (right). Additionally, high-intensity turbulent structures are stretching the flame front, which is why this regime is called “thin reaction zone”. Both effects can deteriorate the stability of the propagating flame what especially gets critical at higher residual gas fractions.

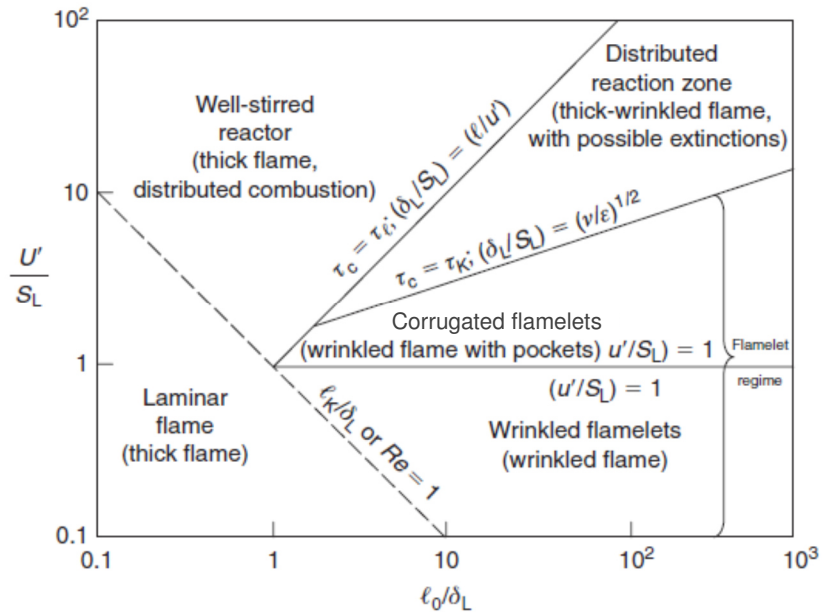


Figure 4.11: Turbulent combustion regimes in the Borghi diagram [77], reprinted from Abdel-Gayed et al. [78]

4.5. Detonation and Intensity of Super-Knock

After the occurrence of pre-ignition with subsequent flame propagation, a second much more violent gas-phase autoignition arises in a hot-spot in the compressed end gas. The rapid change in volume at the hot-spot reaction front leads to a generation of intense pressure waves. Bradley et al. [79] point out that the resulting dimensionless overpressure $p(t)_{max}/p$ is of order unity at the initiation of super-knock for the investigated PRF95. This is in accordance with experimental observations where the super-knock pressure amplitude is of the same order as the mean pressure.

Additionally, after the occurrence of shock waves, the front of the pressure wave generated by the heat release can couple with the autoignition reaction front. In this way chemical energy can be fed into the developing strong pressure wave leading to a pressure spike propagating at high velocity in a *developing detonation*, as described by Zeldovich [80]. The coupling between the acoustic wave and the propagation of the reactive front is defined by the resonance parameter ξ as:

$$\xi = \frac{a}{u_a} \quad (4.12)$$

With a , the speed of sound and u_a , the propagation velocity of the autoignition reaction front relative to the unburned gas. Direct numerical simulations carried out by Gu et al. [81] reveal that a developing detonation is not stringently restricted to ideal coupling of the two waves, with $\xi = 1$. Due to species and thermal diffusion there are lower and upper boundaries, ξ_l and ξ_u , between which a developing detonation can occur. Additionally, Bradley et al [79] note that the initial value of ξ alone is an insufficient indicator for the mode of autoignition. In fact, the reactivity of the charge influenced during interaction with the shock wave has a major impact. The authors introduce a reactivity coefficient ε as a measure for the energy input into the pressure pulse:

$$\varepsilon = \frac{r_0/a}{\tau_e} \quad (4.13)$$

Where r_0 is the initial radius of the reactive spot. τ_e is the excitation time, defined by Lutz et al. [82], between the instant of 5 % heat release rate to the maximum heat release rate. ε stands for the number of excitation times passing into the pressure pulse during its residence time in the reactive spot and hence describes the reactivity of the autoignitive spot. Plotting ξ_l and ξ_u against ε yields the regimes for the autoignitive modes, see black lines in [Figure 4.12](#). From this it can be seen that a higher reactivity, in terms of higher values of ε , clearly extends the regime over which detonation can occur. Regime B in the diagram is the region $\xi > \xi_u$, which corresponds to subsonic deflagration, the classical flame propagation mode. For $0 < \xi < \xi_l$ in region P a supersonic reaction wave propagation takes place without coupling with the pressure wave. Finally, for $\xi = 0$ homogeneous autoignition sets in simultaneously in the charge.

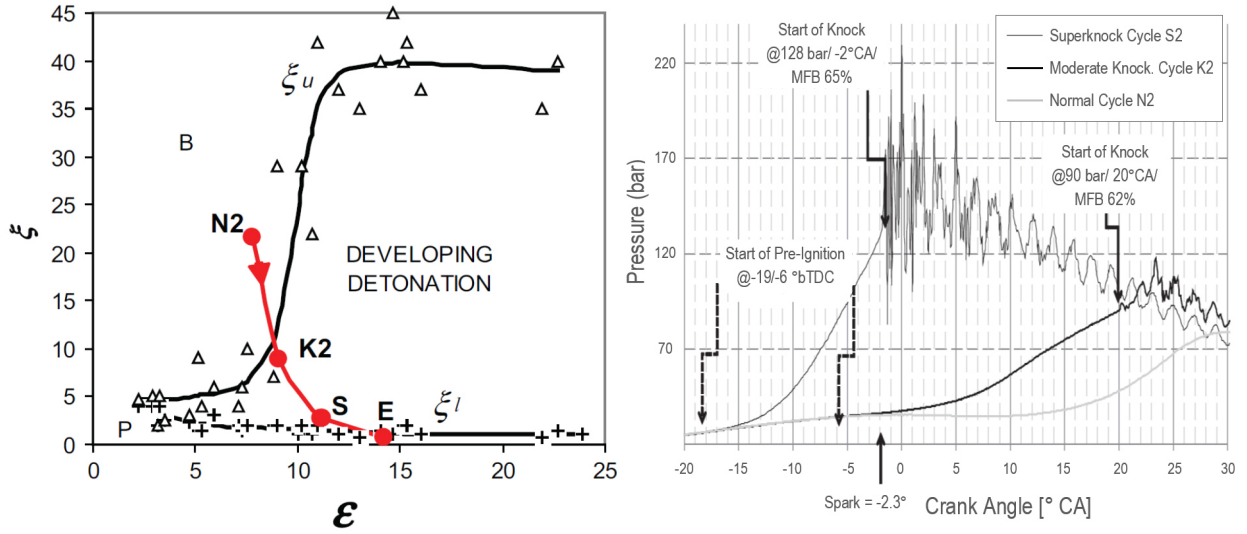


Figure 4.12: Conditions for the occurrence of a developing detonation in terms of the resonance parameter ξ and the reactivity parameter ε extended with values for a normal cycle (N2), a moderate knocking pre-igniting cycle (K2) and a super-knocking pre-igniting cycle (S) from Kalghatgi and Bradley [49]

Kalghatgi and Bradley [49] use the approach to evaluate knock severity. [Figure 4.12](#) represents well the transition from a regular cycle N2 to a fairly knocking cycle K2 and a super-knocking cycle S2 along a trace approaching high values of ε and low values of ξ . Moreover, Rudloff et al. [83] observe that pre-ignition events with values of ε and ξ inside the detonation regime do not stringently lead to severe knocking. The authors deduce that if the chemical energy left in the end gas is not sufficient, a violent detonation cannot form. Hence, the burned mass fraction at autoignition timing has to be considered beside the thermodynamic conditions favourable for coupling of the acoustic pressure wave with the reactive front.

Kalghatgi and Bradley [49] claim that the direct propagation of a detonation outside an autoigniting spot is unlikely. However, superposition of several developing detonations within a multitude of end gas hot spots dispersed randomly is supposed to aggravate this effect, as shown numerically by Pan and Sheppard [84] and experimentally by Rudloff et al. [83].

5. Experimental Evaluation of Pre-Ignition Characteristics

5.1. Description of the Test Bench Setup

The following investigations were performed on a turbocharged 4-cylinder gasoline engine with direct injection provided by GM Europe. This was a prototype engine featuring moderate modifications compared to series production enabling the analysis of higher downsizing levels. The test bench setup and the investigated operating conditions are given in [Table 5.1](#).

Table 5.1: Engine description and experimental setup for the PI investigations

Property	Specification
Type:	Inline 4
Displacement:	1,364 cm ³
Bore:	72.5 mm
Stroke:	82.6 mm
Compression ratio:	10.7:1
Air charging:	Turbocharger, charge air cooler
Direct Injection:	Central position, 6-hole injector
Speed:	2,000 rpm
p_{mi} /Torque:	21.3 bar/230Nm
Manifold pressure:	1.9 bar
Injection pressure:	160 bar
Ignition Timing:	3.5 °CAaTDC
Lambda:	1
Fuel:	RON 95

The crank angle based pressures of all four cylinders were measured with water-cooled piezo electrical pressure transducers. Low-pressure indication was installed at the intake and exhaust manifold of cylinder 1. Beside all relevant pressures and temperatures, the concentration of the most important exhaust gas components (HC, CO, CO₂, O₂ and NO/NO_x) were observed. Furthermore, the exhaust gas opacity was monitored with an AVL smoke meter and evaluated by the filter smoke number (FSN).

The feedback of breather gas to the intake was decoupled to prevent an impact of remaining oil mist on pre-ignition. In this way possible external influencing factors were excluded and the problem of pre-ignition initiation could be reduced to in-cylinder mechanisms only.

5.2. Pre-Ignition Statistics and Analysis of Cyclic Variations

For the high-load operating point, defined in Table 5.1, pre-ignitions occurred approximately all 10,000–30,000 cycles. During the entire measurement campaign, a total number of about 800 pre-ignition events was captured via high-pressure indication and subsequently statistically evaluated. Figure 5.1 gives an impression of the relationship between pre-ignition timing and the resulting maximum cylinder pressure that was derived from the low-pass filtered cylinder pressure signal. For this purpose, the pre-ignition timing was defined by the crank angle where 0.5 % mass fraction was burned (MFB0.5%). The earlier a pre-ignition was initiated, the more drastic was the increase of cylinder pressure and the resulting mechanical stresses. The earliest pre-ignition was detected at -17°CAaTDC . However, the histogram at the top of Figure 5.1 makes clear that autoignitions primarily occurred close to TDC. This reveals that high pressures and temperatures prevailing at TDC are most decisive for the acceleration of pre-reactions leading to an uncontrollable autoignition.

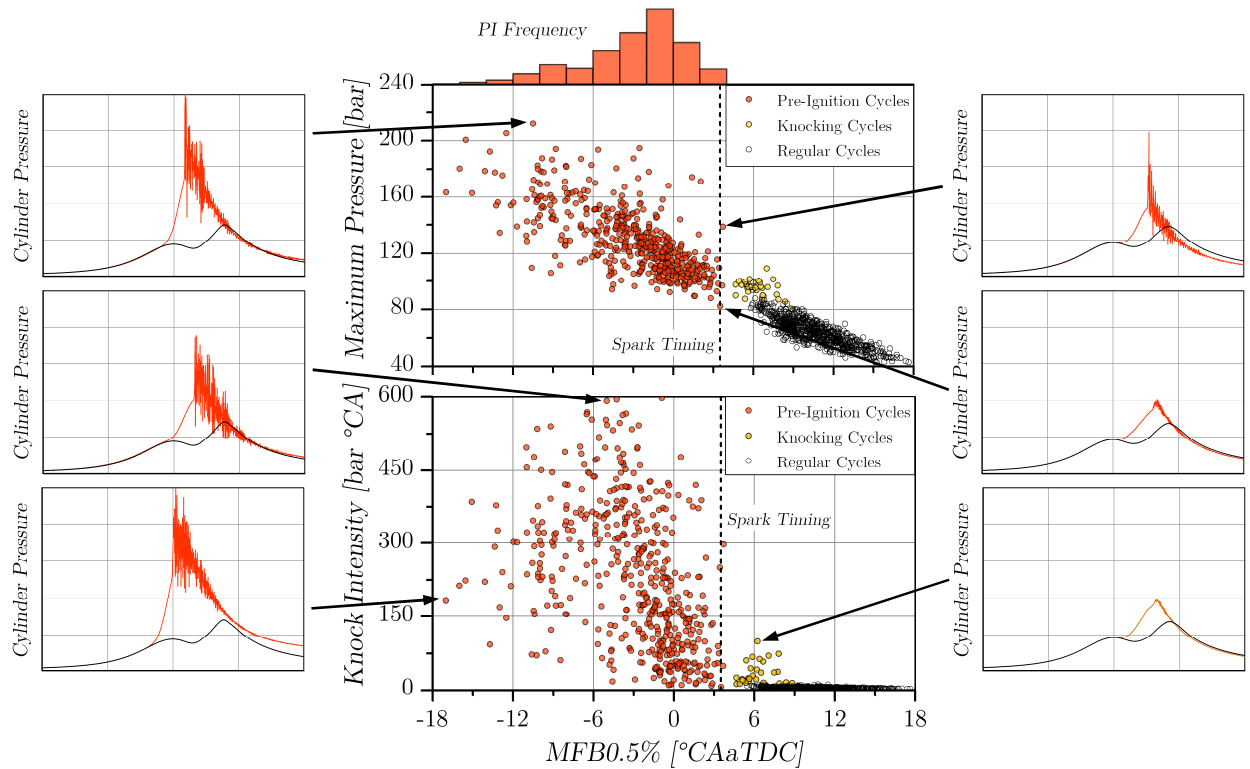


Figure 5.1: Effect of pre-ignition timing (characterised by MFB0.5%) on maximum cylinder pressure (top diagram) and knock intensity (bottom diagram)

In contrast to the strong linear dependency of maximum pressure on MFB0.5%, the knock intensity exhibits highly scattered values without any clear correlation. The most severe knock intensities were determined for autoignitions around -5°CAaTDC , whereas the highest cylinder pressures were found for PIs around -10°CAaTDC . Interestingly, for several cycles with early PI-timings also

exceptionally low knock intensities were determined. The strong variance of knock intensities indicates that this kind of autoignition might be dominated by stochastic processes like cyclic variability of charge composition or temperature fluctuations.

To find out if particular conditions, that could initiate PIs, are different solely for the pre-ignition cycles, a multi-cycle three-pressure-analysis (TPA) was carried out for 100 consecutive measured cycles including at least one cycle with premature ignition. For the TPA, measured pressure profiles of intake, exhaust and cylinder were applied as model boundaries. In this way, cyclic fluctuations of the cylinder charge properties were reproduced considering the gas dynamic effects during gas exchange. [Figure 5.2](#) gives a basic overview of the applied model and the input parameters.

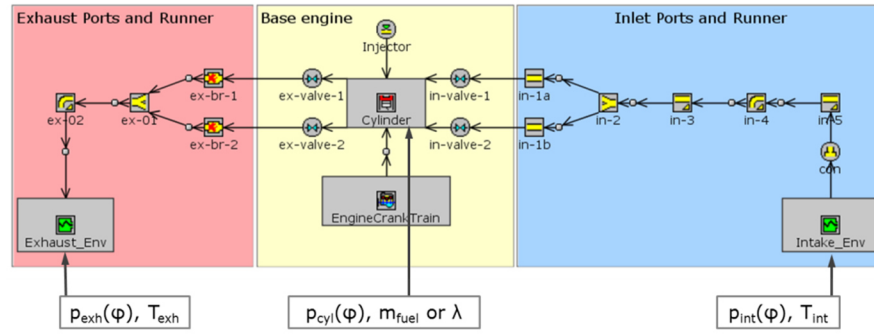


Figure 5.2: Three-pressure-analysis (TPA) with main input parameters modelled within GT-Power

The simulation results showed that fluctuations of obvious PI critical properties like the cylinder pressure and temperature at intake-valve-closing (IVC) lay within a very narrow range without any noticeable outliers that would have indicated an irregularity, see [Figure 5.3](#) (left).

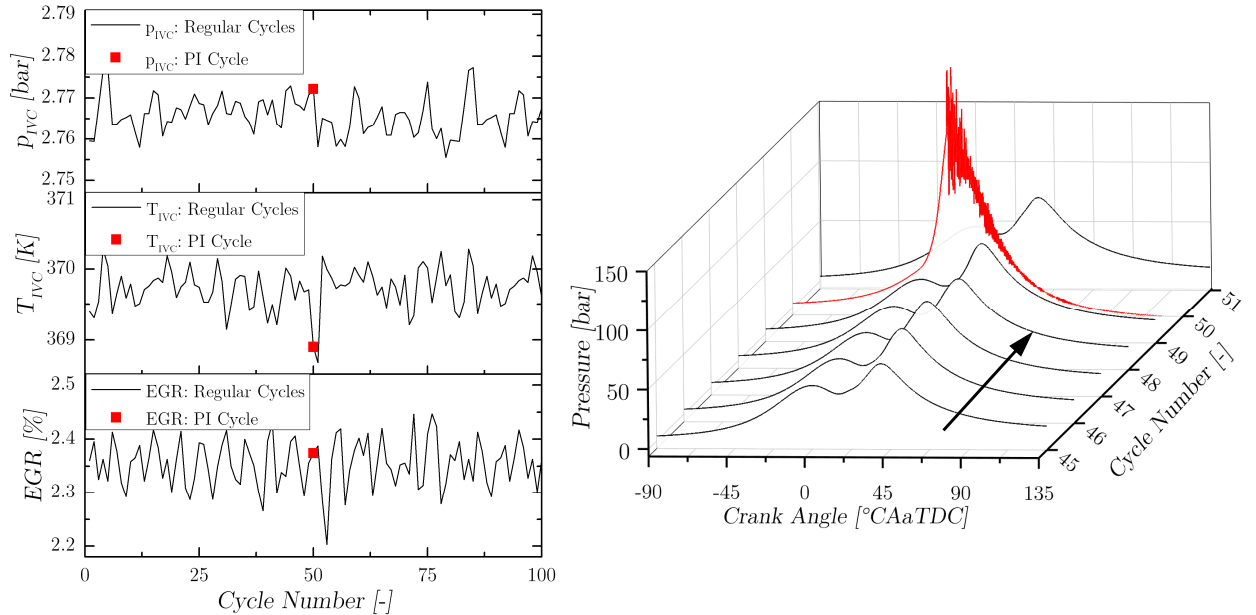


Figure 5.3: Fluctuations of the global thermodynamic charge properties and the remaining residual gas fraction at IVC during a pre-ignition run (left); Cylinder pressure traces for the pre-ignition occurring at cycle 50 and several cycles preceding the event (right)

Hot residual gas including reactive species that remains in the combustion chamber after the exhaust stroke is often associated with irregular combustion. As shown in the left bottom diagram in Figure 5.3, the effective gas exchange under full-load conditions due to the positive scavenging gradient led to a relatively low mean residual gas content of about 2.4 % with almost negligible variations. Therefore, an elevated residual gas fraction can definitely be excluded as reason for pre-ignition.

From the right diagram in Figure 5.3 it can be concluded that beside the global cylinder properties also the combustion characteristics of cycles preceding a pre-ignition event do not exhibit any particular irregularity. The absence of a self-amplifying autoignition sequence is a strong indication that surface ignition due to overheated engine components like the spark plug or exhaust valves is quite unlikely for this engine. Rather, the stochastic nature of the phenomenon makes clear that the mechanism has to be determined by local and instantaneous inhomogeneities. In order to understand the spatial and temporal processes leading to pre-ignition, optical diagnostics was applied at the engine test-bench.

5.3. Observations with a High-Speed Endoscopic Access

A video access was installed on cylinder 4. Two bores were applied to the cylinder head, passing through the water jacket. High-speed imaging was carried out from one direction and light was introduced from the other. The positions of the mounted sleeves are shown in [Figure 5.4](#). In order to guarantee an optimum field of view without light reflections, a certain angle had to be maintained between the axes of the light source and the camera.

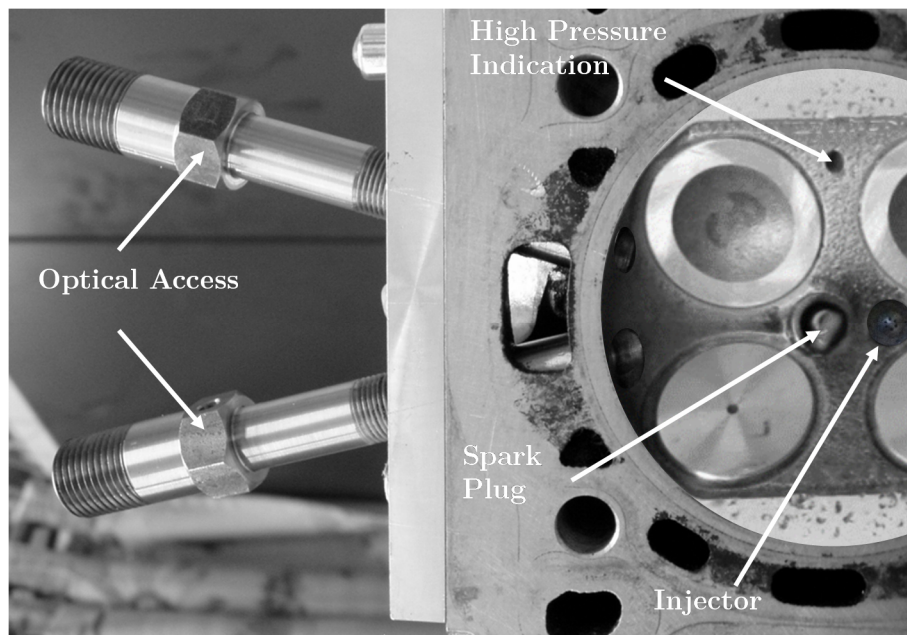


Figure 5.4: Endoscopic access for optical diagnostics

The optical recording unit consisted of an endoscope, an image intensifier (Hamamatsu) and a high speed camera (IDT MotionXtra N4) that allowed frame rates up to 130,000 fps; see [Figure 5.5](#) for the assembled equipment.

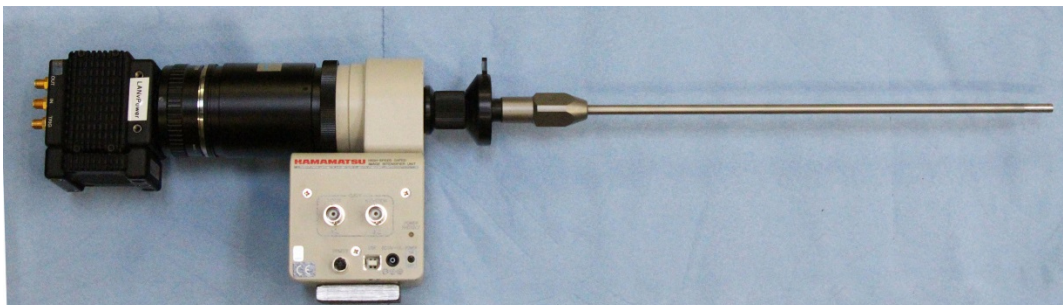


Figure 5.5: Optical equipment consisting of high-speed camera, wide-angle lens, image intensifier and endoscope

Generally, pre-ignitions often occurred within clusters of up to five events alternating with regular combustion cycles but single events were detected most frequently. While using the optical diagnostics, operation was usually switched off after a single event for the critical cylinder in order to prevent damages of the optical windows and also of engine components. However, several pre-ignition sequences were recorded in order to study the phenomenon.

The first observed pre-ignition of a cluster showed distinct different light emissions than all following events: During the first pre-ignition cycle, a light source occurred spontaneously and immediately ignited the entire mixture. Due to the fact that there was no previous light emission, it is likely that the first pre-ignition was triggered by an oil-fuel droplet that reached its critical condition for autoignition at the moment when it became visible. [Figure 5.6](#) (a) shows three different initial pre-ignition events at the moment the spontaneous light emission became visible.

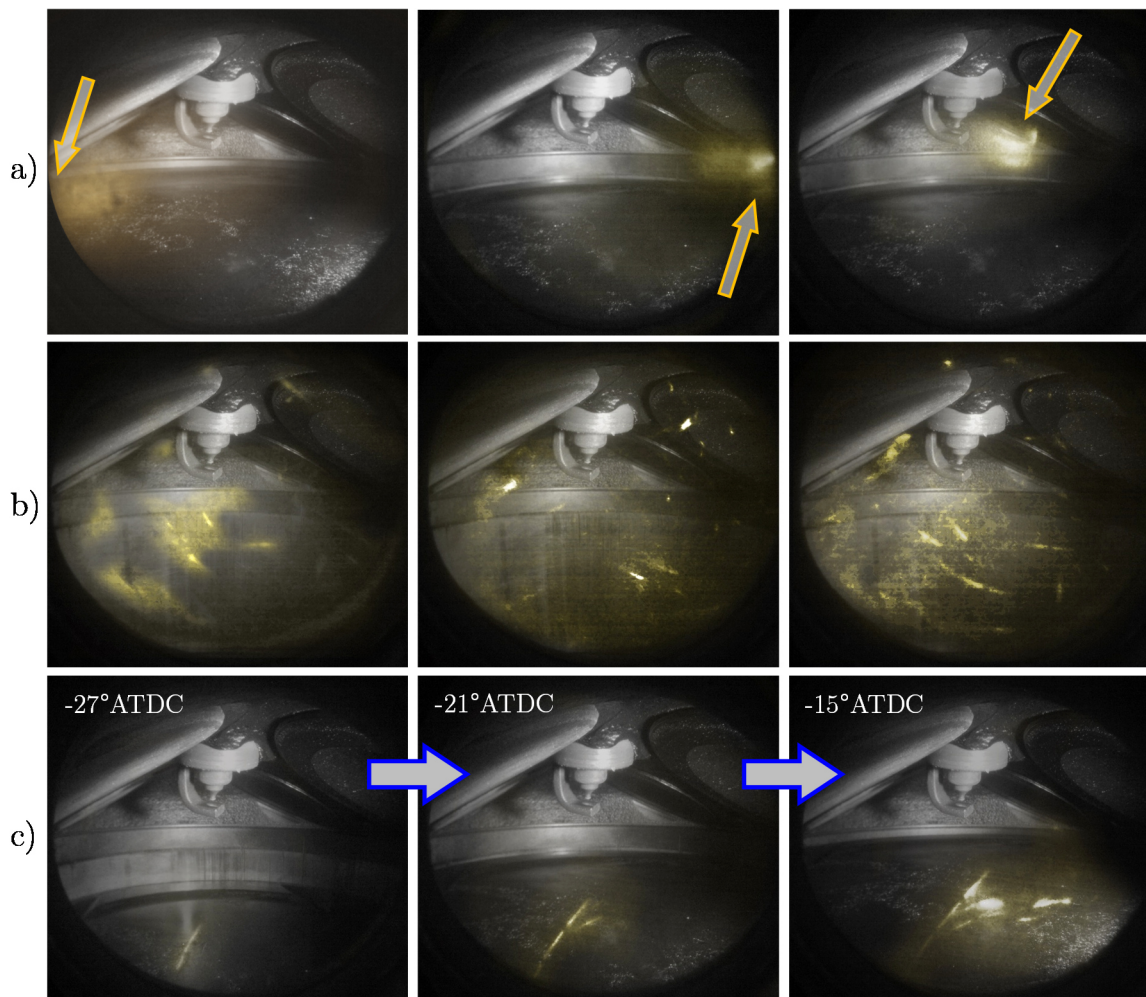


Figure 5.6: High-speed images of pre-ignition events: (a) three different initial pre-ignition events; (b) three different subsequent cycles with glowing particles; (c) Progress of one follow-up pre-ignition event initiated by a glowing particle

As already reported in other studies, it was confirmed that the locations of pre-ignitions vary inside the combustion chamber. The majority of the pre-ignition spots were detected at the height of the cylinder head gasket and in the vicinity of the liner, but also in the centre of the gas volume. Therefore, no connection to possible hot-spots like the spark plug or the outlet valves was given. Furthermore, all pre-ignitions started from a single position leading over to rapid flame propagation accompanied by bright light emissions covering the entire charge volume.

The application of optical diagnostics made it possible to clarify the mechanism leading to follow-up pre-ignition sequences: It was common to all pre-ignitions that in the following regular burning cycle, glowing objects were observed, particularly during the final combustion phase, see Figure 5.6 (b). Obviously, these were glowing fragments of deposits. They were detached by the high-amplitude, high-frequency pressure fluctuations of the mega-knock event of the pre-ignition cycle, close to the end of the combustion. Apparently, some of these particles remained in the combustion chamber and were heated up during the following regular combustion, where the time was sufficient for the heat transfer between gas and particle. It is therefore likely that particles that exceed a critical size and remain above a critical temperature cause the pre-ignition in the following cycle. Then, deposits are detached again, are heated up in the following regular cycle and provoke a pre-ignition in the next cycle. Figure 5.6 (c) shows the evolution of such a subsequent pre-ignition originating from a glowing particle. Follow-up pre-ignitions usually repeated three to five times, obviously until no major deposits were present in the combustion chamber. Hence, video observation of the combustion process provided an explanation for the alternating occurrence of pre-ignitions and regular cycles. Follow-up events seem to be triggered by a different mechanism than initial events. This work will especially focus on the modelling of initial events and therefore the fundamental basis for pre-ignition. However, the presented method was also adapted to analyse follow-up events what will be outlined in Section 8.7.1.

6. Determination of Charge Inhomogeneities with CFD

For boosted engines under full-load conditions a sufficient mixture preparation becomes increasingly challenging. High charge densities demand for large fuel masses that must be evaporated and mixed with air within a very short time available. Gradients of fuel vapour and especially of temperature were shown in experiments to be strongly influential on autoignition [85]. To take detailed account for this influence, a 3D-CFD simulation was carried out in *Star-CD v4.18* to deliver the spatial distribution of charge properties in the cylinder. Temperature inhomogeneities in the combustion chamber can have several sources like hot wall temperatures, especially close to the exhaust valves or spark plug electrodes, but can also be caused by an insufficient mixture preparation due to low charge motion or incomplete fuel spray evaporation. The consideration of all these effects was possible via introducing sub-models and other model adaptations in CFD.

6.1. Description of the CFD Model

The meshing was performed in *es-ice v4.14* via mapping the manually adapted cell topology on the cylinder geometry. The computational grid consisted of approx. 1 million hexahedral cells at BDC with an average cell size of about 1 mm. In [Figure 6.1](#) (left) a sectional view through the valve plane illustrates the cell spacing during intake-valve-opening. The spark plug was expected to have a certain impact on the charge temperature and turbulence. Therefore, the detailed geometry of the spark plug electrodes was considered as can be seen in the right view in [Figure 6.1](#).

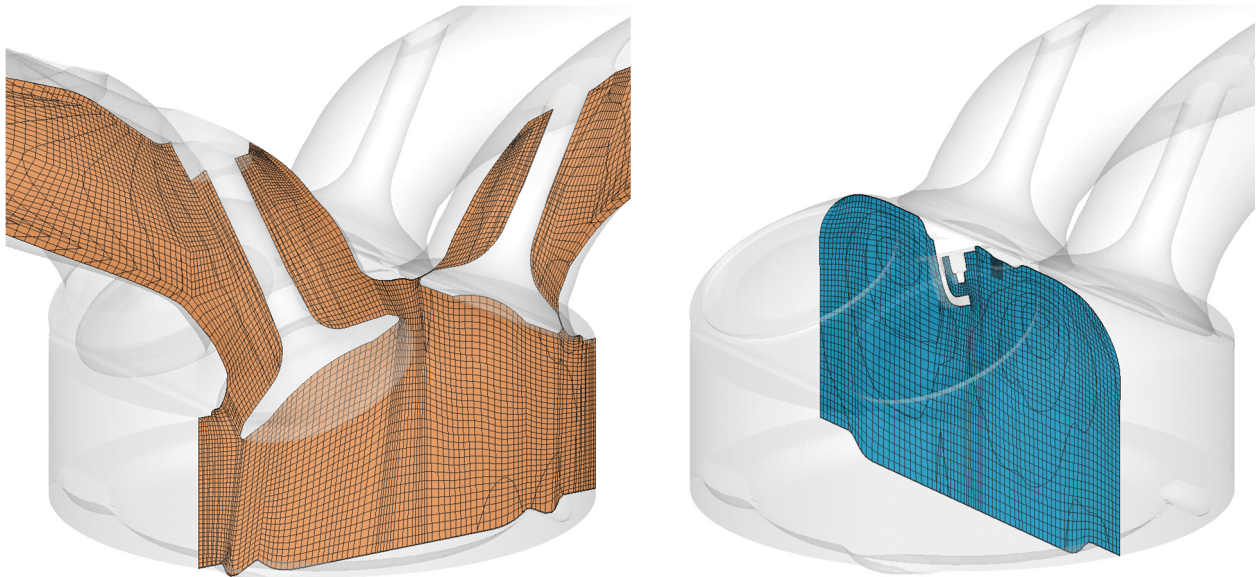


Figure 6.1: Hexahedral moving mesh shown at 410 °CAaTDC in two sectional views

A mesh region close to the injector tip was refined to better resolve for injected droplets with high initial velocity. Along the cylinder walls a 0.1 mm prism layer was created to capture the turbulent and thermal boundary layer. The surface temperatures were pre-calculated with a wall temperature solver in the 1D cycle simulation that uses a simplified finite-element model. The inlet was defined as mass flow boundary, the outlet as pressure boundary.

The highly turbulent flow field was captured with the ‘Renormalisation Group’ version of the two-equation $k-\varepsilon$ model (RNG $k-\varepsilon$). A distinctive feature of this model is an additional dissipation term accounting for the effect of mean flow distortion on turbulence. This improves the accuracy especially for the swirl and tumble motions predominating the in-cylinder flow field.

6.2. Fuel Injection and Spray Validation

The injected droplets were treated as dispersed phase within a Lagrangian framework, whereas the turbulent continuous phase (intake air) was simulated with an Euler approach. Primary break-up was not considered as the accuracy of available models is not satisfactory yet. The injection of fuel was modelled based on a statistical method referred to as discrete droplet model (DDM) [52]. For computational reasons, samples of identical physical droplets are grouped in parcels. About 100,000 parcels were injected throughout an injection sequence, i.e. 50 parcels per time step (0.025 °CA during injection). The spray initial velocity of 143 m/s at the nozzle exit was determined from high-speed measurements in a spray bomb. The simulated spray tip penetration was in good accordance with the experiments; see [Figure 6.2](#) and [Figure 6.3](#), left.

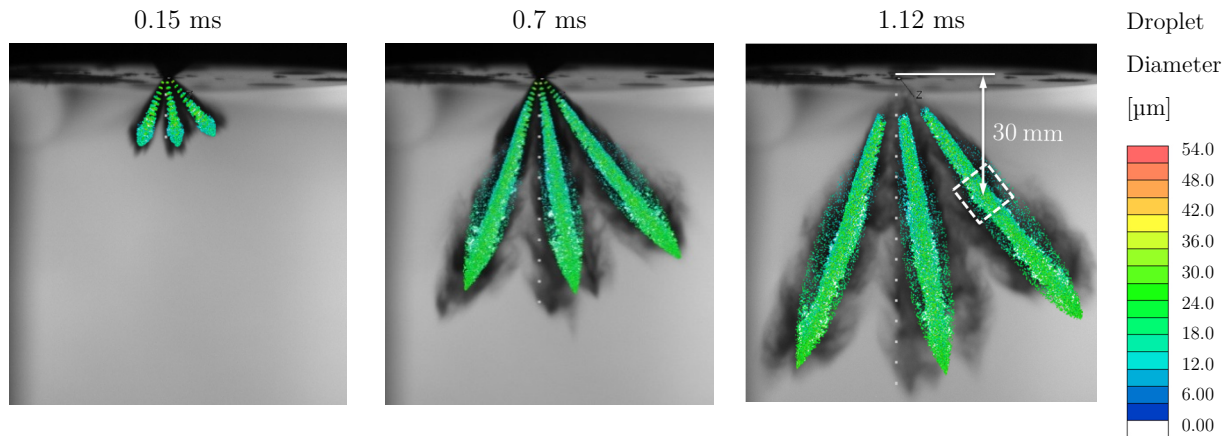


Figure 6.2: Validation of the spray tip penetration with high speed images in a spray bomb. The control volume for SMD evaluation is marked in the right picture.

All spray properties and boundary conditions were defined in a user-coded subroutine. From this, the initial diameter D_0 for each parcel was chosen randomly within a specified range ($15 \mu\text{m} \leq D_0 \leq 65 \mu\text{m}$). The respective particle mass fractions were then assigned to maintain the measured overall spray size distribution, which was defined using a Rosin Rammler distribution function:

$$\psi(D) = 1 - \exp \left[- \left(\frac{D}{X} \right)^q \right] \quad (6.1)$$

Secondary break-up was considered according to Reitz and Diwakar [86]. In this way, droplets that exceeded the critical Weber numbers ($We_{crit,bag} = 6$ for bag break-up and $We_{crit,strip} = 0.5$ for stripping break-up) broke down to smaller stable diameters.

The initial spray size distribution ($X = 47$, $q = 8$, $SMD_{0\text{ mm}} = 38.5$) was defined iteratively in order to find a correlation with PDA measurements at 30 mm distance from the nozzle exit, as illustrated in the right image of Figure 6.2. The result can be seen in the right diagram of Figure 6.3. The evolution of SMD over time was in good agreement with the experiment and therefore justified the definition of the initial drop size distribution. Obviously, the smallest droplets $< 15\text{ }\mu\text{m}$ were slightly underestimated through secondary break-up, as can be seen towards the end of the observed period. However, during the main plateau phase, where most of the droplets were statistically considered, the SMD was predicted accurately. Therefore, the spray setup was regarded as appropriate for the following in-cylinder simulations.

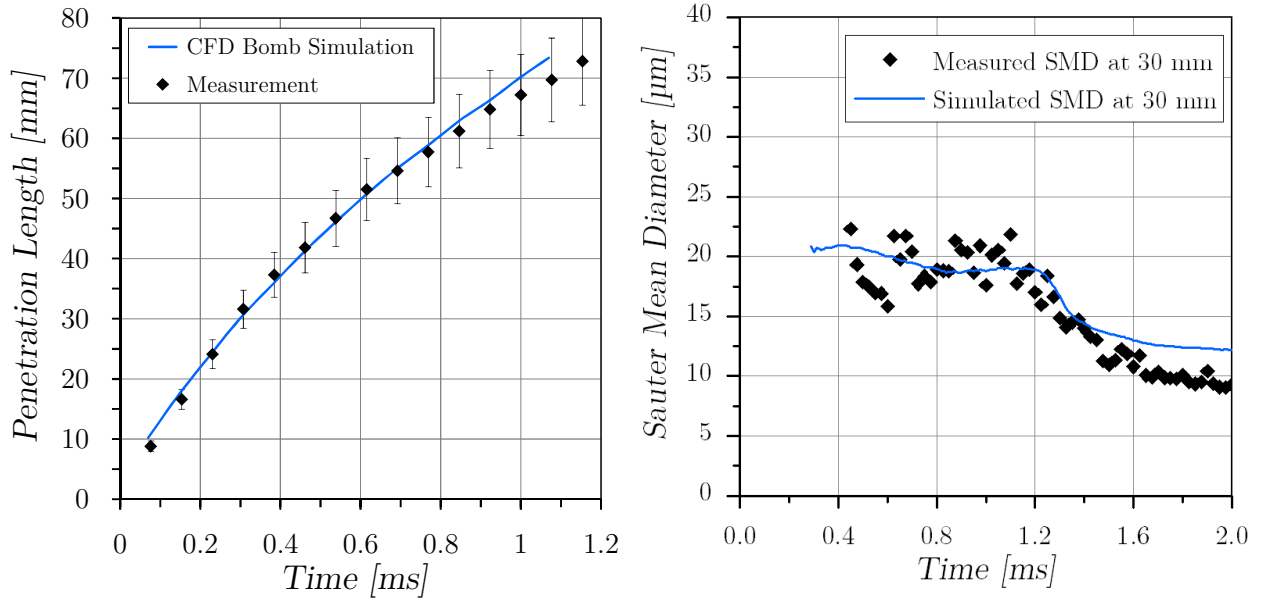


Figure 6.3: Validation of the spray tip penetration and the evolution of SMD over time at 30 mm distance

6.3. Implementation of a Multi-Component Fuel

In order to define a multi-component surrogate fuel that on the one hand can be easily implemented in a CFD-simulation and on the other hand fits the evaporation characteristics of the real fuel, a simplified calculation approach was developed to simulate the measurement of the distillation curve according to DIN EN ISO-3405. During this procedure 100 ml of fuel are electrically heated in a spherical distillation flask of a volume of 125 ml. The temperature increase is 1 K/min. The vapour is afterwards condensed in a cooling pipe and collected in a measuring cylinder. For the simulation of the surrogate fuel's distillation curve, the liquid in the distillation flask was assumed perfectly mixed, without any temperature and concentration gradients. Following the work of Batteh and Curtis [87] the components isopentane, n-hexane, isooctane, 123TM-benzene and n-tridecane were used to create a surrogate fuel with similar vaporisation characteristics as the tested fuel. [Figure 6.4](#) shows the mass fractions and boiling temperatures of these five components.

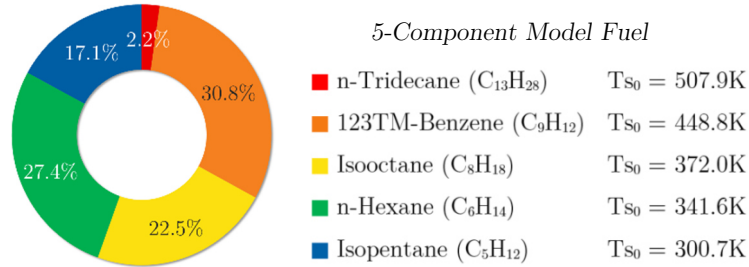


Figure 6.4: Composition of the gasoline surrogate fuel

Ideal liquid and ideal vapour was assumed in order to choose the same physics as it is implemented in the CFD-code. The mass flow \dot{m}_i of the different species from the liquid to the vapour phase was calculated referring to [87,88], see Eq. (6.2)

$$\dot{m}_i = Sh \left(\frac{p_i M_i}{\sum_j p_j M_j} \cdot \frac{A}{D_{fl}/2} \cdot \rho_a \cdot \mathfrak{D}_i \cdot \ln \frac{p_a}{p_a - p_v} \right) \quad (6.2)$$

where p_i denotes the partial pressure of species i , M_i the molecular weight and \mathfrak{D}_i the diffusion coefficient in air. p_a is the ambient pressure and has the value 1 bar. ρ_a is the ambient density and A the free surface of the liquid. The concentration gradient above the liquid was assumed to be linear and is expressed with the radius of the distillation flask $D_{fl}/2$. For the Sherwood number Sh the Ranz-Marshall-Correlation gives:

$$Sh = 2.0 + 0.6 Re^{1/2} Sc^{1/3} \quad (6.3)$$

with the Reynolds number Re and the Schmidt number Sc . Finally, a value of 3.0 was chosen for this simple approach to fit the measured data. [Figure 6.5](#) (left) shows the verification of the presented approach. The calculated distillation curve of the surrogate fuel using the mass fractions from Figure 6.4 was compared to the measured distillation curve of the RON95 fuel. A reasonable

correlation between the calculation results and the measurements can be observed. Therefore, the composition of the model fuel was considered as suitable for the CFD-application.

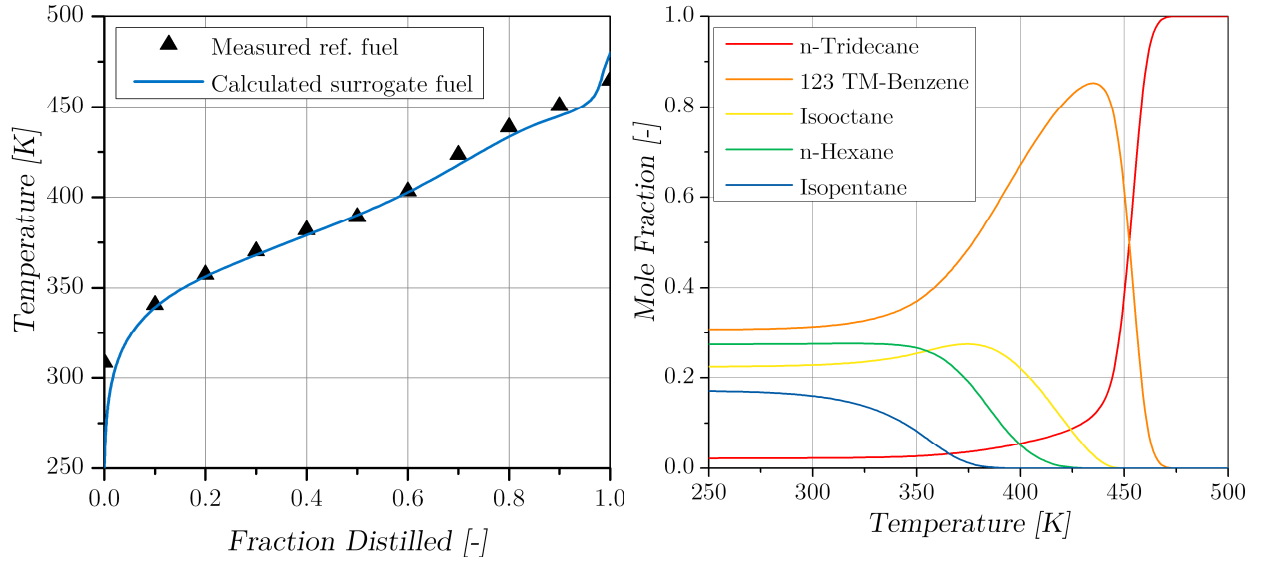


Figure 6.5: Comparison of calculated and measured distillation curves (left).
Mole fractions of the 5 components developing during the distillation process (right).

The demixing process of the components due to their different volatilities gets visible in [Figure 6.5](#). The fractions of constituents with lower boiling temperatures are decreased rapidly. Less-volatile components get concentrated during the distillation process. Hence, it can be expected that the representation of the dynamic multi-component fuel evaporation behaviour will yield more accurate results in terms of mixture cooling and liquid film formation in contrast to simple fuel approximations like n-heptane.

6.4. Validation of the Liquid Film Formation

An efficient mixture preparation for direct injection engines is a challenging task because of a much shorter available time range for fuel evaporation and homogenisation. This effectively gets compensated by high injection pressures enabling finer and hence more rapidly evaporating droplets. The resulting higher spray velocities are problematical because of an increased tendency for deposition as liquid film on the combustion chamber walls. Besides higher HC and soot emissions, also the PI tendency was found to be influenced by wall wetting. Therefore, the validation of the modelled impingement process is a main focus for the following modelling issues.

In *Star-CD*, the Bai-model [89] is implemented as a multi-regime impingement model. The highly dynamic physical processes during droplet wall interaction are categorized by the characteristic quantities: wall temperature T_w and dimensionless droplet Weber number We , see [Figure 6.6](#).

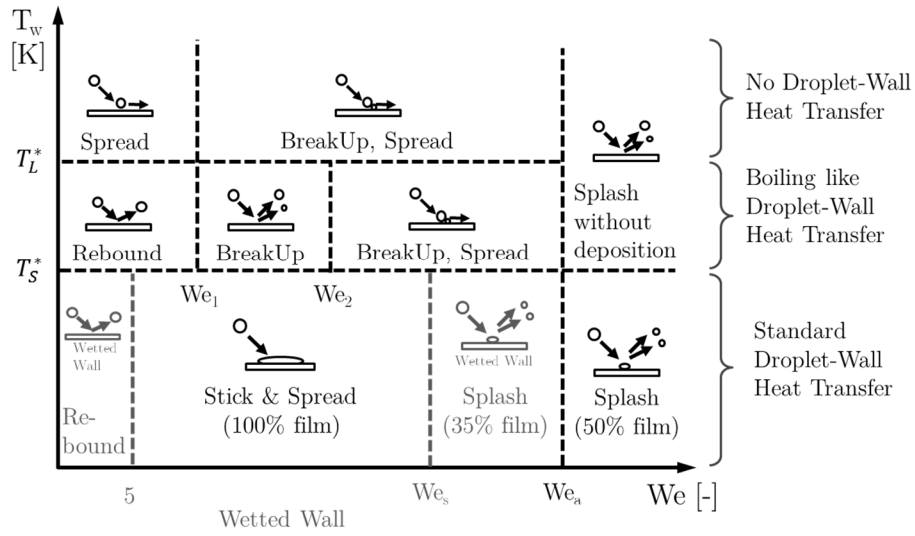


Figure 6.6: Droplet impingement regimes and transition conditions for dry and wetted walls [89,90]

The droplet stability can be described by the dimensionless droplet Weber number We , which is dominated by the droplet normal-to-wall impact velocity v_n :

$$We = \frac{\rho \cdot v_n^2 \cdot D}{\sigma} \quad (6.4)$$

Different impingement regimes (Rebound, Stick, Spread, Splash and Break-Up) can be distinguished by empirically derived critical Weber numbers (We_s , We_a , We_1 , We_2) which mainly depend on the prevailing surface properties (roughness, wet or dry wall).

For wall temperatures below the rebound temperature T_S^* an impinging droplet creates wall film. This temperature is linked to the droplet boiling temperature T_{sat} by an empirical factor B_S^* :

$$T_S^* = B_S^* \cdot T_{sat} \quad (6.5)$$

In Star-CD, the thermal liquid-solid contact beyond the boiling temperature is modelled by the Nukiyama pool boiling correlation, see [90] and [91] for details. For higher wall temperatures above T_S^* no wall contact is assumed because of an intervening vapour cushion forming instantaneously when the droplet hits the wall. Therefore, no deposition of fuel is possible at wall temperatures beyond T_S^* . Thermal contact is only taken into account for the spread regime, where droplets are moving along the surface. For wall temperatures exceeding the sliding temperature T_L^* no direct heat transfer from the wall is assumed, even for droplets sliding along the surface. T_L^* refers to the Leidenfrost temperature T_L by an empirical factor B_L^* :

$$T_L^* = B_L^* \cdot T_L \quad (6.6)$$

In different experiments [92,93] it was stated that droplets even beyond the Leidenfrost temperature can lead to a cooling of the surface. Hence, the Bai model assumption of a perfectly isolating vapour film and zero thermal contact above T_L^* seem to be inappropriate. Thermal contact above the sliding temperature T_S^* is implemented in the Bai model only for the break-up and spread regime until T_L^* . This regime can be regarded as a more realistic physical representation of the Leidenfrost phenomenon. Therefore, as proposed by Fischer [94], the zero heat flux regimes beyond T_L^* have been effectively deactivated by setting this value to a relatively high temperature ($T_L^* = 1000 \text{ K}$). Consequently, the rebound temperature T_S^* , that represents the deposition limit, was set equal to the Leidenfrost temperature of gasoline.

Panão and Moreira [95] have analysed the surface heat flux for gasoline sprays interacting with heated surfaces. The experiments reveal that the Leidenfrost temperature in pulsed systems is especially dependent on pulse duration and injection frequency. In this consideration, fuel direct injection can be regarded as a special case: In contrast to constant laboratory conditions, the walls experience excessive intermittent heat up sequences during the combustion phases. In this way wall cooling due to impinging droplets may be compensated by the combustion process itself or may even be overcompensated because of deposited liquid fuel burning directly off the wall. Additionally, it can be assumed that the majority of fuel vapour emerging in the vicinity of wetted surfaces gets burned in every cycle. Hence, a saturation effect that could slow down film evaporation is widely avoided. Therefore, it was concluded that a superposition of subsequent injection pulses plays a minor role for the Leidenfrost temperature and data was chosen for the lowest pulse frequency available in [95] ($f_{inj} = 10 \text{ Hz}$). Furthermore, Fest-Santini [92] argues with experiments that the effect of pulse duration generally has a stronger influence on the Leidenfrost temperature. For the injection duration of the study at hand ($\Delta t_{inj} = 4.2 \text{ ms}$), a value of $T_S^* \approx 1.47 \cdot T_{sat} = 496.15 \text{ K}$ was finally determined as Leidenfrost temperature for the used gasoline fuel.

The available modelling framework of *Star-CD* v4.18 only allowed for setting constant wall temperatures. A consideration of transient wall heat-up or cooling effects due to film evaporation was therefore not given. To cope with this challenge a sound validation of the fuel deposition behaviour was necessary.

The combustion chamber surface temperatures were determined with an implemented temperature solver in *GT-Power*. A simplified finite-element model is used to calculate the mean wall temperatures for each engine component. The main model input parameters that have to be defined, are the heat transfer coefficients between coolant and components, between valves and valve seats

and a factor to the Woschni heat transfer coefficient between cylinder charge and structure. To determine these values, a design-of-experiment (DOE) analysis was carried out with the volumetric efficiency as target quantity. Details about the methodology and the results of this analysis are documented in [96] and [97].

The restriction to fixed wall temperatures for moving-mesh in-cylinder simulations suggests that the resulting film evaporation will be overestimated due to missing wall cooling effects. However, to be able to evaluate this cooling effect, the cylinder mesh was frozen at -90°CAaTDC enabling a simulation with conjugate heat transfer. Simultaneously the injection event was kept the same as for the moving mesh case, leading to a more concentrated impingement of fuel on the piston. Several cell layers of solid aluminium (total thickness 5 mm) were added to mimic the piston thermal behaviour. [Figure 6.7](#) shows the result of wall wetting (left) and the associated local temperature drop at the piston surface (right).

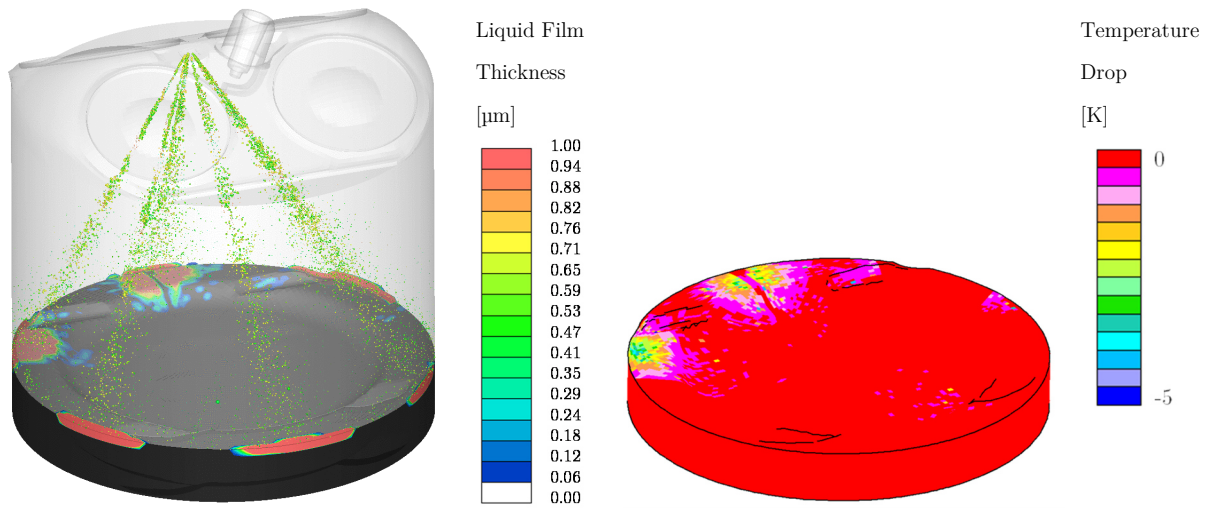


Figure 6.7: Liquid film formation and associated maximum cooling of the piston surface for a non-moving cylinder mesh fixed at -90°CAaTDC extended with solid aluminium piston cells

Even for areas with relatively thick films ($> 100\ \mu\text{m}$), a cooling of maximum 5 K was observed. Keeping in mind that this is a simplified approach, the restriction to constant wall temperatures can be accepted because resulting errors can be expected to lie within the magnitude of the numerical error tolerance. Further details have been published in [98].

After defining the deposition limit and wall temperatures, the droplet-wall interaction showed strong dependency on the used model fuel. The following [Figure 6.8](#) illustrates the different impingement behaviour of the multi-component fuel, presented in [Section 6.3](#), in contrast to that of pure n-heptane as a simple fuel surrogate.

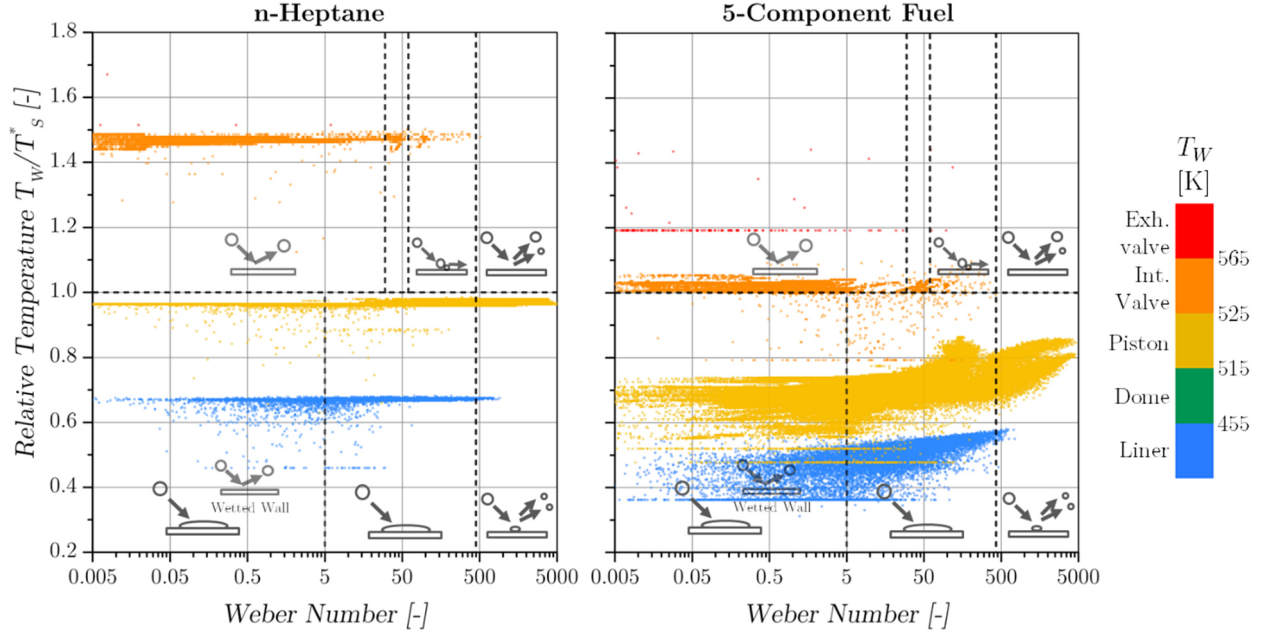


Figure 6.8: Droplet impingement events marked in the adapted Bai model regime map for injection of n-heptane (left) and multi-component fuel (right)

The property that decides about wall wetting is the droplet's Leidenfrost temperature T_S^* at the moment of contact with the surface. As already discussed, this value is related to the saturation temperature $T_{sat}(p)$ of the drop which is pressure dependent. To make all impingement events comparable that occur at different pressures, the ordinate was reduced to $T_W/T_S^* = T_W/(1.47 \cdot T_{sat}(p))$. In this context, deposition is possible for values of $T_W/T_S^* < 1$. Looking at the results for n-heptane (left diagram), it becomes obvious that due to missing demixing of the fuel, the impingement events occur almost on straight lines belonging to the respective component surface temperature (see legend for colour assignment). Scattering, especially to lower values is caused by the rising droplet saturation temperature during compression for late impingement events. In contrast, distinct demixing processes can be observed for the multi-component fuel. Due to an immediate evaporation of high-volatile hydrocarbons, the droplet boiling temperature and hence T_S^* are shifted to higher values. This, in turn, leads to an increased tendency for wall film as values for T_W/T_S^* are more likely to fall below 1. In the present case this becomes especially obvious for impingement on the intake valves (orange colour). For n-heptane impingement occurs far beyond the deposition limit, whereas for the multi-component case, numerous events fall below the limit, especially for higher Weber numbers.

A comparison of the cumulative probability functions depending on the Weber number is given in [Figure 6.9](#). Due to the fine initial spray size distribution ($SMD_{0\,mm} = 38.5$), for both model fuels about 8 % of all impingement events occurred for very small Weber numbers below $We = 0.5$. For bigger or rather faster droplets with values beyond $We_a \approx 500$, the impingement regime changes from stick/spread to partial rebound/splash with a lower tendency for deposition (see also [Figure 6.6](#)). The influence of evaporating high-volatile constituents, decreasing the drop diameter, is clearly noticeable: On total about 14 % more impingement events occur below $We_a \approx 500$ leading to an enhanced wall wetting for the multi-component case.

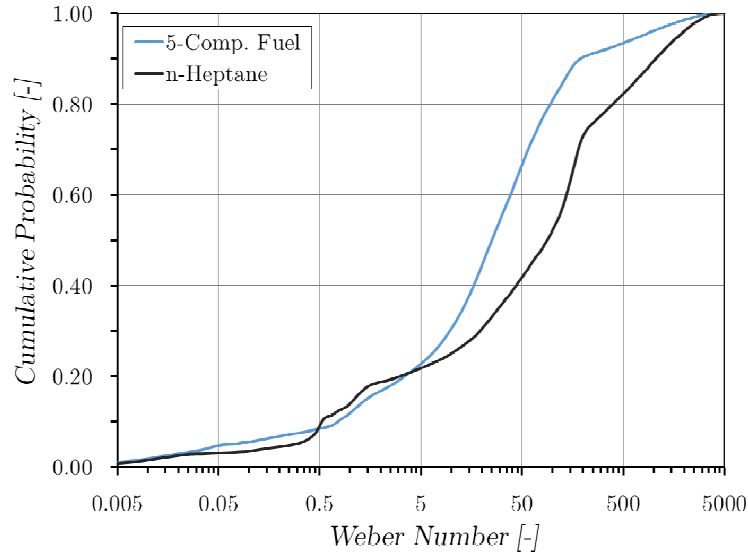


Figure 6.9: Cumulative probability functions plotted over Weber number for n-heptane and multi-component fuel injection

Especially for studying autoignition problems, a correct modelling of the wall film formation on hot surfaces is crucial. The impingement analysis showed that with multi-component fuels important information about liquid fuel deposition is acquired that wouldn't be available with conventional single-component fuel approaches.

After introducing enhanced fuel and impingement models, an experimental validation of the deposition characteristics was carried out. Currently, a direct measurement of the wall film mass inside the combustion chamber of a full engine may only be possible with substantial investments of time and costs while the result quality would still be unclear. Instead, particulate emissions that originate from diffusive combustion of fuel-rich regions like droplets or liquid films were used as an indicator for the wall wetting tendency. Particle formation was measured using an *AVL Smoke Meter*, a filter paper method to determine the soot concentration in the exhaust gas. The filter blackening is detected by a photoelectric measuring head and quantified as Filter Smoke Number FSN which correlates with the soot concentration ($1\,FSN \approx 10\,mg/m^3$).

For the simulations, the remaining wall film mass at TDC was chosen as reasonable quantity describing the soot tendency due to wall wetting of the current engine setup. With this approach, the transient evolution of wall film could be reduced to a single value with the aim to obtain a quantity that is comparable to the measured FSN. The image sequence in [Figure 6.10](#) illustrates a

distinct fuel deposition process on the piston crown and the liner with subsequent film evaporation until TDC. The start of injection (SOI) for this result was rather close to TDC (SOI = 380 °CAaTDC).

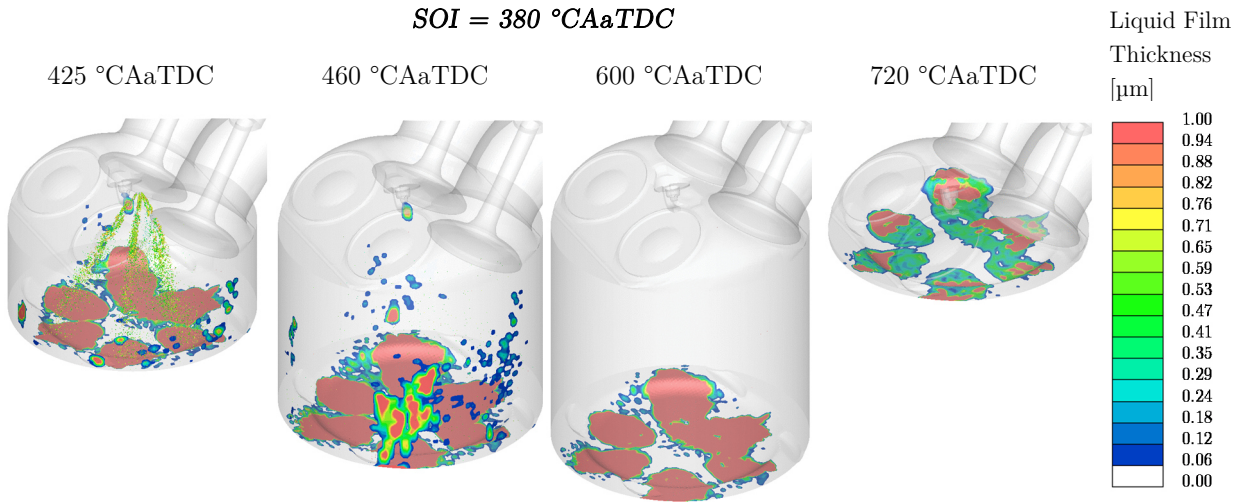


Figure 6.10: Simulation of wall film deposition with “high FSN” injection timing: SOI=380°CAaTDC

In [Figure 6.11](#) the quantitative evolution of the wall film is shown for the same SOI (black curve) in comparison to later injection timings. It becomes clear that with retarded injection, the wetting decreased drastically. As a result of the larger clearance between spray plume and piston crown, the effective time for impingement was reduced.

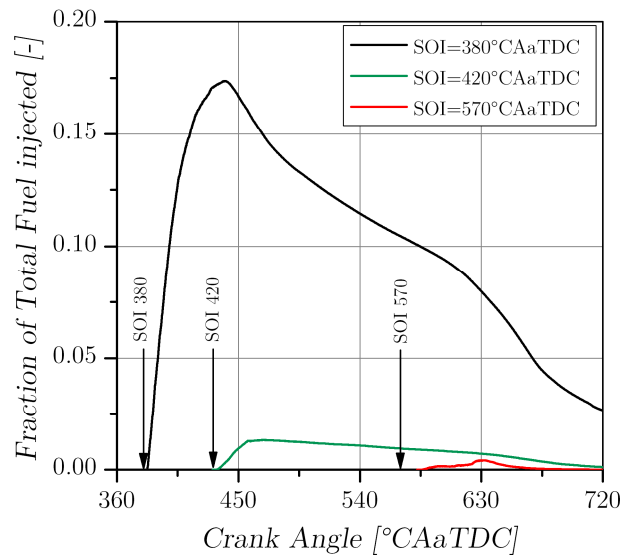


Figure 6.11: Evolution of the wall film deposition depending on the start of injection (SOI)

This dependency on SOI was utilised to validate the wall film results with accompanying FSN measurements. Looking at [Figure 6.12](#), the simulated film fractions at TDC are added as green bars, whereas associated FSNs are plotted in grey. Comparing the drop in wall film from SOI = 380 to

420 °CAaTDC with the associated FSN, a good agreement with experiments can be stated. At the test-bench, minimum soot emissions were detected for $\text{SOI} = 420^\circ\text{CAaTDC}$. For injections beyond this value, the FSN increased again steadily. However, simulations yielded almost zero wall film even for a very late injection starting at 570 °CAaTDC. This observation can be explained by the insufficient time available for fuel evaporation and homogenisation for retarded SOIs. Resulting un-vaporised droplets are responsible for fuel-rich areas which are burning incompletely under oxygen shortage. This was confirmed by the detected hydrocarbon raw emissions (orange bars) that initially remained on a stable level of 250 ppm and started to increase for later injection timings beyond 1000 ppm.

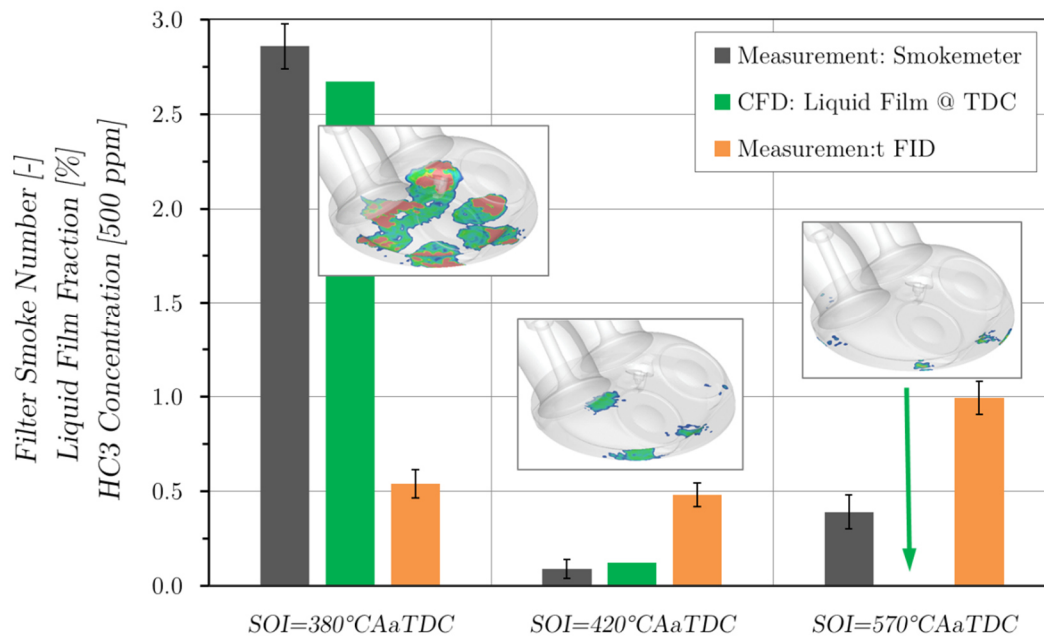


Figure 6.12: Comparison between the measured smoke number and the remaining wall film fraction at TDC, the measured HC raw emissions and the coefficient of variation of IMEP for different injection timings

The insufficient mixture homogenisation could also be reproduced with CFD simulations. In [Figure 6.13](#) the Lambda distribution at TDC is shown as probability density functions for the same SOIs as in [Figure 6.12](#). The earlier the injection proceeded, the more distinct was the homogenisation of fuel vapour and air, as indicated by the peak around the global stoichiometric Lambda for SOI at 380 °CA (black curve). Despite an extensive spatial extension of wall film for this setup, fuel-rich areas below Lambda 0.8 were hardly noticeable in the probability density curve. Even though more than 80 % of the initial wall film was evaporating (see [Figure 6.11](#)), it was captured in just a very limited layer upon the surface and had a minor impact on mixture homogenisation.

For the “minimum FSN” case at $\text{SOI} = 420^\circ\text{CA}$ (green curve), already a second peak started to develop in the fuel-rich region around Lambda 0.9, although the HC emissions remained on a low level. This suggests that slightly rich areas can be consumed entirely throughout the combustion process. In contrast, for late injection, a significant portion of the charge even lay below Lambda 0.6 (red curve) which led to distinct HC emissions. The insufficient mixture preparation becomes additionally apparent by the wide distribution exhibiting no distinct maximum around Lambda 1.

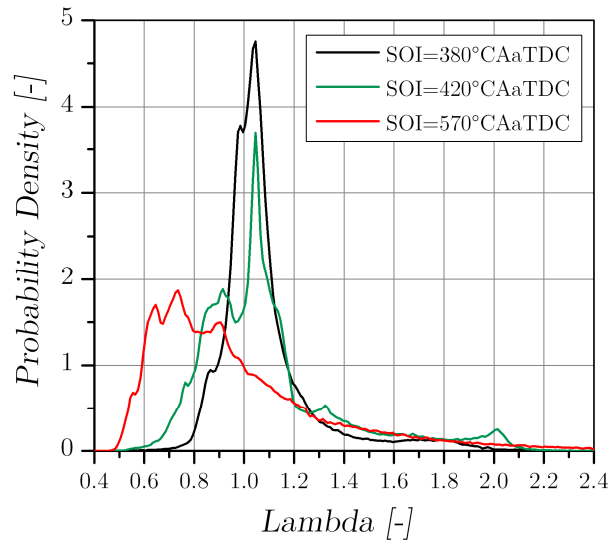


Figure 6.13: Lambda Distribution at TDC for different injection timings

The correlation of predicted wall film with the measured soot emissions suggests that the impingement process of injected fuel on the wall with subsequent evaporation is modelled appropriately. This, together with the approximation of the real fuel's evaporation behaviour by a multi-component hydrocarbon surrogate allows to fully capture the fuel's impact on charge inhomogeneities.

6.5. Impact of Fuel Evaporation on Temperature Inhomogeneities

Autoignition processes are strongly determined not only by the temperature level itself [61] but also by arising temperature gradients [85]. For that reason all of the previously mentioned model adaptations and validations regarding fuel, spray and liquid film were performed because a high model accuracy was essential to gain reliable results about the mixture formation. As was clarified by Figure 1.5 on page 4, pre-ignition is primarily observed at low engine speed under high-load. Certainly, due to a longer available time, a lower speed entails a higher risk for completion of the autoignition process. Nevertheless, the thermal conditions driven by inhomogeneities are the basis for a critical autoignition sequence. For that reason, in the following, low speed results are compared to a high-speed operating point at the same load to gain information about the requirement for pre-ignition.

To some extent temperature inhomogeneities are caused by the heating of the fresh charge on hot cylinder walls but a dominant influence is also arising from the evaporative cooling of injected fuel. Evidence for this can be seen in Figure 6.14, showing the Lambda values of all cylinder cells at TDC (about 100,000 cells) plotted against their respective temperature.

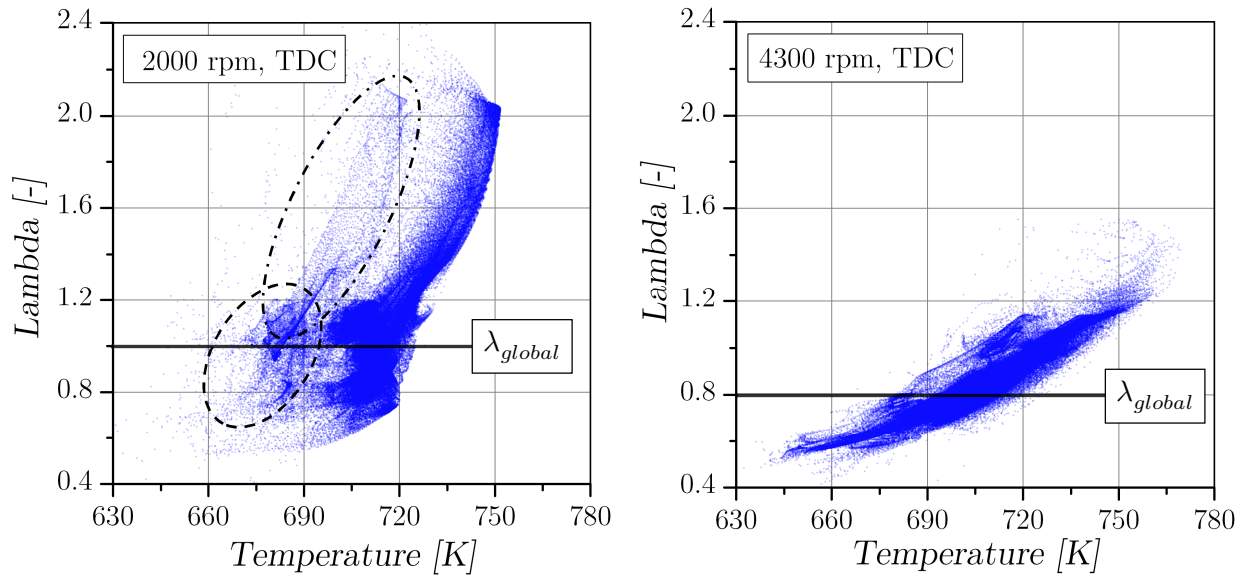


Figure 6.14: CFD cell data showing the dependency between Lambda and temperature for 2000 rpm (left) and 4300 rpm (right) at TDC

A strong correlation was observed, especially for an elevated speed at 4300 rpm (right diagram in Figure 6.14) because the faster intake air flow led to a strong deflection of the injected spray towards the exhaust valves, see Figure 6.15. This led to regions of higher droplet density which were then cooled down more intensively and vice versa. However, the stratification of fuel was partially compensated in the following due to the higher turbulence level at higher speed. Hence, the overall mixing of rich and lean areas was significantly stronger. This gets obvious in Figure 6.14 when comparing the scatter ranges of Lambda around the respective global values.

When comparing the distributions in Figure 6.14, two separated regions became evident for 2000 rpm (indicated with black lines). The dash-dotted line characterises a transition area between the hotter, fuel-lean areas close to the exhaust valves and the cooler bulk mixture, whereas a fuel-rich and relatively cool area emerged close to the piston below the intake valves (dashed line). Both effects could be traced back to the relatively weak tumble motion with a maximum tumble number of 0.7 during compression at 2000 rpm. Further outcomes on mixture formation of this engine at the desired operating points can be found in [97].

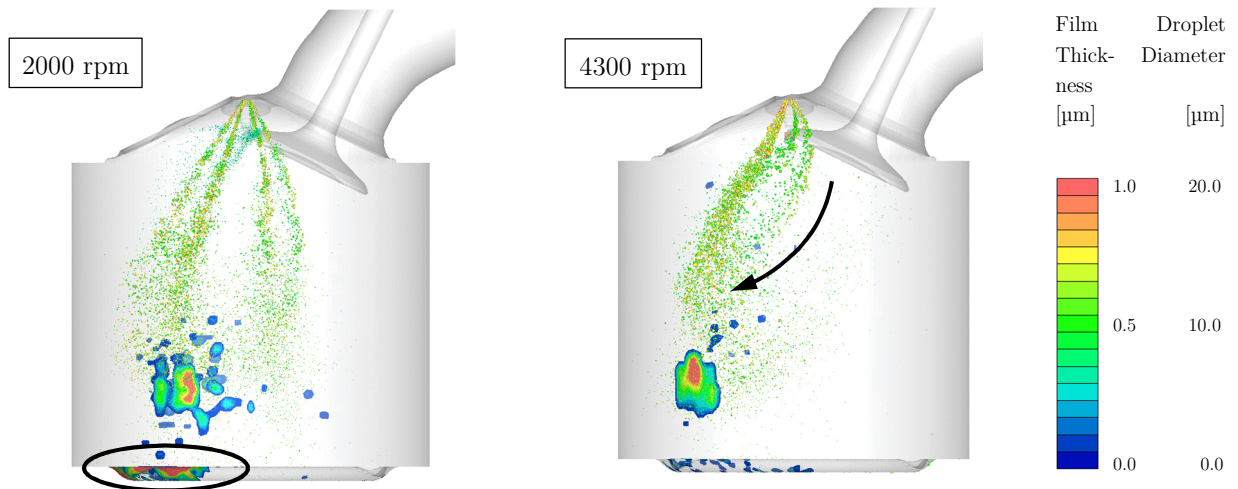


Figure 6.15: Wall film formation and spray deflection compared between 2000 and 4300 rpm during intake-valve-opening at 470 °CA

A stratification of temperature was typical for all investigated operating points. This can be seen by means of a distinct gradient of about 60-100 K that has developed from the intake to the exhaust side, see Figure 6.16. The generally lower temperature level at higher speed was due to the more intensive mixture cooling caused by the richer charge with Lambda 0.8.

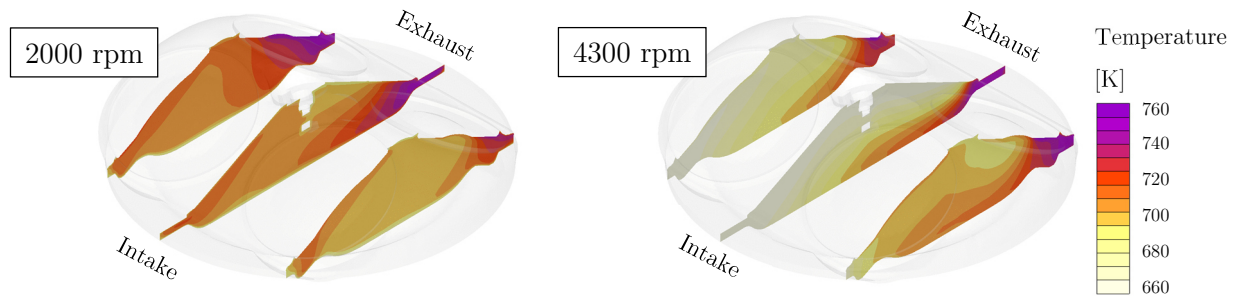


Figure 6.16: Temperature distributions for 2000 rpm ($\lambda = 1$) and 4300 rpm ($\lambda = 0.8$)

The related probability density functions of temperature in Figure 6.17 show a clearly wider distribution for 4300 rpm. In contrast to the stronger mixing with respect to fuel vapour, heat exchange within the charge was significantly less pronounced. The simulations showed that a coupling of both effects is not necessarily given as heat exchange is a relatively slow process being considerably affected by engine speed.

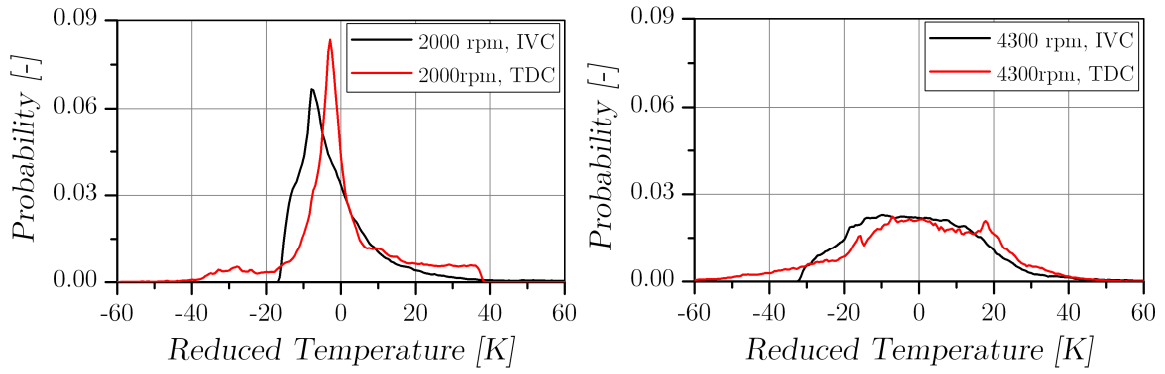


Figure 6.17: Probability density functions of temperature for 2000 and 4300 rpm

The significant dependency between Lambda and temperature revealed that the transport of the injected fuel droplets during the evaporation process must be crucial. Furthermore, fuel that forms liquid film, barely contributes to mixture cooling because most of its heat of vaporisation h_{vap} is provided by the heat fluxes from the wall. Hence, a certain increase of charge temperature may be expected affecting the autoignition tendency. This impact can be evaluated by a simple approach according to [52]. It is assumed that the total amount of fuel is evaporated under stationary conditions, i.e. at the fixed crank angle position IVC in this considerations:

$$\Delta T = \frac{h_{vap} \cdot (frac_{h,Wall} - 1)}{AFR \cdot c_{p,a} + c_{p,L}} \quad (6.7)$$

Where ΔT stands for the mixture cooling relative to the initial charge temperature. The dimensionless parameter $frac_{h,Wall}$ describes the fraction of the overall heat of vaporisation provided by the heat fluxes from the walls \dot{Q} :

$$frac_{h,Wall} = \frac{\dot{Q}}{x_e \dot{m}_a (1/AFR) \cdot h_{vap}} \quad (6.8)$$

RON95 has a relatively low heat of vaporisation h_{vap} compared to other fuels, like alcohols. Together with a typical value of $frac_{h,Wall} < 0.05$ derived from the CFD simulations, the above approach only gave a ~ 1 K warmer charge compared to complete evaporation in air ($frac_{h,Wall} = 0$). This means that the influence of wall film on the charge temperature only plays a minor role. However, its evaporation leads to local wall-near regions of high fuel concentrations. These are particularly of importance and can play a key role for autoignition as ignition delay becomes shorter under slightly rich conditions. The fuel fraction that puddled on the piston was distinctively higher at lower speeds caused by a lower relative velocity between piston and spray tips. The more intensified piston wetting is marked in the left picture of Figure 6.15. Further details about the influence of wall film on the mixture cooling have already been published and can be found in [99].

The main mechanisms that affected both fuel and temperature inhomogeneities can be summarised as follows:

- Charge motion and turbulence level
- Deflection of the injected spray by the intake air flow
- Relative velocity between spray and piston (engine speed/injection pressure)
- Available time for evaporation and mixing (engine speed/injection timing)
- Wall film formation and subsequent evaporation

With respect to pre-ignition, the above findings suggest that critical conditions for autoignition are unlikely to be approached for neither of both speeds. Especially for the PI-critical speed at 2000 rpm, the hottest areas beyond 750 K are extremely lean with Lambda values around 2 what effectively inhibits any ignition reaction. This makes clear that additional triggers are a necessary precondition for pre-ignition. Possible sources and their respective mechanisms will be considered in the following sections.

7. Analyses on the Reactive Impact of Fuel on Pre-Ignition

To study the influence of fuel composition and also fuel droplets on the autoignition tendency of the charge, reaction kinetic calculations were performed in a stochastic reactor model. To validate the autoignition sensitivity of the model fuel, specific boundary and initial conditions of knocking cycles were applied to recalculate the autoignition timing on the basis of low and intermediate temperature chemistry. Thereby, the formation of chemical species and especially reactive radicals that characterise autoignition are resolved over crank angle. The stochastic reactor model (SRM) enables the introduction of temperature inhomogeneities. For that reason, CFD results served to initialise reactor particles with probability density functions.

7.1. Implementation of a Gasoline Surrogate in a Stochastic Reactor Model

The following analyses are carried out in a specialised zero-dimensional stochastic reactor model for in-cylinder combustion. Thermo, chemical and fluid dynamic processes are solved simultaneously including detailed chemical kinetics [100]. An ensemble of so called “stochastic particles” is used to approximate the distribution of in-cylinder properties such as the composition of chemical species and the temperature with probability density functions. Each particle represents a statistical portion of the in-cylinder volume. At each time-step heat transfer, turbulent mixing and chemical processes are solved for each stochastic particle. A chemical kinetic mechanism that represents the fuel’s chemical properties appropriately is of great importance for studies on autoignition problems.

The fuel autoignition quality is commonly specified by the Research and Motor Octane Number, RON and MON. These values are determined in standard knock tests in CFR engines by comparing the fuel’s knock behaviour to a blend of knock-resistant iso-octane (100 RON) and knock-prone n-heptane (0 RON). The volume percentage of iso-octane for equal knock tendency determines the octane number. The knock tendency of practical fuels in engine operation is quite different from a PRF because they are complex mixtures of paraffines, olefins, aromatics and oxygenates. The same fuel can match different PRFs at different operating conditions due to the pronounced NTC behaviour of paraffines. Therefore, typical European premium fuel of 95 RON yields 95 PRF (95 % iso-octane) in the RON test but only 85 PRF in the more critical MON test. The consideration of this behaviour is of great importance when evaluating the autoignition tendency of the charge.

Widely used gasoline surrogates that are capable to match the difference between RON and MON are tri-component Toluene-Reference-Fuels (TRF), for which the base chemistry of iso-octane and n-heptane is enhanced by the mechanism of the toluene as well as the cross-reactions between the components. Andrae et al. [101] presented a detailed TRF chemical kinetic scheme (1121 species and 4959 reactions) that was validated with ignition delay measurements in shock tubes and HCCI engines. However, for practical application in engine models this mechanism was reduced to 137

species and 633 reactions [102] and further validated with RCM experiments and measurements of laminar flame speeds. In the following, this semidetailed TRF served to validate the autoignition quality of the used model composition against measurements at the knock limit.

While for a PRF there exists a direct link between the fuel composition and the octane number, no such link is given for TRF blends. Synergistic and antagonistic blending effects between the three components have to be considered. Morgan et al. [103] described a mapping procedure to determine the TRF composition for any combinations of RON and MON on the basis of 2nd order response surface models. In this way the appropriate TRF blend fitting the test bench premium fuel with 95 RON and 85 MON was obtained and is listed in [Table 7.1](#) next to the values of the pure components.

Table 7.1: Octane numbers of different primary and toluene reference fuel mixtures

Toluene Reference Fuel (TRF)			RON	MON
iso-Octane [Vol%]	n-Heptane [Vol%]	Toluene [Vol%]		
100.0	0.0	0.0	100.0	100.0
0.0	100.0	0.0	0.0	0.0
0.0	0.0	100.0	120.0	109.0
95.0	5.0	0.0	95.0	95.0
20.64	18.82	60.54	95.0	85.0

7.2. Determination of the Autoignition Limit via Knock Cycles

To guarantee an appropriate model accuracy of the surrogate fuel mechanism not only under standard RON and MON conditions but also in real engine usage, a validation was carried out against measured knock cycles. End gas autoignition was calculated on the basis of low and intermediate temperature chemistry and compared to the measured knock timing. To gain highest model sensitivity, cycles had to be determined that lay closest to the knock limit. For the test run, spark advance was adjusted to mild knock rate that was defined as a fraction of 2–3 % detected knock events. To find out cycle characteristics that indicate knock tendency, a multi-cycle process simulation was carried out for 150 consecutive measured cycles with a three-pressure-analysis.

Although cyclic variations of global cylinder properties remained inconspicuous within a narrow margin, the combustion phase showed considerable differences already from the very beginning of the flame propagation. The left diagram in [Figure 7.1](#) illustrates the cyclic variability of the 10–90 % burn duration and hence the entire combustion phase. Although the knock sensor applied on the test engine detected knocking just for the two red marked cycles, the multi-cycle simulation revealed an irregular heat release for several other cycles (yellow dots). An evaluation of the early combustion phase characterised by the 0–2 % burn duration (MFB0-2%) in [Figure 7.1](#) (right) makes clear that

there exists a strong correlation with the autoignition tendency. Autoignition was observed for all cycles with a short 0–2 % burn duration in the range of 10 °CA and below.

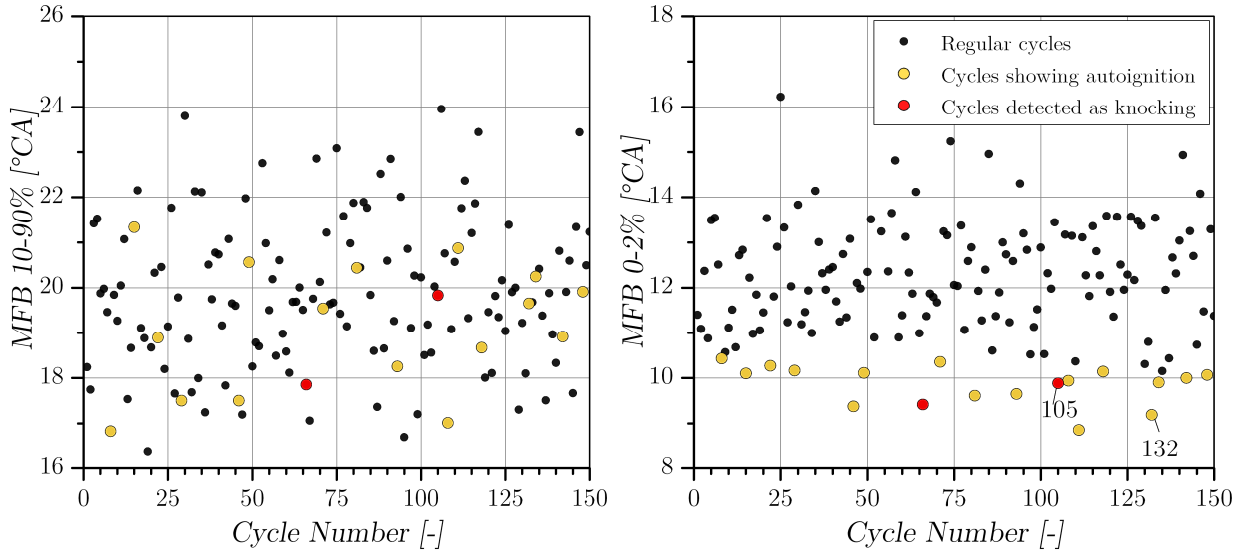


Figure 7.1: Measurements at 2 % knock rate: 10–90 % burn duration (left) and the 0–2 % burn duration (right) for 150 consecutive cycles

To demonstrate the difference between autoignition and knocking, knock cycle 105 is compared to autoignition cycle 132 in terms of pressure and heat release, see [Figure 7.2](#). As can be seen, the heat release rate of both cycles was very similar, but only one of them resulted in knocking pressure oscillations. This reveals that basically all cycles with rapid early combustion phase exhibit critical exothermic pre-reactions, but apparently cyclic fluctuations in the turbulent flow field finally decide about knocking. This finding is also supported by knock investigations carried out in [104].

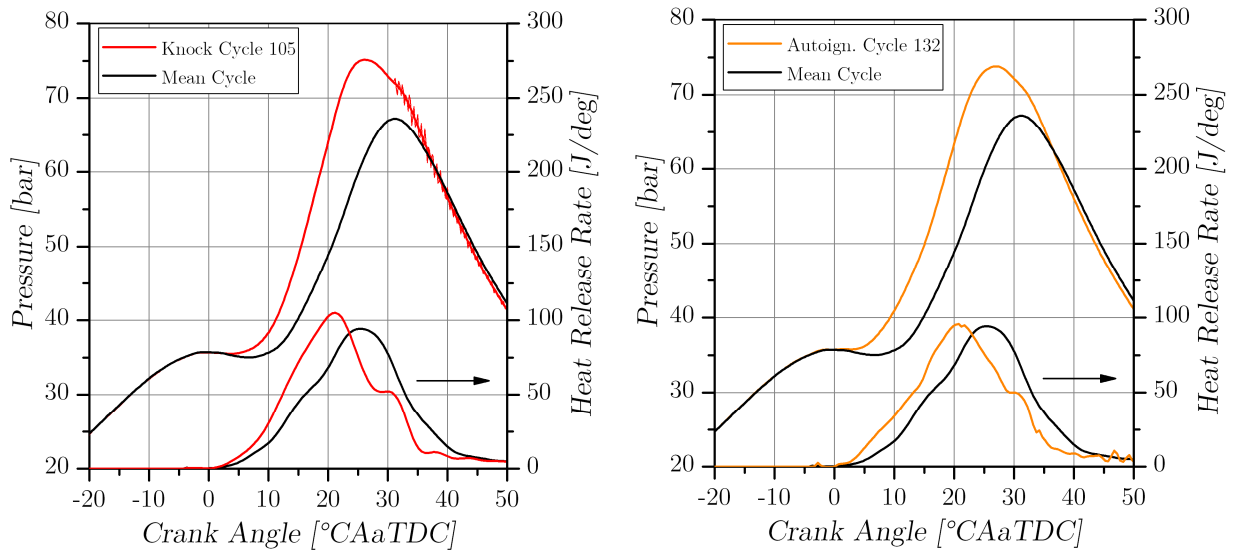


Figure 7.2: Pressure and heat release for a knocking cycle (left) and an autoigniting cycle without knock oscillations (right)

The early flame kernel development phase obviously has an impact on the following combustion process and hence the end-gas properties. As can be seen in [Figure 7.3](#), the position at which 50 % of the fuel mass is burned (MFB50%), exhibits a strong linear dependency ($R^2 = 0.78$) on the 0-2% burn duration MFB0-2% (black dots). This means that the very first growth of the flame determines the phasing of the entire combustion process. Interestingly, no distinct correlation is given between the MFB10-90% and MFB50% (red dots) and also between the MFB0-2% and MFB10-90% (green dots). This reveals that with proceeding combustion the influence of the early flame decreases and that the flame propagation increasingly gets dominated by the stochastic turbulent flow field. Nevertheless, the initial flame kernel is decisive up to MFB50%, at which critical pressures and temperatures are reached in the unburned zone to initiate pre-reactions. This explains the connection between the early flame and the much later occurring autoignition.

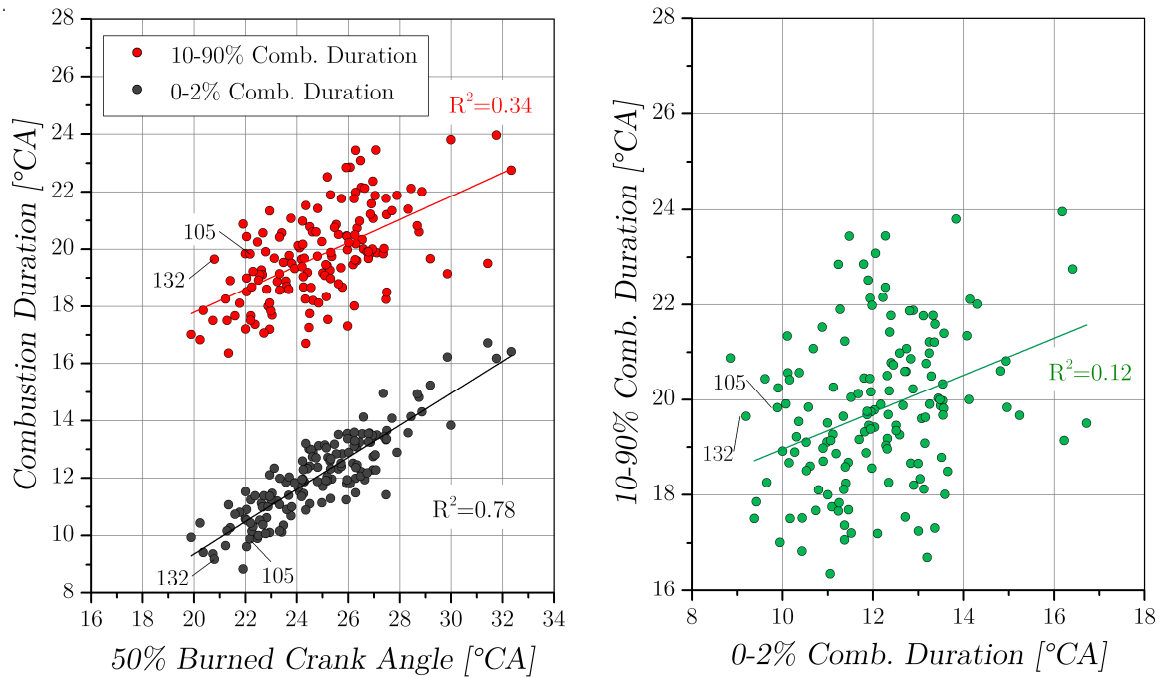


Figure 7.3: Correlations between the early combustion phase (MFB0-2%), the 50 % mass fraction burn point (MFB50%) and the entire combustion duration (MFB10-90%)

From Figure 7.2 it was derived that for two cycles with almost identical traces of heat release, autoignition occurred once with and once without knocking oscillations. This suggests that the desired heat release represents a critical borderline for autoignition. Therefore, knock cycle 105 was regarded as suitable for evaluating the autoignition sensitivity of the TRF blend in the stochastic reactor model.

7.3. Validation of the Surrogate Fuel's Autoignition Sensitivity

The stochastic reactor model was set up in order to recalculate the heat release and the cylinder pressure of a cycle lying close to the knock limit, which was determined in the last section. Thereby, the conditions in the unburned zone were comparable to the real process and consequently critical to autoignition. The objective was to validate the autoignition behaviour of the TRF blend listed in Table 7.1 and to analyse the crank angle resolved evolution of species in the end gas characterising the autoignition process.

The specific boundary and initial conditions of the representative knock cycle were applied to the reactor model to recalculate the initiation of knocking on the basis of low temperature chemistry. The wall temperatures were calculated in advance with a wall temperature solver integrated in the 1D cycle simulation that employs a simplified FE model. Inhomogeneities were accounted for with a number of 100 reactor particles. Therefore, CFD results at intake valve closing were extracted to initialise the particles with the probability density function of cylinder temperature. The temperature spectrum for about 620.000 cells of the CFD model at IVC is indicated by black bars in the left diagram of [Figure 7.4](#). This distribution was then transferred to the 100 stochastic particles (blue bars).

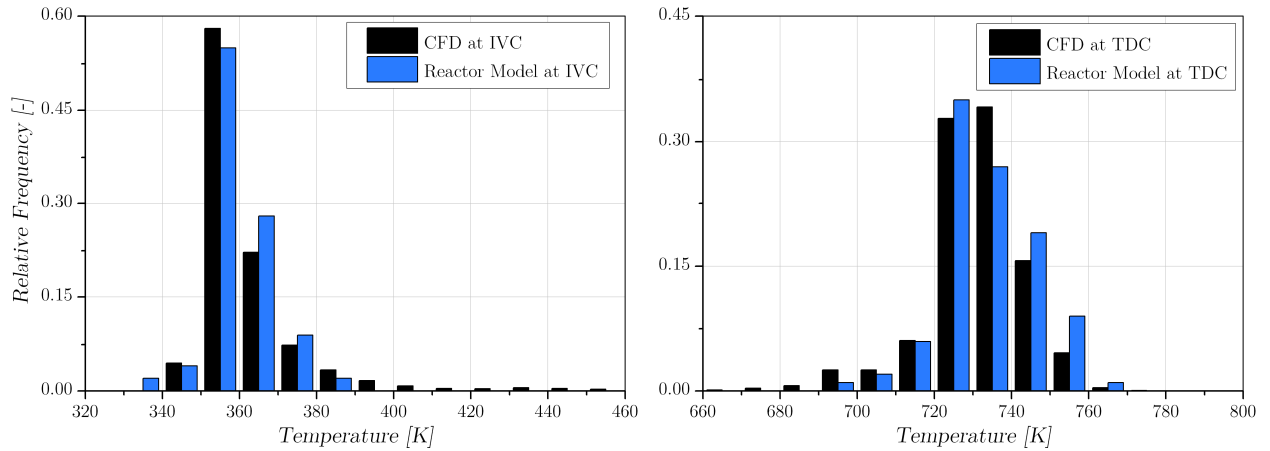


Figure 7.4: Temperature distribution at inlet valve closing (left) and TDC (right)

During compression, the reactor temperature distribution is dependent on stochastic heat exchange, turbulent mixing and cylinder wall heat transfer. Therefore, the turbulent mixing parameters were adjusted in order to find the best possible match with the temperature distribution from CFD. A good agreement at TDC, which is depicted in the right diagram of Figure 7.4, reveals that a proper setup was found for the stochastic mixing process during compression. Especially the formation of knock sensitive areas in the mid and high temperature range were represented properly. The slight lack of coldest particles played only a minor role for autoignition and was therefore accepted. However, the final mean compression temperatures of CFD simulation and reactor model were equal.

The same tuning procedure as for the temperature was carried out for the fuel vapour distribution. CFD results presented in Section 0 imply that there is an inverse relationship between fuel vapour and temperature caused by the evaporative cooling effect of the spray. Therefore, a lower fuel fraction was assigned with a higher probability to the hotter particles and vice versa.

The heat release of the knock cycle was rebuilt using a Wiebe approach in order to find the best possible fit to the measured cylinder pressure. As shown in the right diagram of [Figure 7.5](#), the heat release in the experiments was somewhat differing from a classical Wiebe function, which is why certain deviations had to be accepted. However, good agreement was found for the overall shape of heat release as well as the maximum pressure.

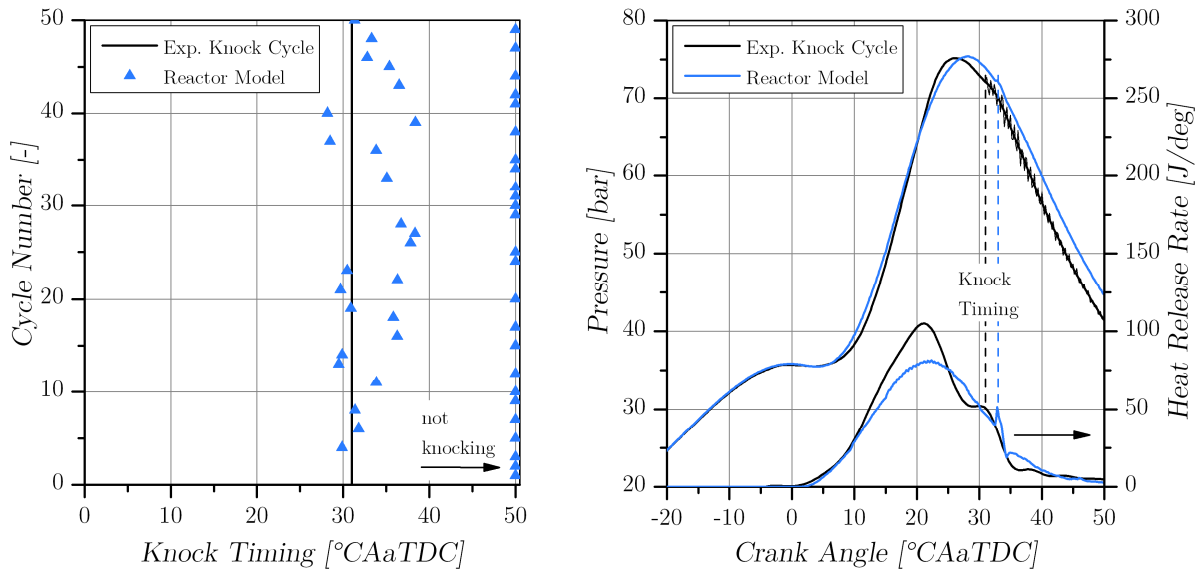


Figure 7.5: Calculated knock timings for representative cycles at the knock limit with an adjusted spark advance for 2% knock rate (left); Pressure and heat release for cycle no. 6 with indicated position of knock timing close to the experiment

Because the SRM is a zero dimensional approach, the particle burn order is defined randomly without solving spatial flame propagation. For each cycle, this has a stochastic effect on the conditions in the end-gas and hence the autoignition probability. Therefore, a sufficient number of cycles has to be evaluated to gain reliable information about autoignition. The results of 50 cycles are shown in the left diagram of [Figure 7.5](#). Pressure and heat release of cycle no. 6 with knock timing close to the experiment is shown in the right diagram of [Figure 7.5](#). About 50 % of the calculated cycles attained autoignition until simulation end at 50 °CAaTDC. This variability confirms the mild knock tendency of the desired operating point and reproduces the borderline situation between autoignition and knocking, as shown in [Figure 7.2](#).

The reason for the variability of knock timing is explained in more detail in [Figure 7.6](#) by means of the reactor particles' temperature histories. All regular burning particles are depicted as black lines. They are characterised by an almost vertical increase to a high temperature level above 2500 K which means that the particle has been entrained into the hot flame. In contrast to this, autoigniting particles showed a considerably different behaviour. Marked with red colour, these particles were passing a kind of heating process with a progressive rise in temperature during the first stage of

ignition until hot thermal ignition completed the autoignition process. Further details have already been published and can be found in [105,106].

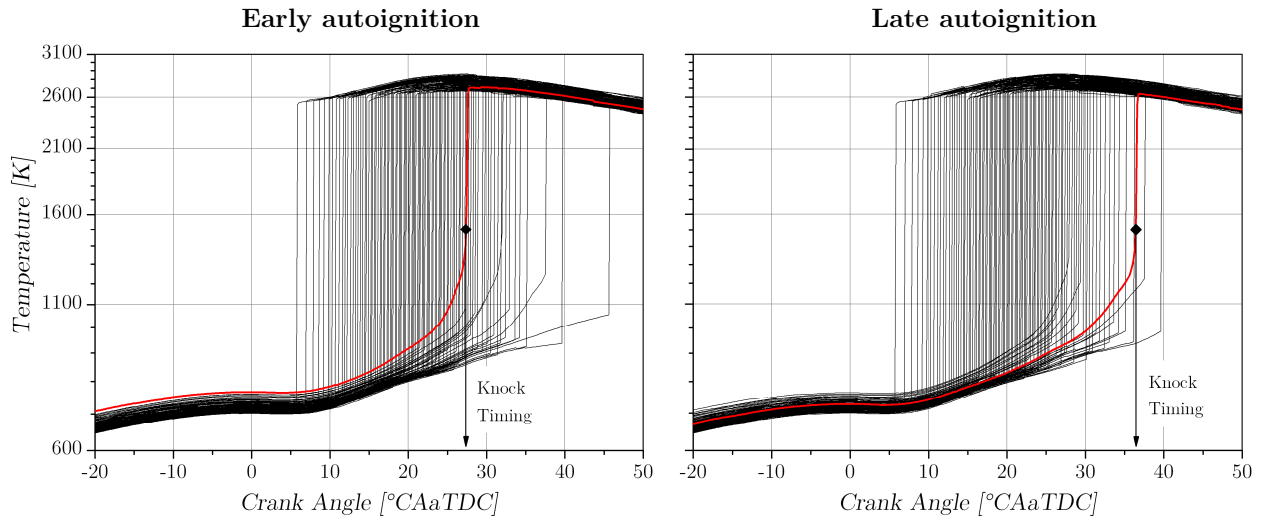


Figure 7.6: Particle temperatures for two different particle combustion order scenarios: early autoignition if cool particles are burned at first (left); late autoignition if hot particles are burned at first (right)

The time when autoignition sets in, depends on the end-gas temperature and hence on the particle combustion order. If primarily cooler particles are burned first, the hotter remaining end-gas ignites rather early. The resulting two extreme cases for early and late autoignition are illustrated in Figure 7.6. Both scenarios are comparable to autoignition events originating from regions with different temperature levels what suggests that knocking can arise quite independently of flame propagation. Hence, the end-gas at this operating point is also critical if hotter regions are burned first. This is in accordance with experimental knock detections carried out with a fibre optic spark plug, as depicted in the left image in Figure 7.7. With eight optical channels the knock critical regions were covered for recording the knock events.

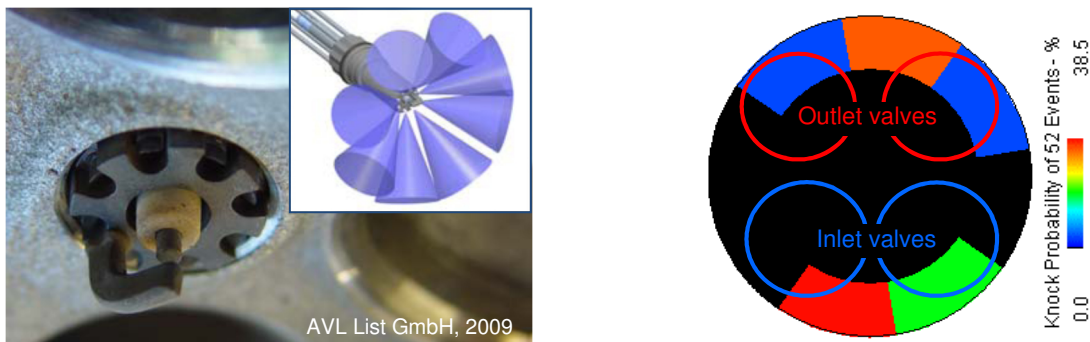


Figure 7.7: AVL VisioKnock spark plug (left) and its application in optical monitoring of the spatial knock probability (right)

The right image in Figure 7.7 shows the result of the relative knock occurrence for 52 recorded knock events. The optical measurement identified an almost equal probability for irregular combustion at the inlet and at the outlet area, what was in good agreement with the simulations carried out in the SRM.

As outlined above, the chosen surrogate composition is able to reproduce the autoignition probability at the sensitive knock limit and is therefore regarded as appropriate for pre-ignition studies.

7.4. Modelling of Remaining Fuel Droplets

Direct injection with rail pressures up to 200 bar generates a fine spray with effective evaporation characteristics. The existence of liquid fuel droplets up to TDC is therefore unlikely. However, as was discussed in Figure 6.10, spray cones are striking against cylinder and piston walls forming liquid film. It is therefore conceivable, that considerably bigger secondary droplets can be stripped off from regions with intensified wall wetting. Generally, the fuel spray immediately evaporates and cools the charge proportional to the local fuel evaporation rate. This leads to a characteristic relationship between local temperature and air-fuel ratio, as shown in Figure 6.14. However, if a droplet would exist around TDC, its evaporation mass flow may be sufficient for generating high local fuel fractions at simultaneously high temperatures. The intensity of pre-reactions in the low-temperature oxidation pathway is depending on the fuel concentration. The probability for chain branching reactions is directly proportional to the local amount of fuel [57,58]. Hence, fuel-rich zones forming close to a droplet surface can ignite more quickly. This raises the possibility for autoignition already before spark timing.

To investigate the local fuel fractions that are critical for pre-ignition, a single fuel droplet was assumed to evaporate in the hottest prevailing region of the inhomogeneous temperature distribution implemented in a stochastic reactor model; see red marked particle temperature history in Figure 7.8.

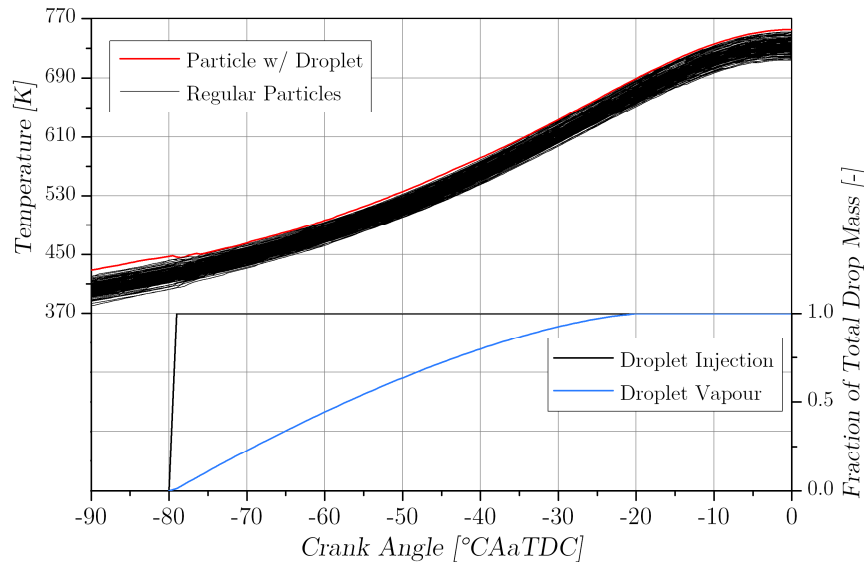


Figure 7.8: Particle temperature histories of 100 reactor particles (top); hottest particle selected for droplet injection is marked red; droplet injection and evaporation (bottom)

To mimic the droplet separation from wetted walls, one fuel droplet was injected during compression stroke into the stoichiometric charge. In the hot environment, the drop mass decreased rapidly what raised the local fuel fraction, see blue curve in Figure 7.8. In the following, the impact of local vapour fractions on pre-ignition is studied by varying the initial mass of the injected droplet.

Figure 7.9 gives an impression of the autoignition tendency of local fuel-rich regions indicated by the formation of hydroperoxy radicals HO_2 and the resulting heat release caused by exothermal reactions during compression until ignition.

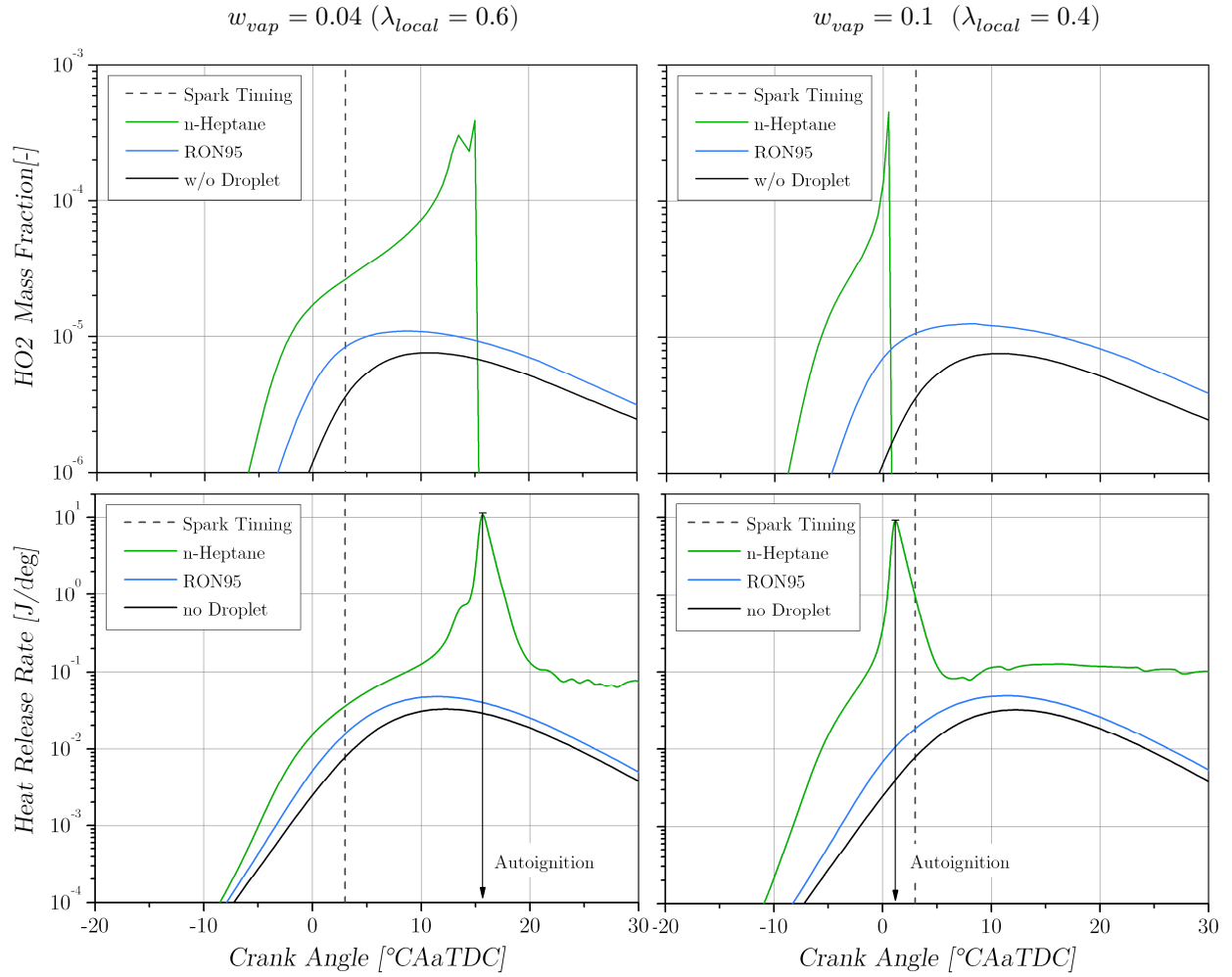


Figure 7.9: Autoignition tendency for low (left) and high (right) droplet vapour fractions evaluated by the formation of hydroperoxy radicals HO_2 (top) and the heat release rate (bottom)

For the calculations, spark ignition was deactivated in order to evaluate the general autoignition trend without the influence of the propagating regular flame. The black curves denote the baseline results for the hottest and stoichiometric particle without additional droplet injection. It becomes clear, that pre-reactions are evolving but remain on a relatively low level which is too weak for autoignition. The maximum mass fraction of the reactive intermediate HO_2 occurs significantly after the maximum temperature at TDC what demonstrates the slow kinetic response and therefore the general uncritical pre-ignition tendency of the charge.

The results with addition of RON95 droplets, which are represented by the TRF blend according to Table 7.1, are indicated by blue lines in Figure 7.9. The pre-reactions forming HO_2 are getting more pronounced as the local fuel fraction is raised by the additional droplet vapour. However, autoignition was not observable over the entire range, not even with a significantly higher droplet vapour mass fraction of 10 % (right diagrams). This clearly points out that the reactivity of typical RON95 fuel is generally too weak to cause pre-ignition even under distinctly rich and critical temperature conditions around 750 K.

Droplets that are separated from combustion chamber walls are rather unlikely to consist of the original RON95 composition. Continuous evaporation of volatile components from the fuel takes place during the entire residence time on a hot surface. Especially in regions like the piston crevice, where liquid can accumulate over many cycles, demixing of fuel is likely to generate liquid mixtures of mainly high-boiling components. Especially for alkanes, such low-volatile species are characterised by a longer carbon chain length and hence weaker autoignition resistance. To account for severe fuel demixing in SRM simulations, neat n-heptane was assumed as surrogate fuel because it represents the most reactive parent fuel component in the TRF mechanism. The green traces in Figure 7.9 make clear that in contrast to RON95 autoignition gets critical with n-heptane. For a moderate droplet vapour fraction of 4 %, a distinct two-stage ignition becomes visible in the radical species formation as well as the resulting heat release (left diagrams). For a high vapour fraction of 10 % the low temperature reactions are much more pronounced and hence facilitate an accelerated and earlier ignition (right diagrams). The higher reactivity becomes apparent as a steep gradient in the HO_2 formation leading to a rapid ignition already before spark timing.

To study the potential pre-ignition severity of n-heptane, the impact of droplet vapour fraction on autoignition timing was carried out more detailed, see [Figure 7.10](#). For vapour fractions below 4 %, a late autoignition was inhibited by the progressing expansion stroke causing a drop in charge temperature and hence freezing further reactions. With rising vapour fraction, autoignition gradually advances before spark timing because the low-temperature reactions are becoming more intense in richer mixtures. A progressive rise of the critical vapour fraction curve reveals that an exceptionally high local amount of fuel would be required to further advance autoignition. However, no ignition is encountered for vapour fractions above 14 %. For such fuel-rich mixtures with theoretical Lambda values below 0.25 the additional heat capacity of the fuel vapour becomes decisive. Thus the heat from low-temperature reactions gets balanced by the additional thermal mass what prevents autoignition of even richer fuels.

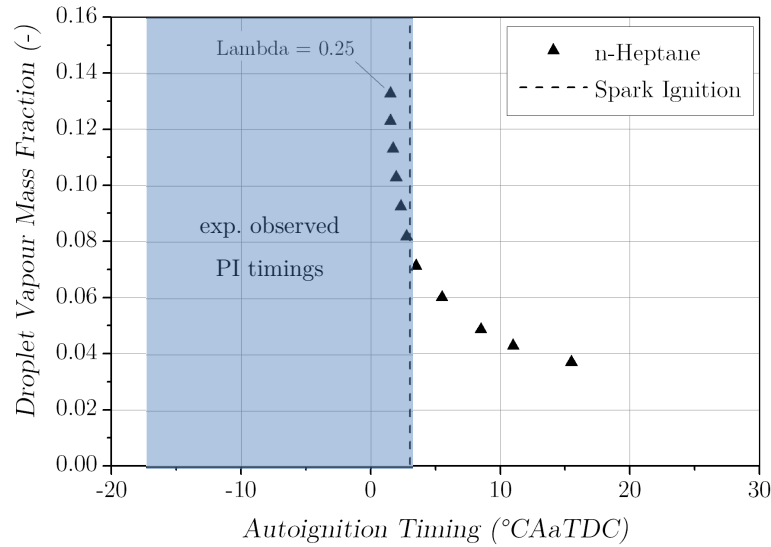


Figure 7.10: Effect of n-heptane droplet vapour on the autoignition timing of a stoichiometric RON95 mixture

For the desired operating point the earliest possible pre-ignition timing caused by local n-heptane vapour lay at 1.5 °CAaTDC and therefore close to spark timing. This means that even if severe demixing of the fuel is assumed for a droplet that survives in the hottest part of the charge, early pre-ignition as observed experimentally is not possible. Therefore, the reason why several experimental studies [29,25,21] were not able to establish a correlation between chemical fuel properties or fuel octane numbers and pre-ignition tendency is that gasoline is generally too resistant with respect to autoignition to show any clear impact.

Besides focussing on severe pre-ignition, the above results reveal that under rare circumstances the ignition timing can be slightly advanced by fuel droplet ignition. Effectively such an event would be recognised as moderate knocking combustion rather than pre-ignition. Looking at the statistics of observed pre-ignition cycles in Figure 5.1 on page 40, a noticeable group of knocking cycles (yellow symbols) occurred separated from pre-ignition events. Keeping in mind that knock control was active during the tests, such cycles shouldn't have occurred since spark timing had already been retarded in advance. Therefore, an uncontrollable premature ignition due to demixed fuel droplets would deliver a plausible explanation for this kind of knocking cycles. However, it should be mentioned that such events were extremely rare (about 30) compared to the already rare number of detected pre-ignition cycles (about 800) during the entire measurement campaign.

8. Analyses on Oil Droplet Induced Pre-Ignition

As was pointed out in Section 2.2, the question whether droplets or particles are responsible for pre-ignition, depends on the particular engine configuration. For the examined engine in this study, the presence of hot glowing particles in initial events couldn't be confirmed by high speed imaging, see Section 5.3. Hence, the hypothesis of droplet autoignition is the central point for the modelling approach applied in this work.

8.1. Pre-Ignition Process Chain

The logical process chain that is derived from the literature review as well as from the preliminary modelling activities is visualized in [Figure 8.1](#).

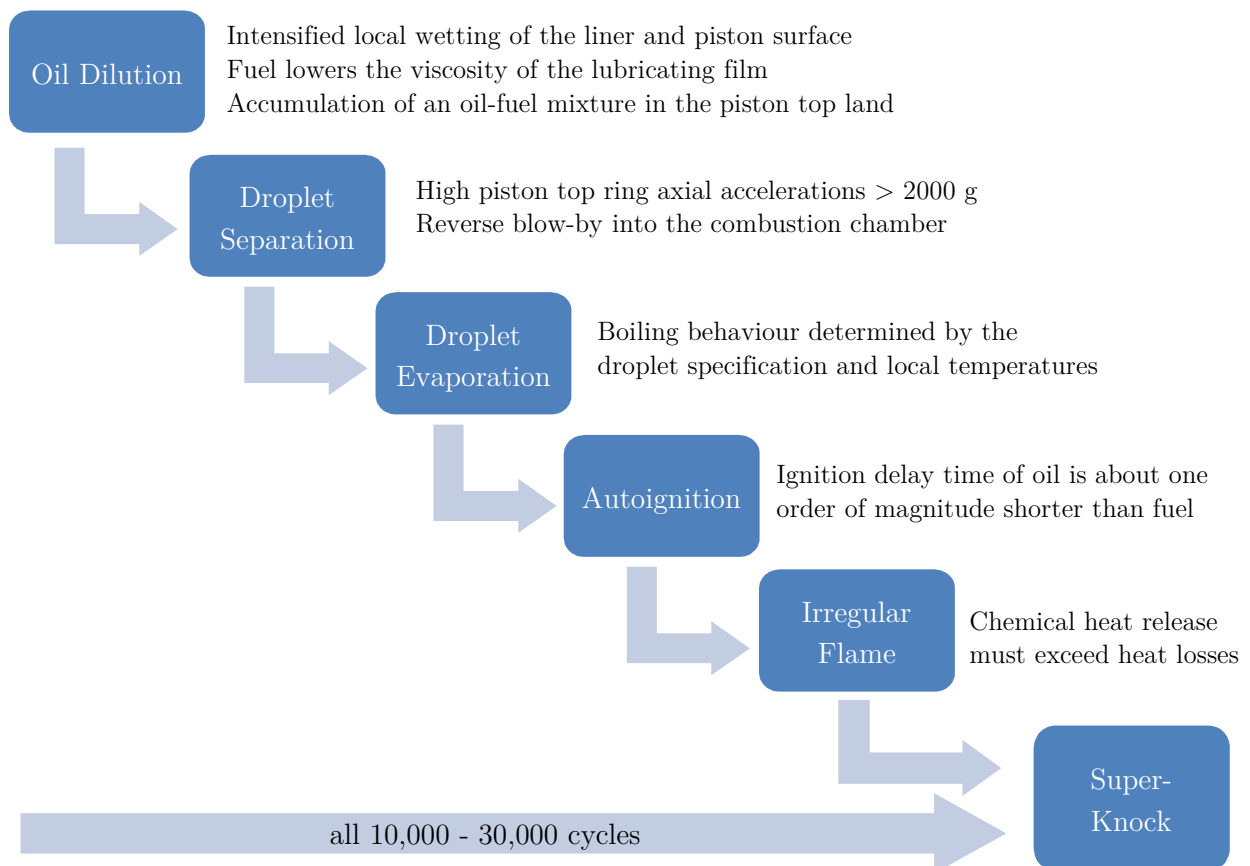


Figure 8.1: Overview of the individual sub-processes leading to pre-ignition with super-knock caused by the intrusion of oil droplets into the combustion chamber

Each step is determined by stochastic processes of the turbulent flow field. Thus, the probability that all necessary conditions of the entire process chain are fulfilled, is expected to be rather low. However, this is in accordance with the findings from the pre-ignition test runs where such events were observed rarely all 10,000 – 30,000 cycles.

The numerical results already presented in the preceding section indicated that the reactivity of local spots has to be significantly higher compared to gasoline or even n-heptane to trigger pre-ignition already at -17°CAaTDC . Lubricating oil with an extremely low autoignition resistance is an obvious candidate to play a key role for pre-ignition. Hence, in the following, the plausibility of the entire process chain starting from fuel impingement until autoignition of evaporating droplets will be validated and analysed via combining CFD with reaction kinetics simulations.

8.2. Evaluation of Fuel Deposition and Oil Dilution

To ensure efficient evaporation and homogenisation within shortest times available until ignition, injection pressures of DI-systems are approaching values about one order of magnitude higher compared to PFI engines. Due to the increased flow rates through the injector holes, spray cones penetrate far into the combustion chamber, leading to a greater risk of fuel deposition on opposing surfaces. Additionally, the fine spray is prone for getting deflected by the intake air flow. The effects of both factors on wall wetting become clear by the simulation of an injection event, as shown in [Figure 8.2](#).

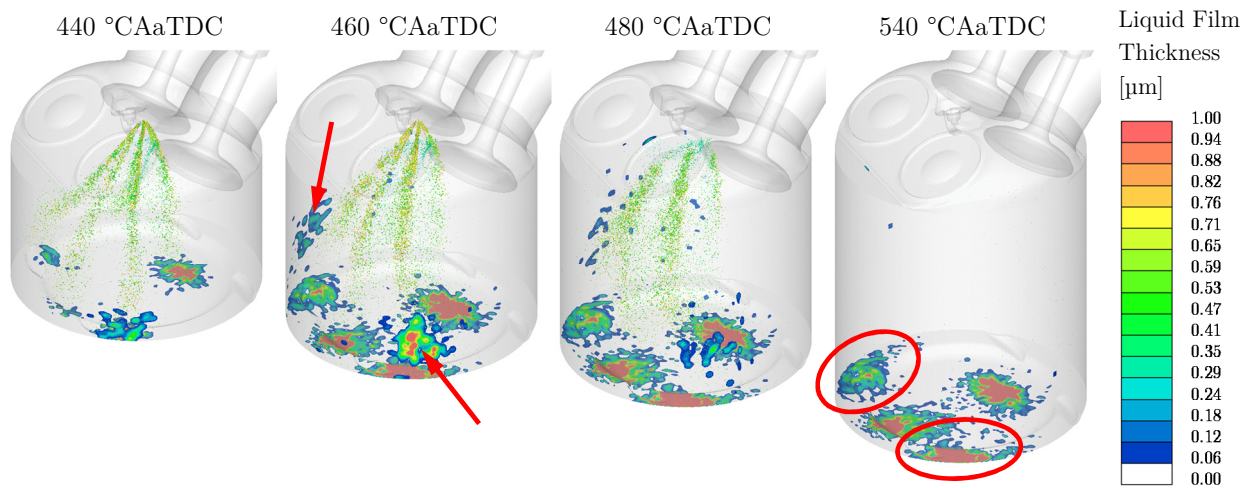


Figure 8.2: Deposition of fuel on the liner (arrows) and close to the piston crevice (circles)

Around the time of highest intake mass flow (440 – 450 $^{\circ}\text{CAaTDC}$), the liner wetting reaches the maximum due to the strong deflection of the spray, see blue line in [Figure 8.3](#). This leads to two local wall film spots on the exhaust side of the liner (marked with arrows in [Figure 8.2](#)). Fuel droplets hitting the liner surface are likely to eject oil from the lubricating film when splashing at the wall.

Throughout the entire injection sequence, critical impingement is also observed at the piston crown close to the liner (red circles). Towards TDC, randomly distributed piston film increasingly evaporates leading to a concentration of the film to limited areas. Due to the long-term droplet-wall interaction in these regions, the resulting wall film density is too high for the film to evaporate completely, see green line in Figure 8.3. A mixing of fuel and lube oil and an accumulation of the oil-fuel-mixture in the piston crevice volume of the top land is therefore probable. As the viscosity of fuel is about two orders of magnitude lower than that of typical engine oils, mixing with already minor quantities of fuel can be expected to cause a distinctive reduction of the viscosity. In this way, a separation of droplets with critical autoignition resistance is significantly facilitated.

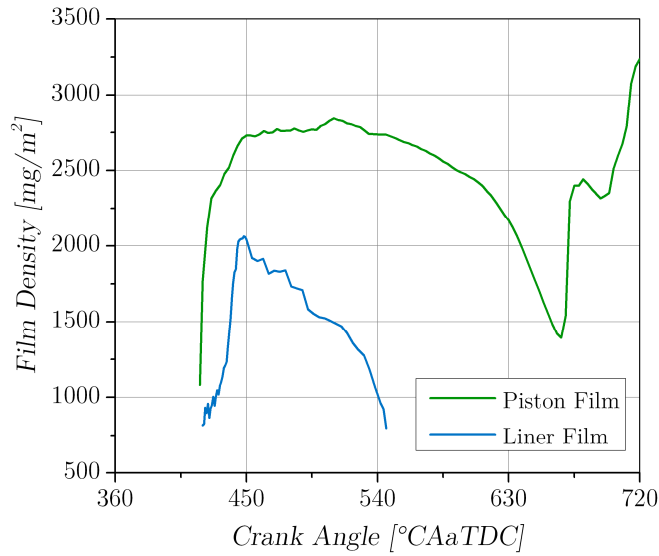


Figure 8.3: Development of the average film density (film mass/ film area) for piston and liner

The release of oil-fuel droplets is additionally supported by external forces acting on the liquid. In [21] and [28] it was shown with a 3D piston ring dynamic model that a reverse gas flow exists from the top ring crevice towards the combustion chamber until compression. In this way gas is pushed into the combustion chamber over the wetted crevice volume for a significant amount of time. Additionally, high piston ring axial accelerations of more than an order higher relative to the piston were calculated in [21], to occur during intake and compression. Consequently, a superposition of fuel-oil interaction, reverse-blow-by gas flow as well as piston ring axial acceleration seems to be the key mechanism that is responsible for the entrainment of oil-fuel droplets into the cylinder flow.

8.3. Modelling of Detached Oil-Fuel Droplets

As was outlined above, there is strong evidence that the separation of droplets results from several physical processes that have to occur simultaneously in the piston crevice. A basic requirement for droplet formation is the presence of a sufficient amount of liquid between piston and liner. In Figure 8.2 it was shown that for the desired engine setup a significant fuel film is available in several critical regions. However, the accumulation of an oil-fuel mixture having the suitable properties for being ejected from the piston top land is a cumulative process over many cycles depending on the stochastic fluctuations of the flow field. Such a behaviour would have only been possible to simulate with a sophisticated large eddy (LES) description of the flow field and detailed modelling of the crevice volume. However, due to the computational costs, an LES-model was not regarded as practical for the reproduction of pre-ignition, as such an event was observed very rarely every 10,000 – 30,000 cycles. Therefore, the survey was restricted to the RANS formulation, which however, only allowed for a determination of ensemble averaged conditions.

To cope with the present modelling limitations, a methodology was applied, for which the argumentation for pre-ignition was effectively reversed. Droplets were first introduced through a user defined subroutine in the crevice regions with intensified wall wetting. Then the results at a representative pre-ignition timing were compared to experimental PI observations to verify the assumptions. [Figure 8.4](#) shows the specified droplet initial conditions and illustrates the positioning of the droplet initial velocity vector.

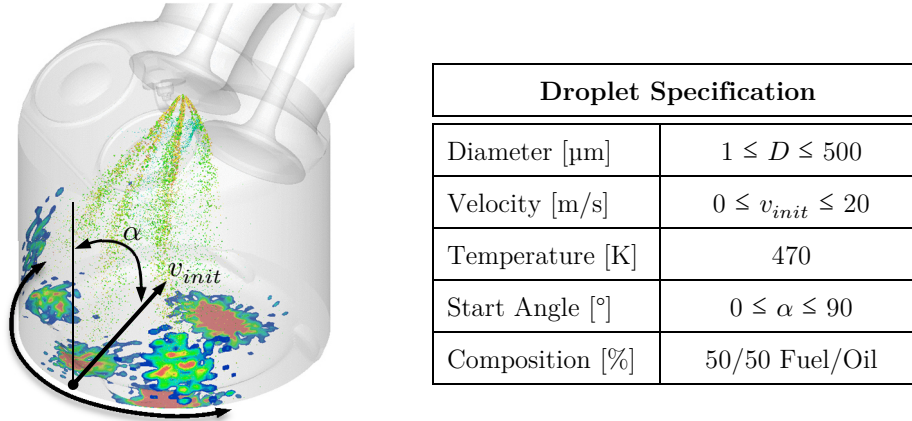


Figure 8.4: Initial properties of droplets inserted in the piston crevice region

To allow for a statistical evaluation from a single cycle, in total about 5000 droplets were introduced within one time step. The initial properties of each droplet were randomly defined within suitably chosen ranges to account for the stochastic behaviour of the droplet separation process. In this consideration, the maximum droplet velocity was estimated to be in the range of the mean piston speed ($\sim 20 \text{ m/s}$ at 2000 rpm). The temperature of droplets getting ejected from a liquid pool that is trapped between the cooled liner ($\sim 450 \text{ K}$) and the hotter piston ($\sim 520 \text{ K}$), was specified at a value of 470 K. Keeping the influence of droplet composition out of consideration until later, the droplets were assumed to have a balanced mixture composition of oil and fuel.

The lubricant that was run in the test engine was a SAE 5W-30 fully formulated passenger car engine oil (PCEO) on synthetic basis. In analogy to the multi-component fuel introduced in Section 6.3, the boiling behaviour of the oil was modelled by a number of five hydrocarbons with appropriate volatilities covering the entire boiling range of oil. [Table 8.1](#) gives an overview of the long-chain hydrocarbons ranging from C16 to C37 that were selected to obtain the high-temperature boiling range of lube oil.

Table 8.1: Definition of the multi-component engine lube oil model

Hydrocarbon species	Boiling point [K]	Mass fraction [-]
n-Hexadecane ($C_{16}H_{34}$)	560.15	0.02
n-Eicosane ($C_{20}H_{42}$)	616.75	0.25
n-Pentacosane ($C_{25}H_{52}$)	675.05	0.035
n-Heptacosane ($C_{27}H_{56}$)	715.15	0.6
n-Heptatriacontane ($C_{37}H_{76}$)	778.15	0.095

The measured boiling data of oil was adopted from [31], as a similar synthetic PCEO oil of comparable viscosity range was used in that study. [Figure 8.5](#) shows the measured and calculated boiling curves which are in good agreement for both oil and fuel. An almost parallel offset of about 300 K becomes obvious between the substances. The initial boiling point of the oil lies with about 600 K clearly above the typical wall temperatures of the liner and even the piston. Thus, boiling or intense evaporation from the lubricating film is rather unlikely under regular conditions.

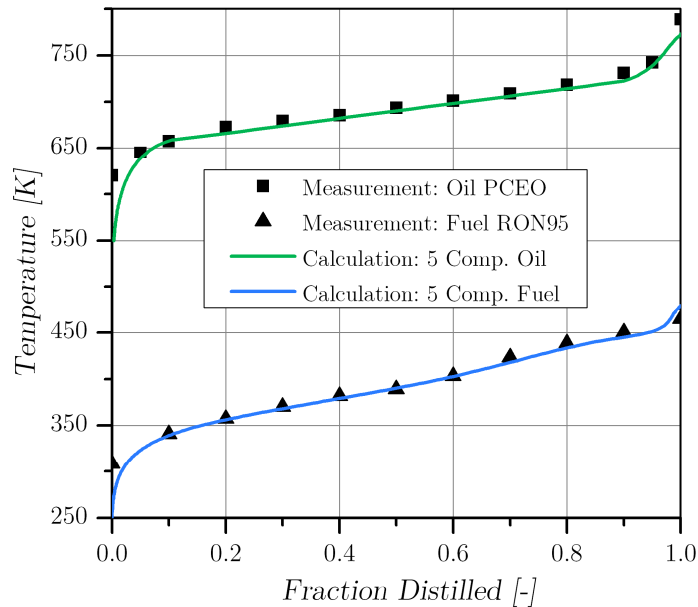


Figure 8.5: Comparison of measured and modelled boiling curves for the applied lube oil and fuel; Experimental data of the oil was adopted from [34]

Droplets were inserted evenly distributed around the circumference in a wall-near cell-layer next to critical piston crevice areas for fuel deposition, see [Figure 8.4](#). The resulting process of droplet

release, spreading into the charge and impingement resulting in the formation of wall film is illustrated as image sequence in [Figure 8.6](#).

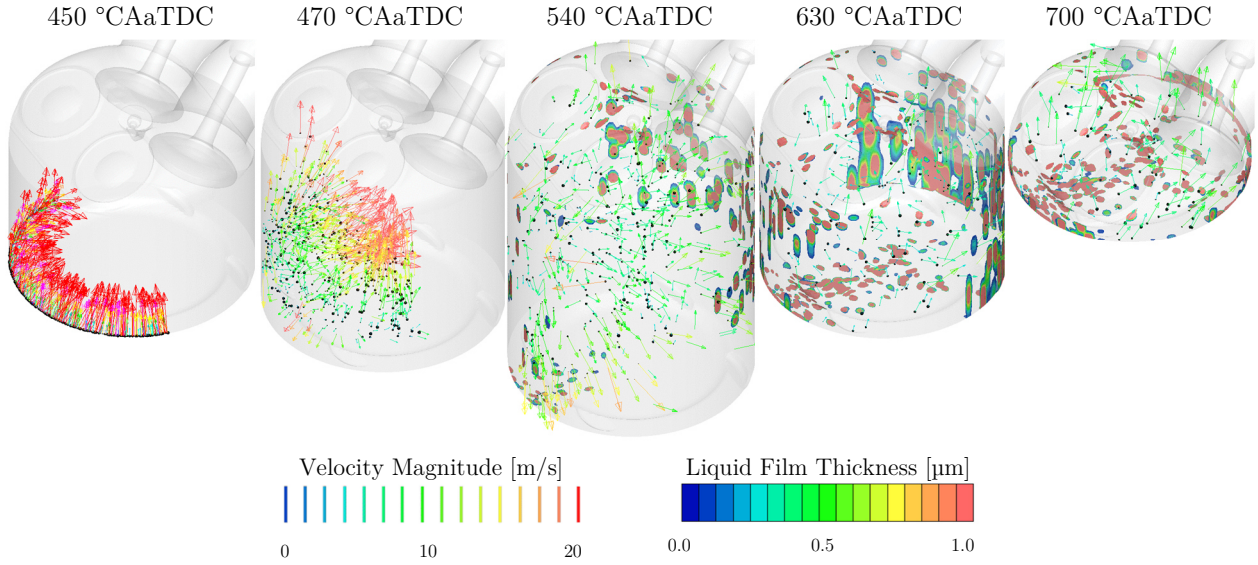


Figure 8.6: Spreading of inserted oil-fuel droplets (black dots and velocity vectors) and subsequently forming spots of wall film upon droplet-wall contact

It becomes obvious that a significant quantity of the droplets forms wall film upon wall contact. A quantitative evaluation of the droplet count depending on the diameter is given in [Figure 8.7](#). The total number of droplets at a potential PI timing at 700 °CAaTDC considerably decreased at about 80% compared to the initial count (blue results). This pronounced tendency for wall film formation is caused by the high boiling temperature of the oil. As the deposition limit scales with the boiling temperature (see Eq. (6.5) and [Figure 6.6](#)), all impingement events occur clearly in wetting regimes, even at the hottest surfaces like the valve disks. This has a strong effect on the number of critical droplets that can remain in the charge until compression end. As can be seen from the distribution at 700 °CAaTDC in [Figure 8.7](#), autoignition critical smaller droplets that evaporate rapidly in the hot compressed gas, have a distinctively low probability to act as a possible pre-ignition source. However, keeping in mind that autoignition was observed rarely approximately all 10,000–30,000 cycles at the test-bench, this low probability is in line with the experiments.

The result presented in [Figure 8.6](#) was generated assuming that the oil-fuel drops are released at 450 °CAaTDC. As was shown with 3D piston ring dynamic simulations in [21] at this timing, the piston ring acceleration of the top ring approaches a maximum at more than 2000 g, while a distinct back-flow exists through the top ring crevice. Although the severity of reverse blow-by decreases steadily with progressing intake stroke, further critical ring accelerations were observed around gas-exchange-BDC at 540 °CA and relatively late in the compression around 630 °CAaTDC. These three timings are therefore classified as the most critical moments for the separation of liquid and are concerned in the following. The afore-mentioned procedure of drop insertion was repeated for 540 and 630 °CAaTDC. Although one might assume that later insertion timings result in a shorter time available for impingement and hence a larger remaining droplet count around TDC, the simulations made clear that the drop number decreases to an almost similar extent as for early insertion, see green and orange results in left chart of [Figure 8.7](#).

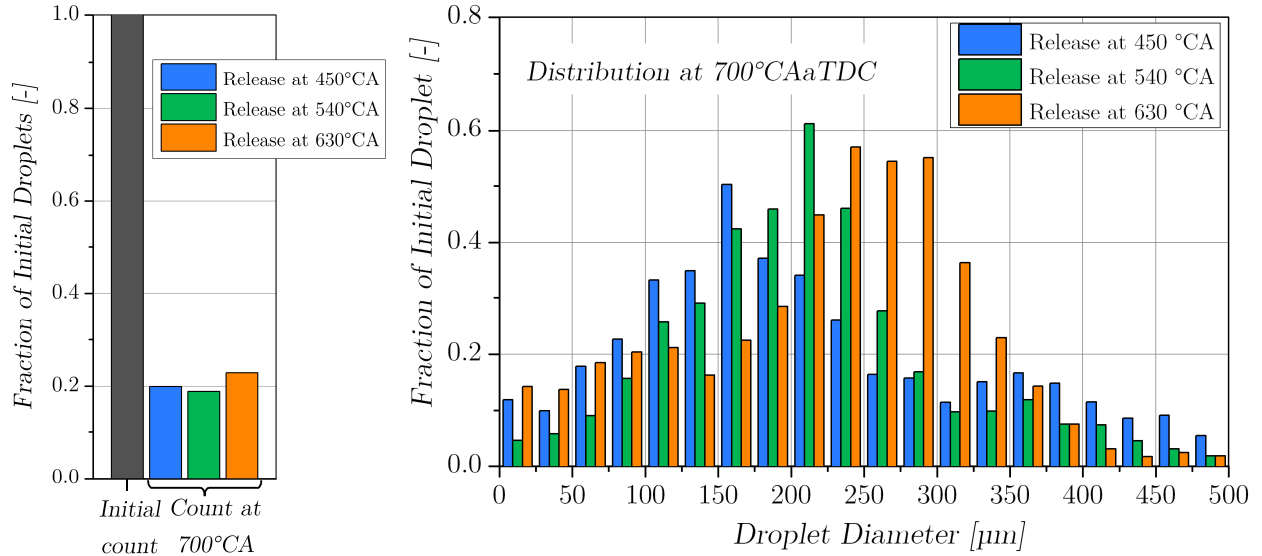


Figure 8.7: Left: Remaining fraction of oil-fuel droplets at a potential pre-ignition timing shortly before TDC (700 °CAaTDC) depending on insertion timing
 Right: Drop size distribution at 700 °CAaTDC depending on insertion timing

This can be explained by the larger number of drops colliding with the piston. For later insertion timings, the time for the piston to catch up the previously detached droplets gets shorter. Hence, only drops moving sufficiently fast towards the cylinder head can remain in the gas phase. Only large drops with comparably high momentum can maintain their velocity in the turbulent flow field. However, for too fast droplets, the risk of impingement on opposing walls increases. In contrast, small droplets that slow down rapidly are almost floating in the charge and are therefore most likely to be captured by the upward moving piston. Between these extremes, there exists a diameter range for which impingement is less probable, as can be seen by the occurrence of a maximum in the droplet diameter distribution in Figure 8.7. This maximum shifts to higher diameters for retarded insertion timings because less time is available for evaporation. Interestingly, the small scale droplets are moderately increasing what makes late separation processes even more critical for a potential occurrence of pre-ignition spots.

The dispersion and the dynamic motion of oil-fuel droplets were shown to be highly stochastic processes depending on the droplet initial properties as well as the turbulent flow field. In the next step, transient streamlines of critical drops remaining in the charge were evaluated and compared to the high-speed images of pre-ignition spots presented in Section 5.3, to find out any particularities of droplet motion. For each of the three conducted insertion timings, several streamlines were found to show similar endpoints in comparison to the recorded pre-ignition locations. However, especially for the drop insertion at 630 °CAaTDC, the origins of the droplets were in exceptionally good agreement with the areas of maximum crevice wetting. This is depicted in the images of [Figure 8.8](#) that show the cylinder volume from the same perspective as through the endoscope access. The recorded droplet ignition is depicted by a yellow symbol. Furthermore, the streamline endpoints of each image were set at the timing at which the subsequent pre-ignition occurred. The correlation with recorded pre-ignition locations and the agreement between streamline starting points and

crevice areas of maximum film thickness, suggest that an entrainment of oil-fuel droplets relatively late in the compression at 630 °CAaTDC is most likely to trigger pre-ignition.

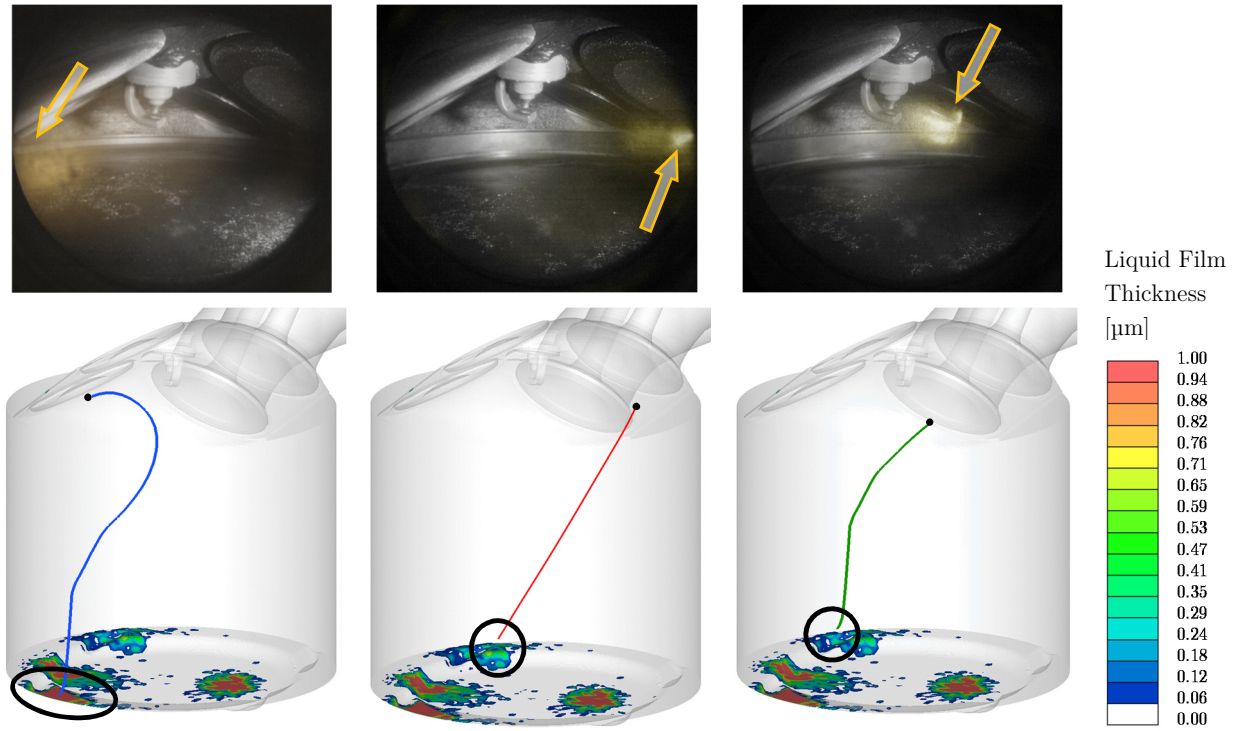


Figure 8.8: Trajectories of droplets (coloured lines) released at 630 °CAaTDC from wetted crevice areas in comparison with recorded origins of pre-ignitions (yellow arrows)

8.4. Validation of the Single Droplet Evaporation

For the case of droplet induced ignition, the vapour concentration in the environment close to the droplet's surface is the driving force. As described in Section 4.2, the ignition stages occur in a distance of several times the drop diameter away from the surface where critical mixture fractions of air and hydrocarbons are prevailing. Hence, the droplet gasification process in a hot environment will be studied in the following.

A droplet of initial diameter $D_0 = 250 \mu m$ was inserted in the centre of a cubic model of 10 mm edge length. Experiments on isolated droplets are typically carried out in an N_2 quiescent atmosphere under microgravity conditions as the spherical symmetry of the droplet is guaranteed. Therefore, zero gravity was also defined for validating the theoretical and numerical models as these usually suppose droplet symmetry. No gas velocity and no source term for momentum was considered. Hence, the evaporation process was driven only by diffusion ($Sh = 2$) and heat transfer without any convective influence ($Nu = 2$).

In a first step, the behaviour of n-heptane will be examined since it is one of the most extensively researched liquids in this field. This will then be complemented by results of the developed multi-component models for RON95 and PCEO oil. The specific heat and the thermal conductivity of the background fluid were defined as polynomial correlations directly from the *Star-CD* database. The molecular viscosity was obtained from the Sutherland equation. The gas phase properties of each hydrocarbon species was determined in a user coded subroutine: The temperature dependency of the latent heat was modelled with the enhanced Watson equation. The binary diffusion coefficients \mathfrak{D}_{12} were implemented as pressure and temperature dependent properties based on the work of Fuller [107]:

$$\mathfrak{D}_{12}(T_a, p_a) = 1.013 \cdot 10^{-3} \frac{T_a^{1.75} \sqrt{\frac{M_1 + M_2}{M_1 M_2}}}{p_a [(\sum v_1)^{1/3} + (\sum v_2)^{1/3}]^2} \quad (8.1)$$

The atomic diffusion volumes v_1 and v_2 were derived from tabulated values listed in [108].

In the following, model settings are validated with experiments from Nomura et al. [109] and Chauveau et al. [67]. Both studies are carried out on single droplets suspended on a support system exposed to hot ambient in a furnace. While Nomura used classical horizontal quartz fibres of 0.15 mm, Chauveau applied a new method where the droplet is suspended at the centre using a “cross-fibre” system of only 14 μm , see [Figure 8.9](#). The characteristic evaporation time predicted by Chauveau is typically two times longer compared to that determined by Nomura. Obviously, the results of Nomura are distinctively influenced by the heat conduction through the thicker support fibre and by the radiation of the internal walls of the furnace. Especially at high pressures and temperatures, where no measurements on a small-scale support fibre are available, the experiments have to be interpreted carefully when performing comparisons with numerical results.

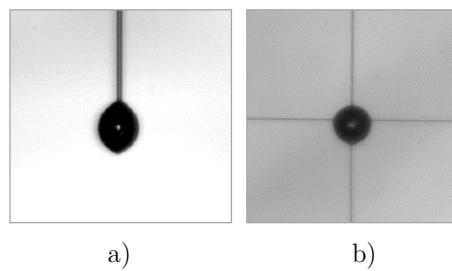


Figure 8.9: Droplet suspending techniques: a) classical fibre and b) cross-fibre, extracted from [67]

In [Figure 8.10](#) the influence of cell size on the temporal evolution of the non-dimensional droplet surface $(D/D_0)^2$ is analysed for an n-heptane droplet with an initial droplet temperature of 293 K. The ambient conditions are defined according to the configuration of Chauveau at a pressure of 1 bar and a gas temperature of 623 K. As can be seen, the droplet surface diminishes almost linearly during the gasification process what is termed as the “ D^2 -law” or “quasi-steady-model”. As becomes obvious from the right diagram in [Figure 8.10](#), after an initial heat-up period, the droplet temperature approaches a quasi-steady stage which is referred to as the adiabatic wet-bulb

temperature T_d^{wb} . This thermal state results from a balance between the latent heat of droplet vaporisation $h_{vap,d}$ and the heat transfer from the ambient gas to the droplet λ_a :

$$T_d^{wb} = T_a - \frac{\dot{m}_d(p_{sat}(T_d^{wb})) \cdot h_{vap,d}}{\lambda_a} \quad (8.2)$$

A comparison of the numerical results in Figure 8.10 reveals a strong influence of different cell sizes on the surface diminishing rate as well as on the droplet temperature. A coarse cell size that is one order of magnitude larger than the drop ($D_0 = 0.5$ mm) has a similar accelerating effect on evaporation (red line) as the classical droplet suspending technique from Nomura et al. [109] (open symbols).

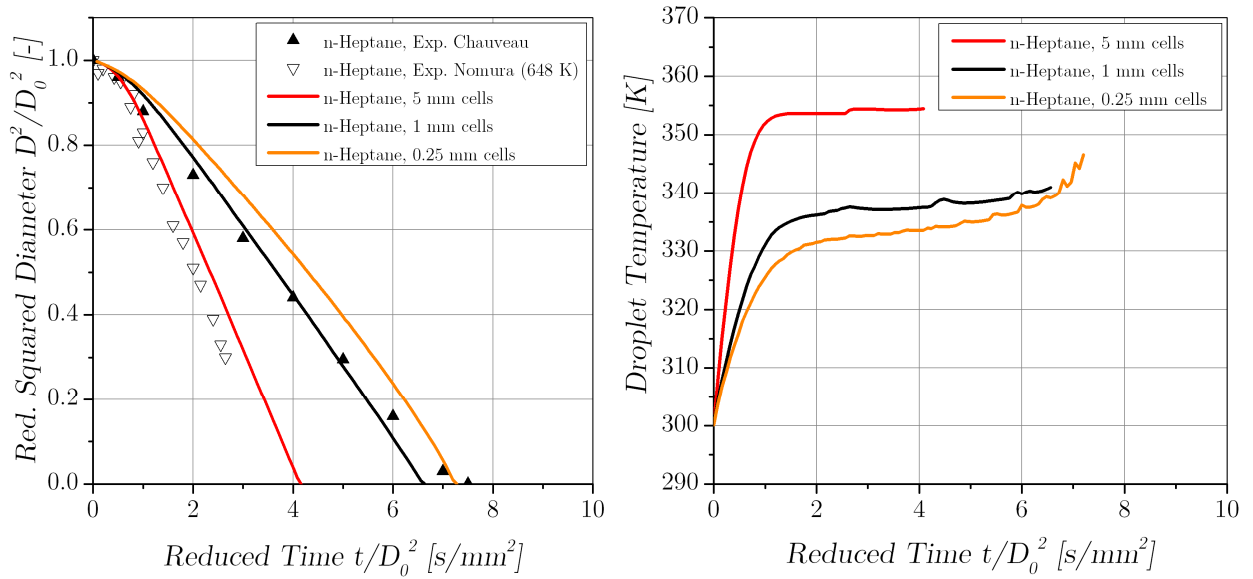


Figure 8.10: Diffusive influence of the cell size on the vaporization histories of single n-heptane droplets with $D_0 = 0.5$ mm at $p_a = 1$ bar, $T_a = 623$ K compared to measurements from Chauveau et al. [67] and Nomura et al. [109]

In contrast, for cell sizes that are smaller than the droplet diameter (orange line), additional numerical effects are superimposing the D^2 -law leading to a more progressive decrease of the surface compared to the measurement. The evolution of the droplet temperature makes clear that a quasi-steady equilibrium at the wet bulb temperature cannot be reached for small cell sizes. Interestingly, although evaporative cooling is weaker due to the slower evaporation process, the droplet temperature is the lowest compared to the other results. Looking at Eq. (8.2) an explanation can be found in the temperature dependency of the thermal conductivity of the gas λ_a . The smaller the cells in proximity to the droplet the more effectively is their cooling during the initial phase. A cooler boundary layer consequently impedes heat conduction to the droplet as the thermal conductivity decreases for lower gas temperatures. Towards the end of the process, heat exchange in the surrounding increasingly balances the initial cooling and droplet heat up and evaporation gets intensified rapidly. However, this numerical deviations are taken into account as such small scales occur only for a limited number of cells in the quenching areas around TDC. The vast majority of

the cylinder cells typically has a length of 1 mm. For this dimension, the simulations delivered the best correlation with the measurements of Chauveau et al. [67]. This was additionally validated over the relevant temperature range for in-cylinder considerations, see Figure 8.11. As can be seen, the wet bulb temperatures remain well below the boiling temperature of n-heptane (372 K) even for high gas temperatures. A measurement of wet bulb temperatures was carried out by Yuen & Chen [110]. An interpolation of these results to the gas conditions of Chauveau et al. [67] is depicted as symbols in the right diagram of Figure 8.11. A certain deviation of the simulations may arise from the different experimental setup as Yuen & Chen investigated on freely falling droplets. Therefore, the experimental data is only conditionally comparable to the results at hand. However, the relative offset within the measurement series shows the similar tendency. Finally, due to the appropriate agreement between simulations and experiments, the current model setup allows for a detailed analysis of the gasification process of single droplets.

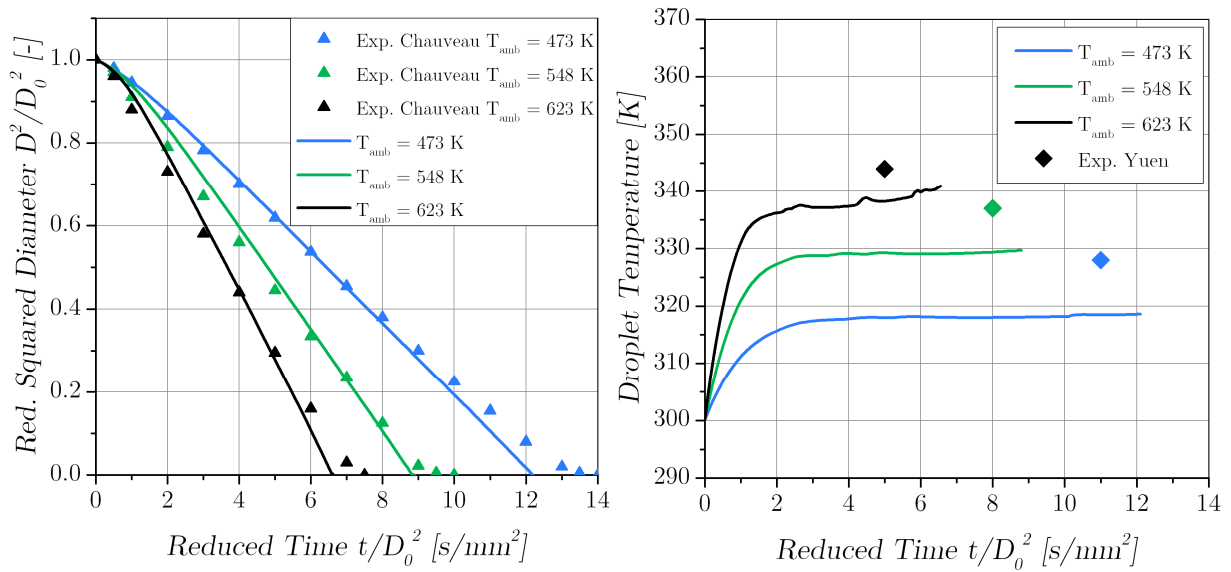


Figure 8.11: Vaporization histories of single n-heptane droplets at $p_a = 1$ bar for different ambient temperatures compared to measurements from Chauveau et al. [67] and Yuen & Chen [110]

Comprehensive single droplet evaporation experiments on PCEO oil or even RON95 are not available at present. Therefore, the behaviour of multi-component droplets in hot environment will be discussed in relation to the validated results of n-heptane.

Nomura et al. [109] carried out high-pressure experiments with n-heptane droplets under engine-relevant conditions at $p_a = 20$ bar and $T_a = 656$ K which occur approximately at a crank angle of 690° in the operating point treated in the study at hand. At this timing, the first pre-ignition reactions are likely to be initiated, whereby it can be regarded as the critical evaporation region for oil-fuel droplets. Figure 8.12 compares the single droplet simulations of n-heptane, RON95 and PCEO oil with regard to the surface diminishing rate and the droplet temperature. As was to be expected because of the argued influence from the droplet support fibre used by Nomura, the calculated diminishing rate of n-heptane is slightly delayed compared to the experiment. The relatively cold droplet with an initial temperature of 300 K experiences a strong heat-up in the hot

environment. In the experiment this becomes obvious in an initial thermal growth of the drop volume beyond $(D/D_0)^2 = 1$ that overcompensates the evaporative losses. This behaviour was actually not captured by the material properties defined in *Star-CD*. However, the heat-up effect is probably less pronounced for already hot droplets separated from combustion chamber walls and was therefore neglected.

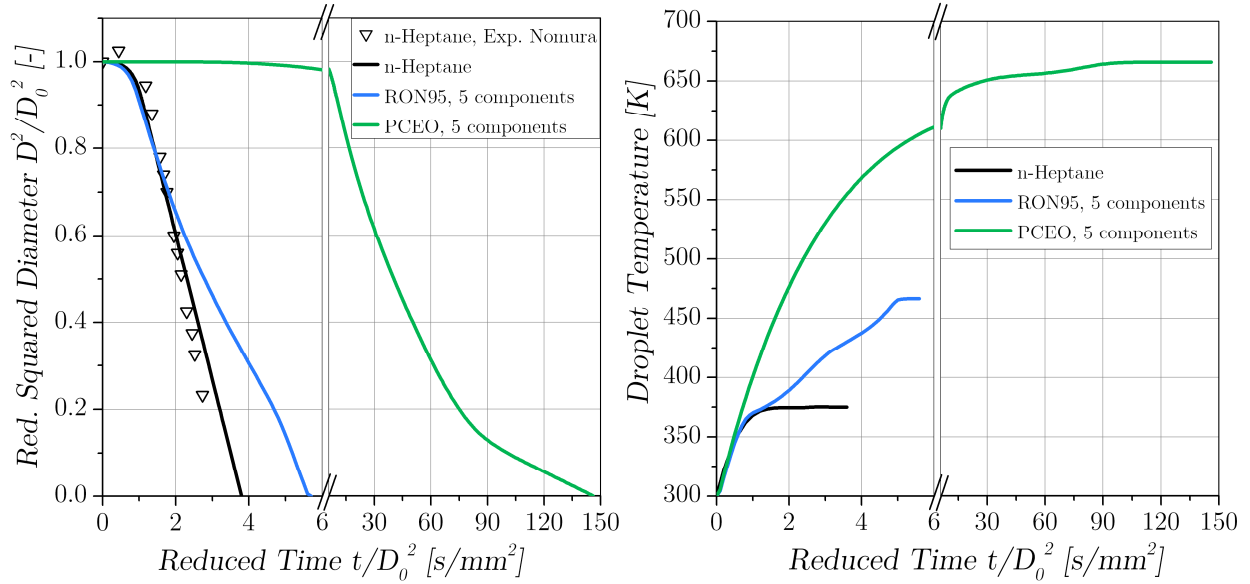


Figure 8.12: Comparison of the vaporisation behaviour between single droplets of n-heptane, RON95 fuel and PCEO oil at $p_a = 20$ bar and $T_a = 669$ K

A comparison between n-heptane and fuel in Figure 8.12 makes clear, that the time until the droplet has evaporated completely, is about 50 % longer for RON95 compared to neat n-heptane. Moreover, for a multi-component mixture the D^2 -law is not valid anymore. As the composition of the droplet and hence the saturation pressure changes continuously, no equilibrium condition is reached at the wet bulb temperature.

For a better understanding, in [Figure 8.13](#) the vapour mass flow rates of fuel and oil are shown separately for each model component. For RON95 it becomes obvious that the evaporation of the light-end component isopentane C_5H_{12} is excessively high during the early period. This is the reason why the gasoline drop diminishes slightly faster in the beginning compared to higher boiling n-heptane. In the middle boiling range of gasoline, the evaporation rate decreases temporarily and the droplet heat-up gets effectively determined by the highest-boiling components. Only in the last stage of evaporation when all components but n-tridecane $C_{13}H_{28}$ are distilled, a quasi-steady drop temperature can be stated, shortly before the liquid has fully vaporised. Considering the different scaling of both axes in the right diagram of Figure 8.13 a distinctively different behaviour can be found for the case of multi-component PCEO oil. The droplet evaporation process extends over a significantly longer period with moderate evaporation rates which are approximately one order of magnitude lower compared to RON95. Already the light-end constituent of the oil model n-hexadecane $C_{16}H_{34}$ requires a droplet temperature beyond 600 K at the desired ambient pressure of 20 bar to vaporize notably. Further, the evaporation is dominated by the two components n-eicosane $C_{20}H_{42}$ and n-heptacosane $C_{27}H_{56}$ according to their disproportionately high initial droplet

mass fractions, which were defined in Table 8.1 to represent the relatively flat boiling curve of PCEO oil, shown in Figure 8.5.

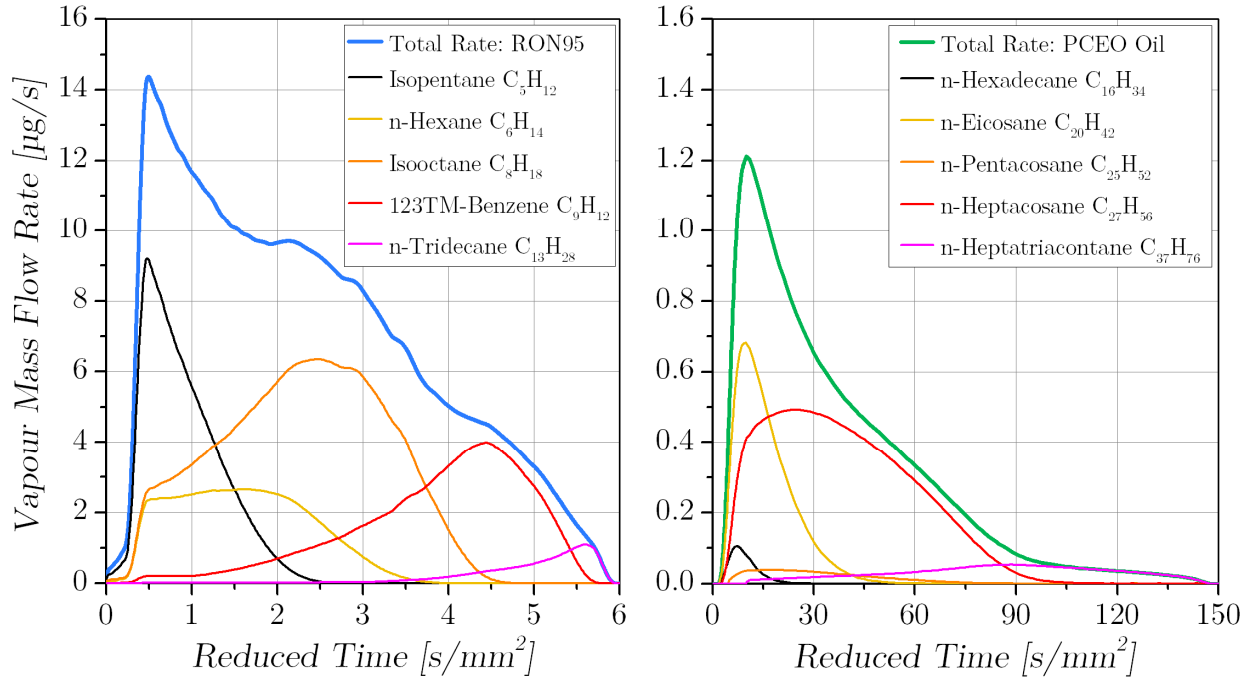


Figure 8.13: Droplet vaporization histories of the five individual model components resulting in the total droplet vapour mass flow for fuel (left) and oil (right) ($D_0 = 100 \mu\text{m}$, $p_a = 20 \text{ bar}$ and $T_a = 669 \text{ K}$)

Comparing the data of fuel and oil in Figure 8.12 and Figure 8.13 it becomes obvious that the fuel has almost vanished completely when the oil starts to evaporate. Therefore it might be incorrectly assumed that the evaporation of both liquids would proceed independently. However, fuel and oil were not mixed in the above considerations and interactions between the liquids were not taken into account. The impact of the fuel-oil mixture ratio on droplet evaporation will be studied in the following under the assumption of ideal liquids.

Slight, medium and heavy dilution of a fuel droplet will be captured by oil mass fractions of 10 %, 50 % and 90%, respectively. Due to the fact that the volatility of both liquids differs strongly, an addition of already lowest portions significantly changes the properties of the initial liquid. As shown in the left diagram of [Figure 8.14](#), an addition of 10 % oil to the fuel increases the droplet lifetime by a factor of 5. Conversely, an oil-droplet evaporates about 30% faster when diluted with 10% fuel. The composition of the ten droplet components changes continuously depending on their initial fractions and their volatilities. Thus, an equilibrium condition is not reached during the process, as can be seen by the strongly varying temperature gradients in the right chart of Figure 8.14. The droplet temperature adjusts in order for the energy and mass balance to be satisfied and experiences heating or cooling. A higher dilution with more volatile fuel leads to a stronger initial cooling but as the drop mass decreases and the drop surface to volume ratio increases, the remaining oil can be heated up rapidly by the hot ambient gas.

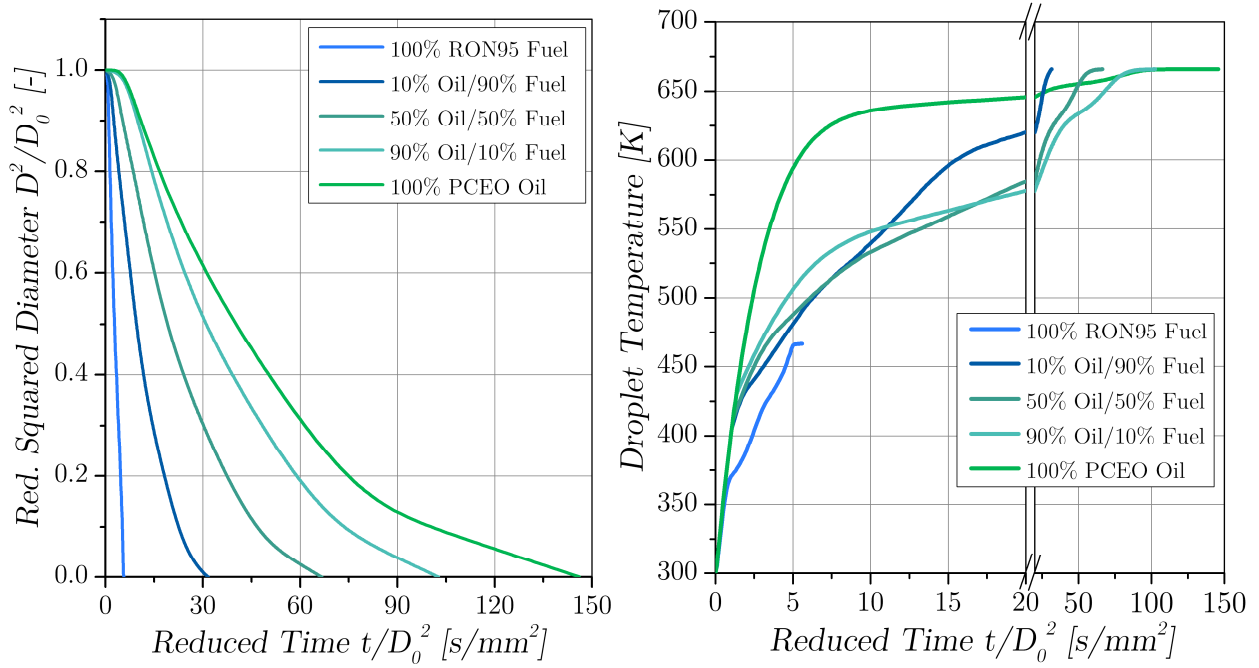


Figure 8.14: Impact of the oil-fuel mixture ratio on the droplet surface reduction rate (left) and on the droplet temperature (right) shown at $p_a = 20$ bar and $T_a = 669$ K

For higher oil contents, the initial heating of the droplet is more effective and the necessary temperature for the evaporation of the light-end oil components is reached faster. However, the heat-up process gets then increasingly balanced by the latent heat required to vaporise the remaining oil components. Thus, the temperature gradient decreases notably when the medium boiling range of the oil is reached and the main components with high initial mass fractions are vaporised.

The oil and fuel vapour mass flow rates corresponding to the results presented in Figure 8.14 are shown in [Figure 8.15](#). It should be noted that the oil vapour results are scaled by a factor of 10 to provide a better comparability with the fuel vapour results. Interestingly, although the droplet temperatures were shown to be strongly influenced by the instantaneous droplet compositions, the timings of the maximum vapour mass flow rates of fuel and oil remain almost unaffected. In contrast, the maximum values themselves decrease in a similar manner as the droplet lifetime: A dilution with 10 % fuel decreases the maximum oil vapour mass flow rate at about 30 %. For droplets that are released from the piston crevice, this means, that a higher dilution with fuel substantially decreases the risk of high local oil vapour concentrations. Additionally, a higher fuel content keeps the droplet temperature on a lower level during the early phase what slightly retards the evaporation of the oil. The later the oil vapour is exposed to the hot cylinder charge, the lower the probability for autoignition reactions to be finished and to initiate pre-ignition.

Furthermore, it is quite a remarkable result that although the complete evaporation of oil extends over a relatively long period, the maximum oil vapour mass flow occurs already very early in the process. This is of significant importance with respect to pre-ignition, because a local critical amount of oil vapour can be expected to exist already after a very short exposure time. The results from Figure 8.15 allow a rough estimation of the maximum oil vapour fraction to occur at approximately two times the lifetime of a pure fuel droplet of the same size.

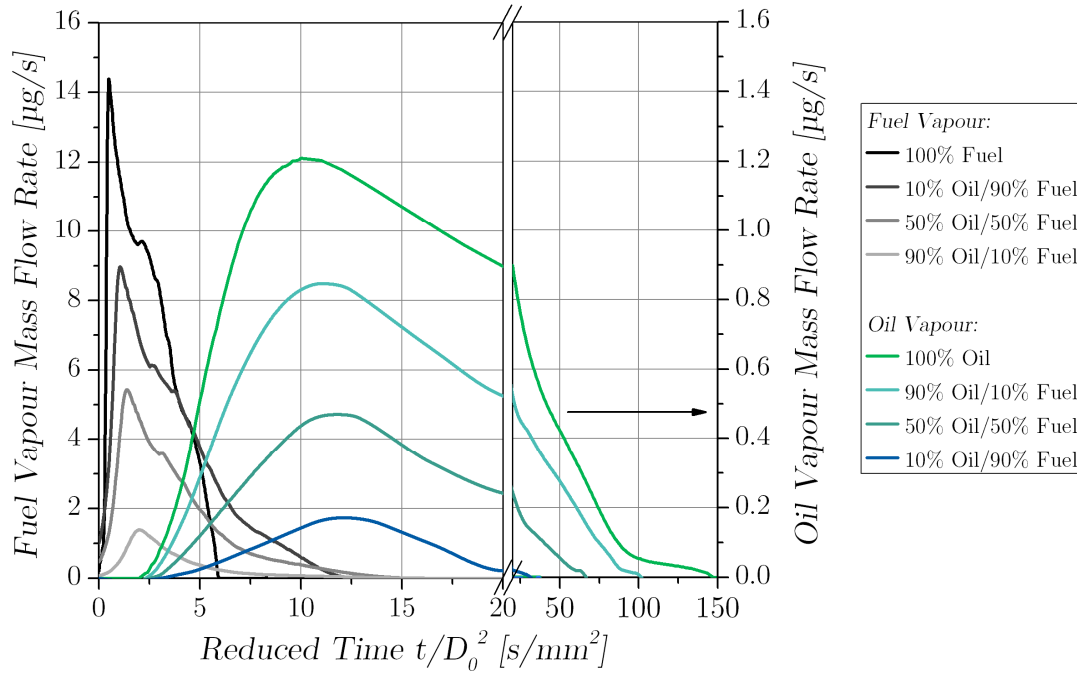


Figure 8.15: Vapour mass flow rates of fuel and oil shown for different oil-fuel mixture ratios of the droplet ($D_0 = 100 \mu\text{m}$, $p_a = 20 \text{ bar}$ and $T_a = 669 \text{ K}$)

For the single droplet investigations, any convective influence caused by the gas flow or the droplet movement was excluded. Hence, in the following section, oil droplet ignition experiments will be recalculated with CFD and reaction kinetics simulations to gain more practical results. Both simulation methods are combined to establish the connection between a certain oil vapour concentration originating from the droplet and the resulting autoignition tendency.

8.5. Determination of the Oil Reactivity

The presence of lubricant inside the combustion chamber was shown in several experimental studies to have a substantial accelerating effect on the ignition delay time [32,33,34,35]. However, these works have in common, that relevant properties of the lubricant droplets like the initial size, the detailed positioning or the release timing were not to be specified in detail. For example in [32] a liquid pool of oil was placed on the piston of the RCM which obviously dispersed randomly as droplets during compression. The ignition delay measurements for different oils are shown in the left chart of [Figure 8.16](#).

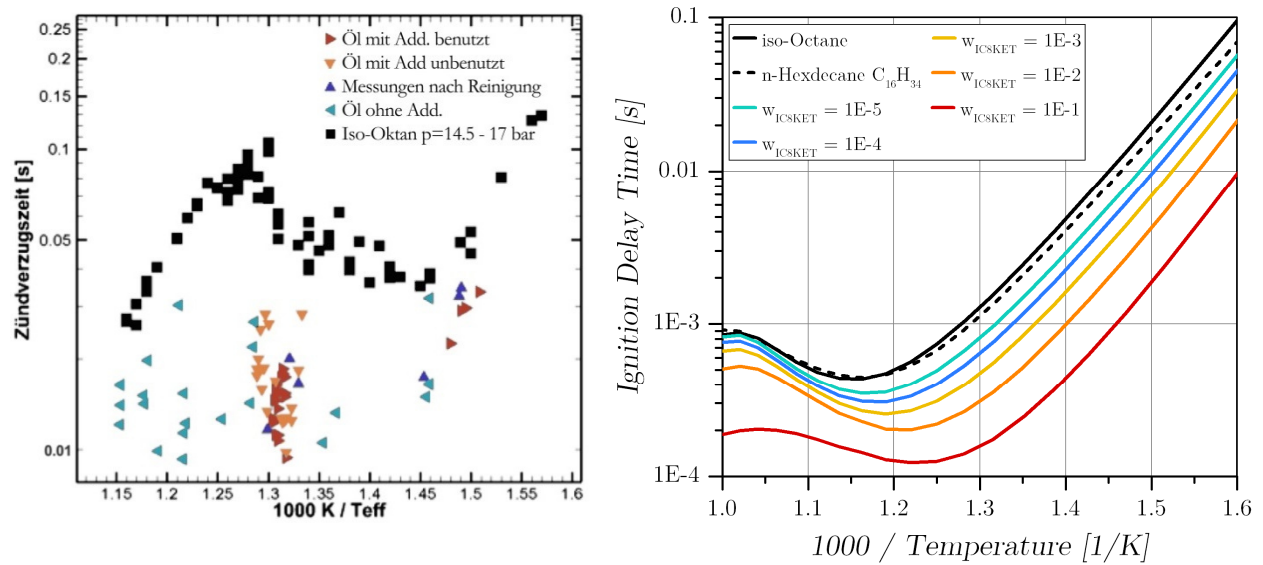


Figure 8.16: *left:* RCM measurements of autoignition delay times for stoichiometric iso-octane mixtures between 14.5 -17 bar and with addition of lubricating oil, from Palaveev et al. [32]
right: Ignition delay study of stoichiometric n-alkane mixtures and different seeding levels of octylketohydroperoxide carried out in a homogeneous reactor model at 40 bar

It should be noted, that there exists a strong fluctuation of the measured ignition delay times during oil addition. This seems to confirm that the autoignition of the applied oil occurred as a stochastic phenomenon depending on the size, the spatial distribution and hence the evaporation behaviour of the separated droplets. Nevertheless, an ignition delay time up to one order of magnitude shorter compared to iso-octane was observed independently on the inserted oil type.

To validate this accelerating influence from a chemical point of view, reaction kinetics simulations were carried out in a homogeneous reactor model. In analogy to the RCM experiment, iso-octane, represented by the mechanism discussed in Section 7.1, was compared to an oil surrogate. For that reason, a reaction mechanism was used from the Lawrence Livermore National Laboratory covering a wide range of long-chain n-alkanes up to C16 [47] which are typical constituents of engine oils. Comparing iso-octane and n-hexadecane, which is the largest available species in the mechanism, an accelerating effect under engine relevant conditions at 40 bar can hardly be ascertained, see black

lines in right chart of Figure 8.16. According to Westbrook et al. [47], the ignition delay times of long-chain n-alkanes are generally of the same order. It is argued that solely n-alkanes cannot be responsible for the observed early pre-ignition timings shown in Figure 5.1 on page 40. Consequently, somewhat more reactive components included in the oil or oil-additives are supposed to accelerate the oil chemistry what is also confirmed by investigations in [32].

One group of species that is produced in the low temperature oxidation regime of hydrocarbons was identified in [48] and [111] to be highly reactive even in very low quantities. These so called ketohydroperoxides are intermediates that are formed through isomerisation between 620 K and 720 K. Moreover, in [48], ketohydroperoxides were obtained with a CFR engine that was run under conditions close to autoignition but without combustion. At this pre-oxidised state, the mixture was then cooled down resulting in a certain content of long term stable ketohydroperoxides. If this mixture was successively used as fuel additive, a considerable reduction of the ignition limit was found. This leads to two possible assumptions for droplet ignition: The first is, that the promoting effect of lubricating oil is due to reactive components in the chemical composition itself. The second is, that in regions with intensified fuel impingement, especially the liner and crevice, partially burned fuel containing ketohydroperoxides accumulates and is then released as droplets.

To demonstrate the impact of reactive components, the reactor was seeded with octylketohydroperoxide, which is a stable intermediate forming during the low temperature oxidation process of iso-octane (see also Section 4.1.1). As can be seen from Figure 8.16, already extremely low mass fractions of octylketohydroperoxide w_{IC8KET} in the range of $1.0E-6 - 1.0E-5$ showed significantly faster pre-reactions leading to autoignition than n-hexadecane.

In order to gain reliable statements about the reactivity of oil it is essential to study the behaviour of single oil droplets. As pre-ignition is a very topical issue and until now the autoignition of lubricating oils was not of great relevance in practical engine or combustion considerations, experimental studies are barely available on this topic. Ohtomo et al. [37] were the first who recently carried out high-speed imaging in an RCM to capture the autoignition process triggered by a well-defined falling oil droplet. A special injection device was utilized to control the diameter and temperature of the inserted single drop. The resulting recordings shown in the top row of Figure 8.17 make clear that the ignition occurred in the oil vapour plume far behind the falling droplet.

In the following, this experiment serves as reference to determine the critical oil vapour mass fraction for autoignition. For this reason, the evaporation of the oil drop in the RCM experiment was recalculated with the CFD method using the multicomponent oil model presented in the previous sections. The results can be seen in the bottom row of Figure 8.17. To visualize the general presence of oil, a blue isosurface is plotted for a vapour fraction w_{oil} of $1.0E-3$. An additional red isosurface at $w_{oil} = 1.0E-2$ should emphasise the strong initial gasification process of the drop. The droplet that was pre-heated in the injection device ($T_{D0} = 610$ K) immediately experienced cooling due to evaporative heat losses and the cool charge itself prevailing at compression start ($t = 0$ ms). Hence, the gasification rate was the highest at the beginning and decreased as the droplet further moved downwards. However, as can be seen from the image at 25.6 ms an ignition kernel formed in a certain distance to the wall and not at topmost position of the combustion chamber. This is explained by local disturbances of the flow field generated by the motion of an actuator closing the communication path to the injection device immediately after drop insertion. Additionally, heat

losses through the walls are to be expected to delay or even inhibit the development of an ignition kernel in close proximity to the wall.

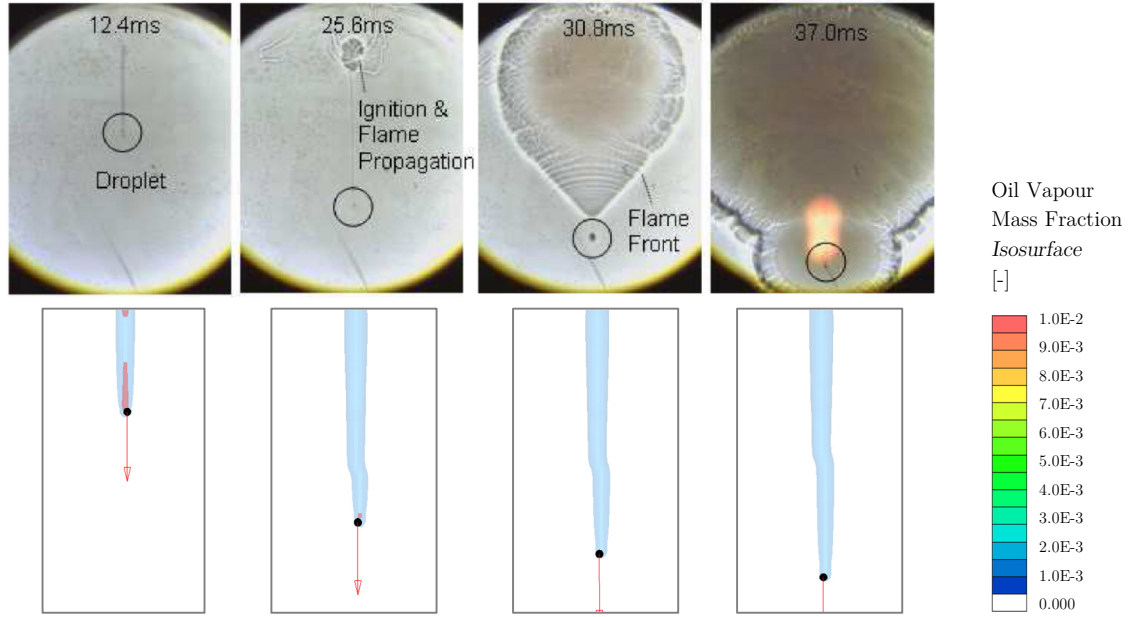


Figure 8.17: RCM free fall experiment of a single oil droplet with $D_0 = 410 \mu\text{m}$ and $T_{D0} = 610 \text{ K}$ injected under stoichiometric conditions, reprinted from [37] (top row); Associated results of the oil vapour distribution recalculated with CFD (bottom row)

For the determination of a critical oil vapour mass fraction, a cubic control volume was positioned according to the observed ignition kernel at a distance of about 10 mm to the upper wall, see left illustration in [Figure 8.18](#). The temporal evolution of the maximum oil vapour mass fraction that arose within this volume is plotted in the right chart of [Figure 8.18](#). The red line corresponds to the high drop temperature of 610 K that was adjusted in the experiment shown in [Figure 8.17](#).

Additional measurements with lower drop temperatures were also carried out in [37] to investigate the limit for autoignition in more detail. Vapour ignition was apparent down to an obviously minimum necessary drop temperature of 560 K. The associated calculated evolution of the vapour fraction, plotted as orange line, can therefore be regarded to represent the autoignition limit. As can be seen from [Figure 8.18](#), when the drop entered the control volume at about 7 ms, the fraction of oil vapour increased abruptly to values beyond 0.1. This was caused by the high vapour fractions emerging in closest proximity to the drop surface. Autoignition was, however, detected after the ignition delay time has elapsed, at about 31 ms (marked by symbol). No vapour ignition was observed for a droplet with 520 K (green line) because obviously the gasification process was too weak for generating sufficiently high local oil concentrations.

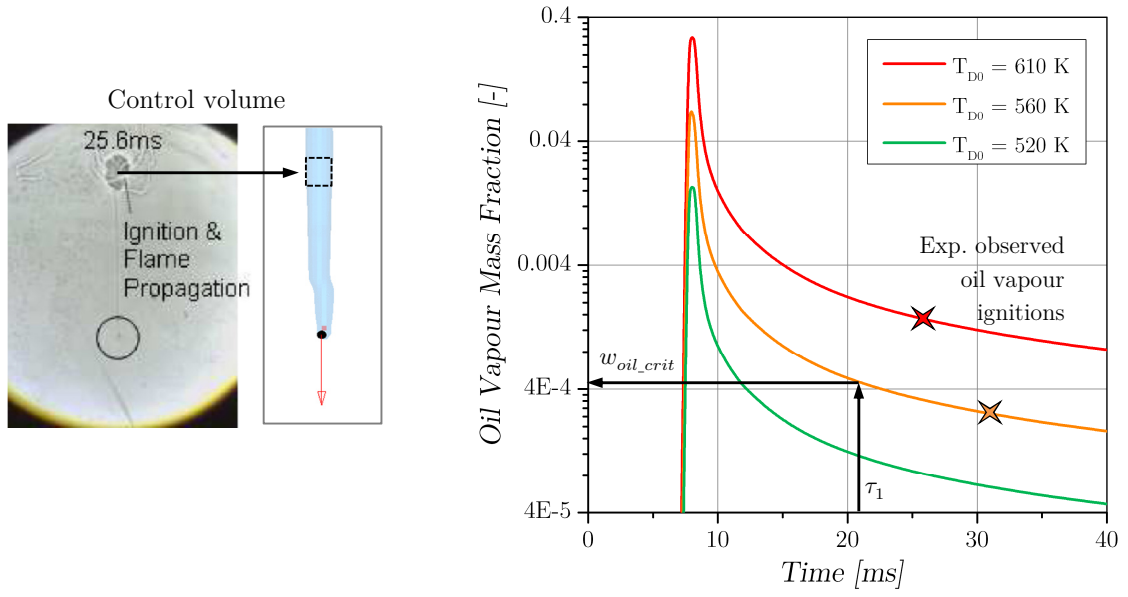


Figure 8.18: Evolution of the maximum oil vapour mass fraction monitored in a control volume defined at the observed location of vapour ignition

The strongly diminishing vapour fraction shown in Figure 8.18, indicates that high local oil fractions get rapidly balanced by molecular diffusion. Hence, the occurrence of first pre-reactions is not only dependent on the transient pressure and temperature during compression but additionally on the available oil fraction at the ignition spot. To study the impact of different oil vapour fractions on autoignition timing, the RCM experiment was recalculated with reaction kinetic simulations. For this purpose, the stoichiometric air-fuel mixture was seeded with octylketohydroperoxide to mimic the reactive influence of oil vapour. The fraction of the reactive species was adjusted in order to reproduce the autoignition timings from the experiment and can be taken from Figure 8.19.

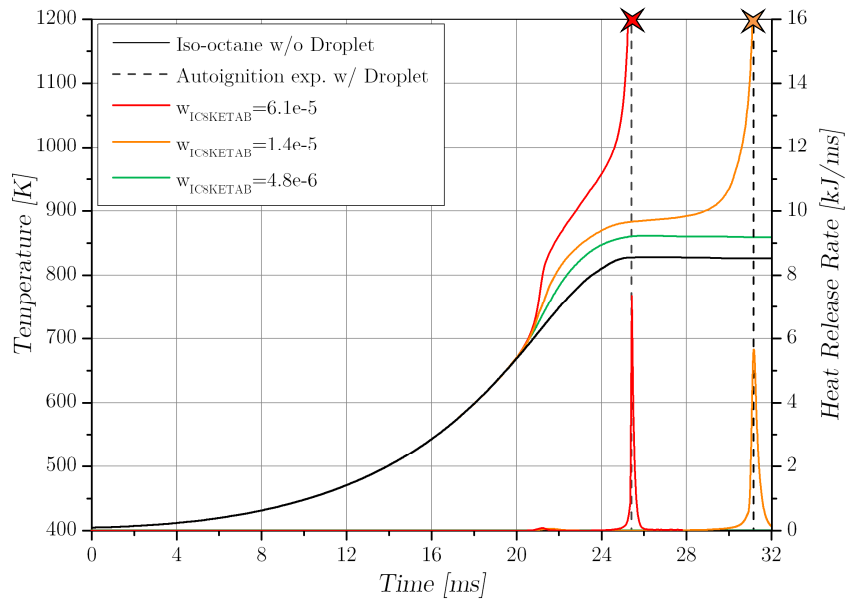


Figure 8.19: Recalculation of the experimentally observed oil vapour ignitions with different seeding levels of reactive octylketohydroperoxide added to the stoichiometric reactor volume

Remarkably, the first stage of ignition occurred independently on the radical seeding level, after an induction time of 21 ms. At this timing, a charge temperature around 690 K was reached and exothermal chain branching pre-reactions were strong enough leading over to the intermediate oxidation regime. Therefore, it was considered as a representative timing for evaluating the critical threshold for oil vapour ignition. As depicted in Figure 8.18, for the droplet with 560 K at 21 ms the critical oil vapour mass fraction w_{oil_crit} could be determined at about 4.5E-4. For the 40 K hotter droplet, the oil vapour fraction at the ignition spot increased about 4.4-fold. This trend agrees well with the approximately 4.5 times higher ignition probability measured for the hotter droplet in [37]. Obviously, for higher local vapour fractions the impact of dilution due to diffusion and convection is less significant what raises the potential risk of autoignition.

After the first stage of ignition, it can be observed that the vapour fraction further falls off. This may indicate that the radicals from the oil formed during the first stage of ignition further react more likely with the vast amount of fuel molecules available in the background fluid. Thus, the fraction of oil vapour is probably decisive for preparing the first stage of ignition but is obviously less significant for the final hot ignition. This is also confirmed by the falling drop RCM experiments in [37] since the autoignition timing was observed slightly delayed when the drop was introduced into pure air under equal thermodynamic boundary conditions. Apparently, the second stage of ignition was retarded due to the lack of hydrocarbons available at the ignition spot. Rich mixtures were, however, not studied, but it is known from the test bench that a possibly higher reactivity will certainly be overcompensated by the enhanced evaporative cooling effect. However, for the investigations at hand, it was of special interest to analyse the higher PI tendency arising from a fuel-efficient stoichiometric combustion, for which, the higher resulting mixture temperature is known to be the fundamental requirement for autoignition reactions.

Comparing the critical oil vapour fractions from Figure 8.18 with the fractions of ketohydroperoxide from Figure 8.19, it is evident that there exists a direct relationship between the quantities. Independently on the drop temperature, the mass fraction of the reactive species was found to be linked to the local oil mass fraction by a constant factor:

$$w_{oil} \approx 32.5 \cdot w_{IC8KETAB} \quad (8.3)$$

This relationship allows a simple approximation of the oil chemistry without the requirement of detailed chemical data about the composition of the oil and additives. Especially, information about the latter may be difficult to obtain from the manufacturer but has a distinctive influence on autoignition. Furthermore, the chemical impact of organometallic substances such as additives on the oxidation of long-chain hydrocarbons has not yet been sufficiently understood and is therefore not available in current reaction mechanisms. The method to capture the reactivity of oil with radical species is therefore a practical approach. However, it should be noted that the factor determined in Eq. (8.3) is expected to depend on the oil type and is therefore restricted to the PCEO oil that is used in the study at hand.

8.6. Modelling of the Oil Droplet induced Pre-Ignition Process

In the previous sections, a considerable effort was invested to validate the evaporation and autoignition behaviour of oil under defined test conditions. In the following, CFD and reaction kinetic simulations are carried out for a PI-critical operating point according to the full-engine test bed. In this way the causality of pre-ignition emerging from separated droplets will be further clarified.

8.6.1. Critical Oil Vapour Fraction for Pre-Ignition

The single oil drop experiments and simulations suggest that sufficiently high initial drop temperatures beyond 500 K are mandatory for oil vapour ignition in an RCM. For in-cylinder considerations, however, oil drops can be expected to be dominated by the wall temperature of the liner, which is well below 500 K. In contrast to the discussed RCM, typical SI engines showing PIs, employ distinctly higher compression ratios in combination with turbocharging. The final compression pressure of the operating point treated in the study at hand (see Table 5.1 on page 39) is with 47 bar about 2.5 times higher compared to that of the RCM with 19 bar. As shown by Figure 4.2 on page 23, autoignition reactions of hydrocarbons are substantially faster at elevated pressures. It can therefore be concluded that under real-engine conditions already lower oil fractions, compared to the RCM case, are sufficient to initiate a premature ignition. Consequently, the evaporation and ignition behaviour of separated oil droplets inside the combustion chamber will be treated in the following.

In order to analyse the necessary oil reactivity for pre-ignition under the high-pressure conditions prevailing in a downsized engine, chemical kinetic simulations were carried out in a stochastic reactor model. The direct injection sub-model was adjusted to introduce a single oil droplet into one stochastic reactor particle. In analogy to the investigations on the reactivity of a single fuel droplet in Section 7.4, a crank angle of -80°CAaTDC was estimated to inject the droplet. During compression, the droplet continuously evaporated and increased the concentration of the reactor subvolume containing the drop. The droplet evaporation rate was adjusted to provide the highest vapour fraction in the reactor particle sufficiently in advance to TDC to fully account for the impact of low-temperature pre-reactions on autoignition. As was explained in the previous section, the injected droplet was seeded with the radical species octylketohydroperoxide to mimic the reactivity of oil.

In the left diagram of [Figure 8.20](#) cylinder pressure and heat release rate are depicted for a pre-igniting cycle caused by an injected oil droplet. Immediately after autoignition, a predictive spark ignition model was invoked to calculate the remaining heat release. The correlation with the measured cylinder pressure reveals that the flame initially propagates identical as from a regular spark followed by a super-knocking combustion with an immediate heat release. The right diagram in Figure 8.20 shows the associated temperature history of all stochastic particles. The red line

stands for the particle that contains the injected droplet. The progressive rise in temperature due to pre-reactions that heated up the particle, set in just 5°CA before autoignition.

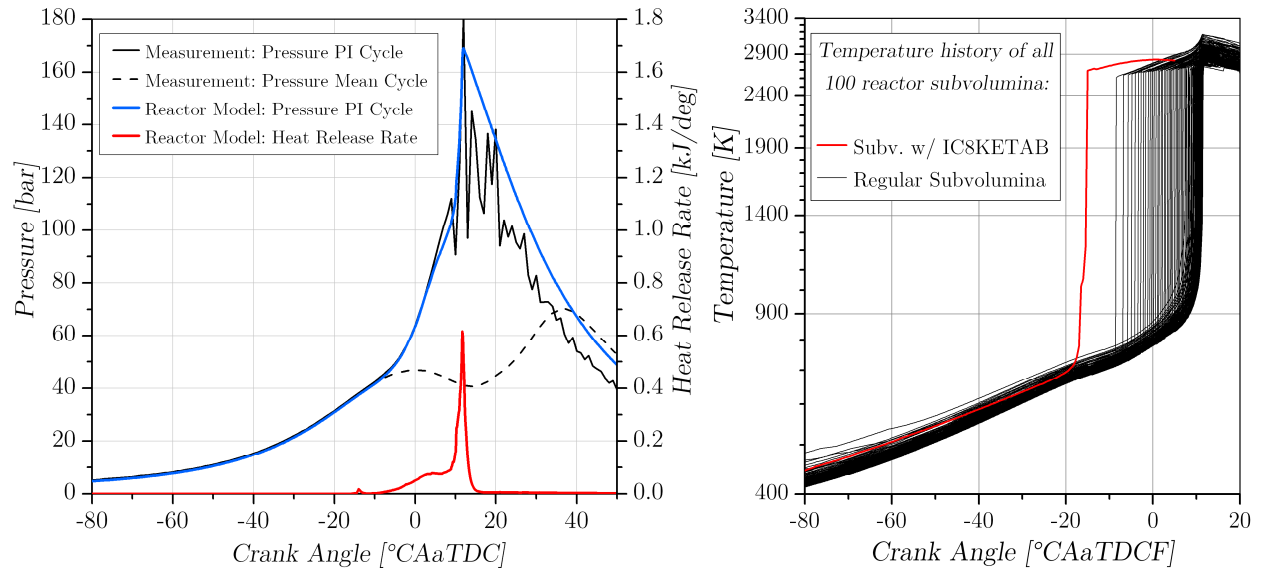


Figure 8.20: *left:* Pressure and heat release for a pre-ignition cycle triggered by a droplet containing reactive octylketohydroperoxide;
right: Temperature history of all stochastic reactor particles - Particle containing the injected droplet showing autoignition is marked red

Compared to the RCM case of Figure 8.19, the ignition delay time is significantly shorter as the autoignition reactions are getting much faster at higher pressures. This is in accordance with the video observations of the first pre-ignition events, where the igniting spot became visible only shortly before the combustion of the entire charge set in. It can be concluded that not exclusively the higher thermal load is critical for downsized engines but rather the higher final compression pressures due to boosting. Moreover, in the right diagram of Figure 8.20 a distinct two-stage ignition cannot be clearly recognized, as the second stage of ignition immediately followed after the first almost without delay. Autoignition can therefore be expected to proceed spontaneously within a few degree-crank-angle at the moment a sufficiently high oil vapour fraction can build up locally.

Figure 8.21 illustrates the dependency of the autoignition timing on the local mass fraction of IC8KETAB in the stochastic reactor. The greatest impact can be stated for the lowest mass fractions below 1E-5. With an increasing seeding level, the autoignition timing asymptotically approaches a value of about -17 °CAaTDC. This can be interpreted as the threshold at which the temperature level of 680 K to 690 K is reached for achieving the necessary activation energy of 180 kJ/mol for the decomposition of IC8KETAB and thus the chain branching step according to R (4.16) in Section 4.1.1. This finding is in exceptionally good agreement with the observations at the test bench, where the earliest pre-ignition events were also found around -17 °CAaTDC, see Figure 5.1 in Section 5.2. The simulation shown in Figure 8.20 was carried out with the highest seeding level of 4.7E-5. The compared measurement data is the earliest pre-ignition event that was observed at the test bench. The correlation of the autoignition timings is a strong indication that reactive components contained in oil or oil additives are likely to initiate pre-ignition.

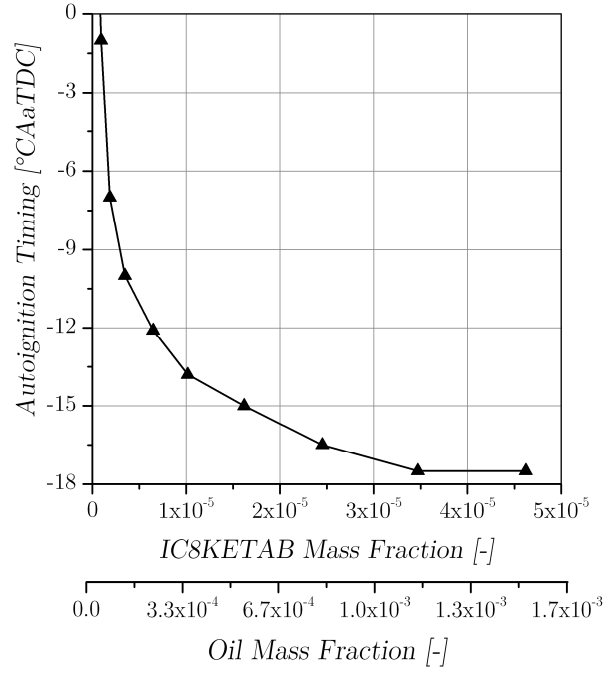


Figure 8.21: Dependency of the pre-ignition timing on the local fraction of IC8KETAB and oil

In Figure 8.21 a second abscissa is plotted to establish the link to the critical oil mass fraction that follows from the radical species fraction according to Eq. (8.3). It can be found that lowest oil fractions of about $1\text{E-}4$ are already sufficient to trigger pre-ignition around TDC. In contrast, comparatively high oil fractions of at least $1\text{E-}3$ are necessary to induce early pre-ignition at $-17\text{ }^{\circ}\text{CAaTDC}$. The higher the local oil content, the more effective is the heat release from the cool flame of the first stage of ignition. In this way, the necessary thermal condition for the onset of the second stage ignition is attained more rapidly and can cause early pre-ignition. Therefore, the lower the local oil fraction available in the combustion chamber, the less pronounced the pre-heating effect of the first ignition stage. Thus, the autoignition process gets increasingly dominated by the high gas temperatures prevailing towards the end of compression what is confirmed in Figure 8.21 by the steep gradient when approaching to TDC.

8.6.2. Critical Droplet Evaporation Behaviour

Up to now, the pre-ignition critical oil vapour was determined from a chemical perspective. In the following, CFD simulations are used to examine influencing factors on the evaporation behaviour of separated droplets inside the combustion chamber and hence on the pre-ignition probability.

In Section 8.3 droplet insertion was already studied with respect to wall film formation and the probability of droplets to survive until TDC. With about 80 %, the vast majority of the drops was shown to form wall film. Nevertheless a small number of air-borne droplets can remain in the charge and is increasingly heated up during compression. Such droplets are the essential basis for pre-ignition but do not necessarily have to result in autoignition critical oil vapour fractions. This will be demonstrated by means of the droplet thermal state. The droplet temperature is a measure of the kinetic energy absorbed by the molecules of the liquid. The higher the energetic state, the higher the probability for molecules at the surface to overcome atomic attraction forces and to vaporize into the gas phase. The loss of high-energy molecules cools the droplet proportional to the mass loss rate and the latent heat of evaporation. Due to thermal contact between the generally cooler droplet and the surrounding, the heat necessary for the phase change is balanced by the convective heat transfer. Thus, the energy conservation equation of an evaporating droplet is given as follows:

$$m_d(t)c_d \frac{\partial T_d(t)}{\partial t} = \underbrace{h(t)A_d(t)(T_a - T_d(t))}_{\text{convective heat flow}} + \underbrace{\frac{\partial m_d(t)}{\partial t} h_{vap,d}(T_d(t))}_{\text{latent heat loss}} \quad (8.4)$$

The heat transfer coefficient h is related to the gas phase heat conductivity λ_a and the Nusselt-number Nu :

$$h(t) = \frac{\lambda_a Nu}{D_d(t)} \quad (8.5)$$

In contrast to the single droplet evaporation studies in quiescent air ($Nu = 2$), inside the combustion chamber relative velocities exist between separated air-borne droplets and the cylinder charge. Hence, convection is expected to enhance the evaporation process of such droplets ($Nu > 2$) and to increase the probability of locally high concentrations of oil vapour. The droplet evaporation model implemented in the CFD code captures the transient heat and mass transfer processes from Eq. (8.4). This allows to determine critical droplet properties and boundary conditions based on the thermal state of the drop. For that reason, droplets were inserted in the crevice region in an analogous manner as was pointed out in Section 8.3. The temperature of the liquid pool captured in the piston crevice was assumed to be dominated by the cooled liner. The initial temperature of separated droplets was therefore specified at 470 K. The formation of droplets is likely to be caused by overlapping stochastic processes, such as the accumulation and mixing of fuel and oil over many cycles and the separation process due to reverse blow-by and high piston ring accelerations. Consequently, the droplet properties might also be distributed stochastically. As a result, a statistical approach was employed to evaluate the impact of the separation timing on the droplet temperature and hence the probability for high oil evaporation rates.

As was argued in Section 8.3, three crank angle positions at 450, 540 and 630 °CAaTDC are most likely for the separation of droplets and are therefore considered in the following. The drop size was divided into ten diameter classes. At release timing, 100 oil droplets were inserted for each diameter class, evenly distributed in crevice regions with intensified wall wetting. As was shown in Figure 8.15, the oil evaporation rates are even more critical the higher the oil content of the separated drop. Therefore, the following simulations are conducted with pure oil droplets to study the worst case scenario. All other droplet properties were randomly defined within suitably chosen ranges as already presented in Figure 8.4. To allow for general statements, the average temperature was calculated from the 100 droplets. Figure 8.22 compares the evolution of the resulting average droplet temperatures of each diameter class. As can be seen, large drops beyond 200 μm are almost not influenced by the varying charge temperature due to their greater thermal mass. If droplets get separated early at 450 °CAaTDC (left diagram) a distinct cooling becomes obvious during the intake stroke proportional to the droplet size. The later droplets enter the charge volume, the less pronounced is the cooling effect as the gas temperature rises rapidly during compression what increasingly heats up the drops.

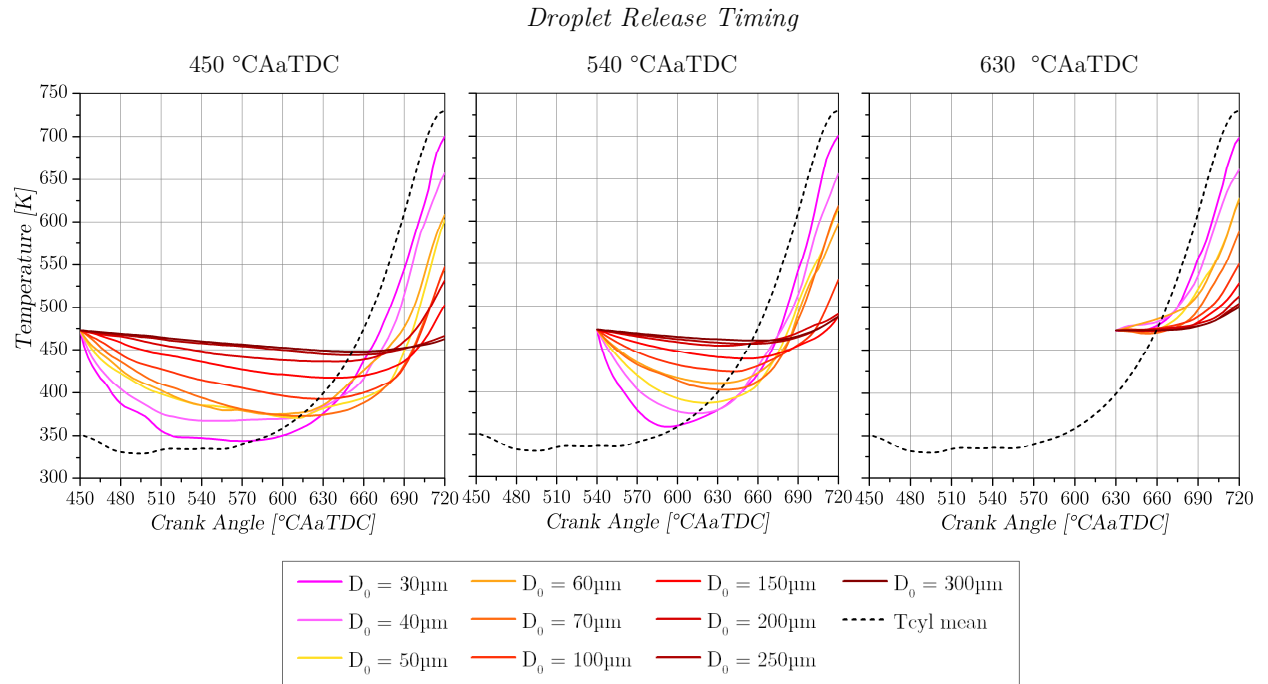


Figure 8.22: Temperature history of oil droplets with different initial diameters shown for three probable release timings; Each line represents the average of 100 droplets per diameter class

A remarkable trend can be found when comparing the drop temperatures at TDC resulting from different release timings. Although the droplets are experiencing distinctly different heat up or cooling phases, the drop temperatures are approaching almost identical values towards TDC independently on the release timing. This suggests that the moment of separation is not of essential importance for the droplet evaporation tendency. In fact, the drop size and the gas temperatures during compression are the determining factors for the droplet thermal state at a potential pre-ignition timing.

As could be shown in the previous section, high local oil fractions can distinctly advance pre-ignition timing what increases the engine damage potential. For air-borne moving droplets the evaporation rate is adopted to quantify the local production of oil vapour as a measure for the pre-ignition probability. In [Figure 8.23](#) the evaporation rate is compared for droplets with different initial diameters. To give an impression of the pre-ignition severity arising from the respective drop diameter, each diagram shows the results of the ten most critical droplets with the greatest evaporation intensities.

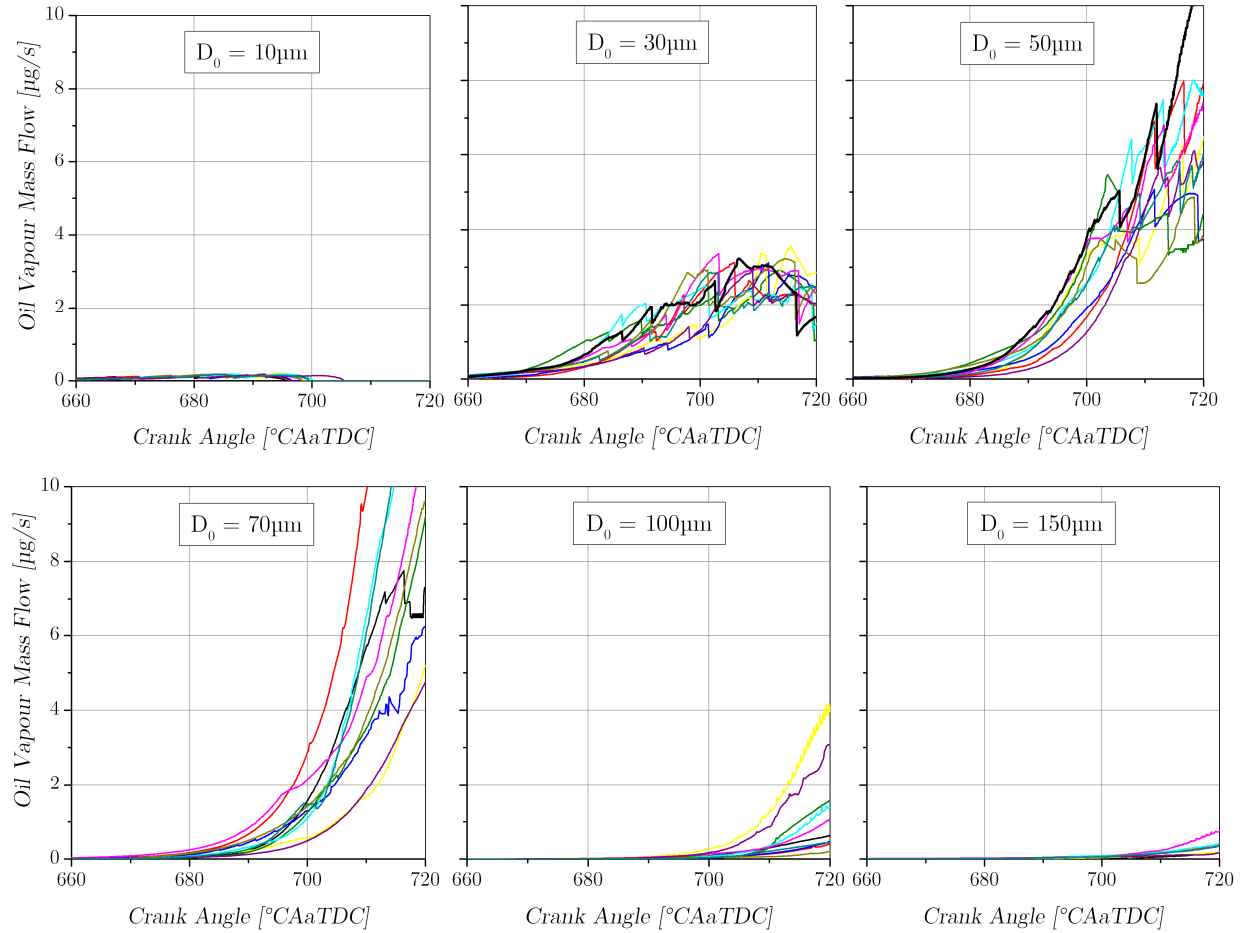


Figure 8.23: Evaporation behaviour of oil droplets towards the end of the compression stroke shown for different initial droplet diameters

Due to the stochastic motion of the drops inside the combustion chamber, the evaporation rates are not consistently smooth throughout the process. Besides the temperature distribution within the charge, strong temperature gradients also exist in the boundary layers close to walls. With decreasing volume during compression, the likelihood increases that droplets approach wall-near zones and experience sudden temperature changes. This becomes especially evident for smaller drop sizes, as they react more rapidly to changes of the local gas temperature.

Interestingly, although small drops were shown in [Figure 8.22](#) to follow the average charge temperature almost instantaneously, the mass of smallest drops with diameters of 10 µm and below is obviously not sufficient to produce a noticeable amount of oil vapour, see upper left diagram in

Figure 8.23. This explains why no relevant impact on the PI-rate was found at the test bench whether the crankcase ventilation was connected to the intake or not. Apparently, oil in the breather gas seems to be uncritical regarding pre-ignition as long as it remains globally dispersed and the contained droplets don't exceed diameters of about 10 – 20 μm .

For larger droplet sizes, Figure 8.23 reveals that the evaporation rate becomes increasingly critical. The evaporation process of a 30 μm droplet, corresponding to the black trace of the top middle diagram in Figure 8.23, is illustrated as image sequence in [Figure 8.24](#).

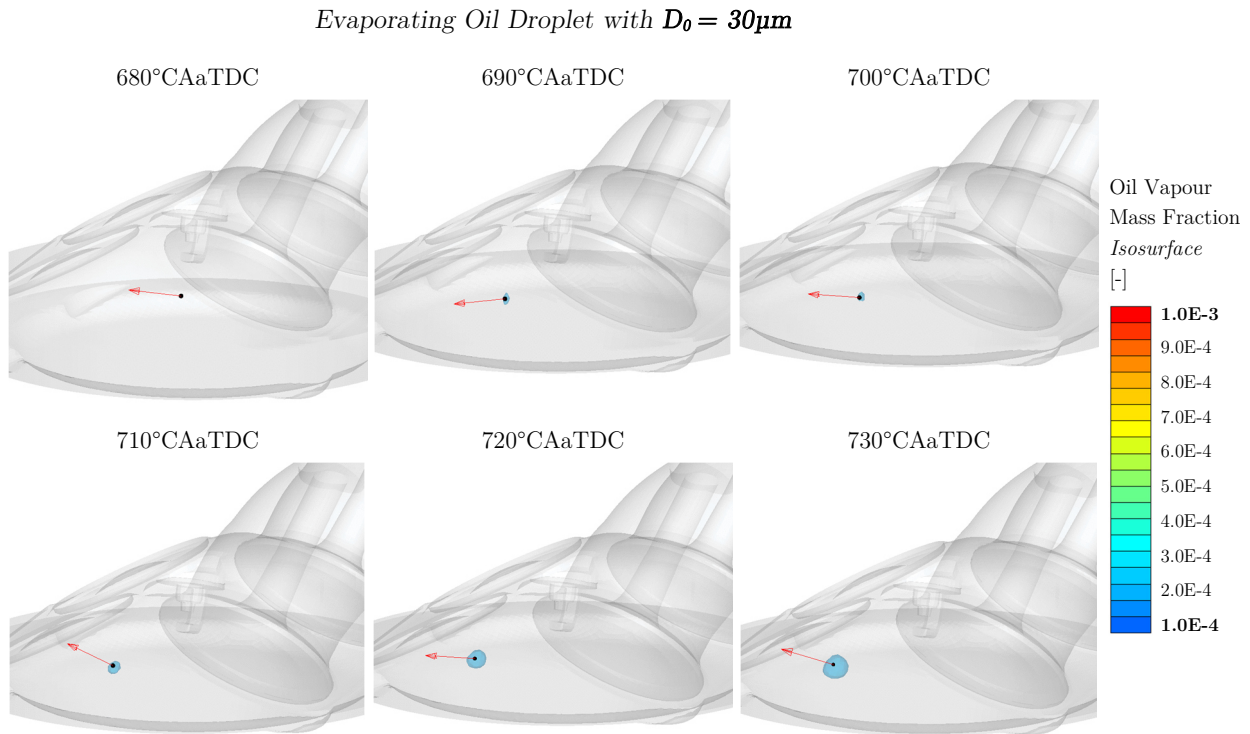


Figure 8.24: Oil vapour plume of an evaporating drop with an initial diameter of 30 μm

According to Figure 8.21 of the previous section, an oil fraction of $1\text{E-}4$ was determined to be at least necessary for pre-ignition at TDC. This value is depicted as isosurface to visualize the oil vapour plume originating from the drop. As can be seen, the isosurface becomes visible the first time at 690 °CAaTDC at an evaporation rate of 0.2 $\mu\text{g/s}$. The rate further increases slightly but falls before reaching TDC because the preceding mass loss was already too severe to allow higher vapour rates. Consequently, for 30 μm drops, pre-ignition is already possible somewhat before TDC, but the limited evaporation rate is insufficient for earlier pre-ignition timings.

When the droplets reach a size of 50 μm , the greater thermal mass slightly retards the initial evaporation compared to the 30 μm case. However, as temperatures are rising during the final compression phase, the evaporation rates rapidly exceed the values of the 30 μm drops already before 700 °CAaTDC. In [Figure 8.25](#) the evaporation process is illustrated for the 50 μm droplet corresponding to the black line in the top right diagram of Figure 8.23. A second isosurface is plotted in red colour to visualize the oil vapour fraction of $1\text{E-}3$ that was identified in Figure 8.21 to be

capable of inducing the earliest observed pre-ignition timings. In contrast to the evaporating 30 μm drop shown in Figure 8.24, a distinct vapour cloud cannot be noticed until 690 °CAaTDC. However, just 10 °CA later at 700 °CAaTDC, a sufficiently amount of oil has evaporated to attain the critical threshold for early pre-ignition. Keeping in mind that ignition delay times were shown in Figure 8.20 to be in the range of several degree-crank-angle under the prevailing pressure conditions, the resulting autoignition timing is in exceptionally good agreement with the test bench observations of the earliest pre-ignition events occurring between 703 – 706 °CAaTDC, see Figure 5.1 in Section 5.2.

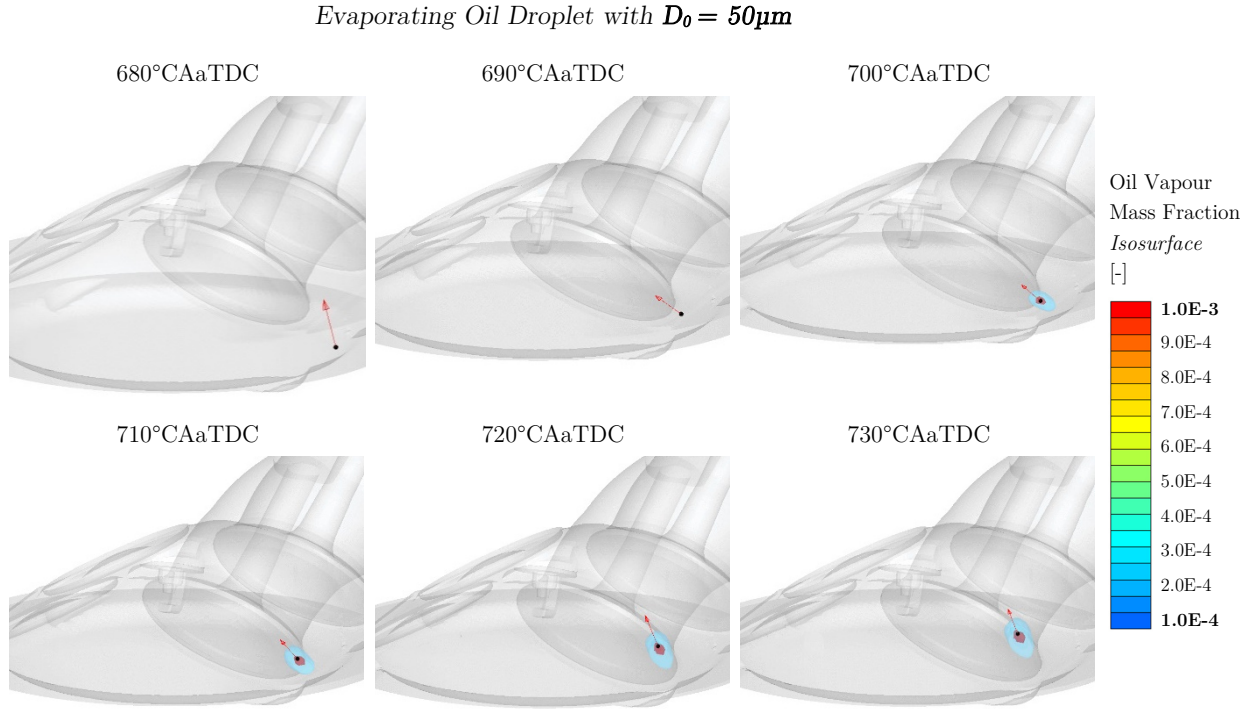


Figure 8.25: Oil vapour plume of an evaporating drop with an initial diameter of 50 μm

From Figure 8.23 follows that comparably high evaporation rates can also be expected for larger droplets, such as for diameters of 70 μm . However, the higher heat capacity of the larger liquid mass increasingly delays the droplet heat-up process and shifts the critical evaporation range closer to or even beyond spark timing. For 100 μm droplets, maximum evaporation rates until TDC are comparable to that of 30 μm drops. Therefore, pre-ignition is also expected to occur rather late around TDC. Hence, it can be concluded that a premature ignition before TDC is critical for drop diameters between 30 and 100 μm , whereas earliest pre-ignition can exclusively be expected for drop sizes in a narrow range around 50 μm . This is the reason why early events are observed extremely rare and a significant rise in pre-ignition tendency is stated towards TDC, as shown by the histogram in Figure 5.1.

Comparing the trajectories and the final positions of the droplets in Figure 8.24 and Figure 8.25, it can be stated that both droplets exhibit PI critical evaporation rates although they pass distinctively different areas. This is in good accordance with the pre-ignition origins observed with optical diagnostics which are shown to spread across the entire combustion chamber, see Figure 5.6.

According to the results from Figure 6.16, at TDC, the temperature at the exhaust side is approximately 60 K hotter than at the intake side. Obviously, the impact of gas temperature inhomogeneities decreases towards TDC. In contrast, temperature gradients in boundary layers close to hot walls seem to have a crucial impact on the droplet heat-up process. In the upper cases, during compression, both droplets remain close to the hot piston crown with a temperature of 520 K until 680 – 690 °CAaTDC where the drops leave the wall near zone and proceed into the centre of the combustion chamber. This is approximately the time at which the mean charge temperature exceeds the piston wall temperature. Hence, it seems that critical drops are effectively pre-heated in the boundary layer and are finally heated by the hot compressed gas what intensifies the evaporation until a pre-ignition critical vapour fraction is reached. A necessary residence time in the boundary layer, however, increases the risk of impingement and wall film formation. Figure 8.7 reveals that the probability of separated drops to survive until TDC is not exceptionally high for PI-critical diameters between 30 and 100 μm what further explains the generally rare occurrence of pre-ignition events.

8.7. Discussion of the Oil Droplet Hypothesis

The conducted simulation work on the evaporation and ignition behaviour of separated droplets provided plausible insights into the pre-ignition process. It could be shown that the evaporation rates of high-boiling lubricating oil droplets can be sufficient during compression to induce autoignition considerably before TDC. Furthermore, resulting pre-ignition timings were calculated with detailed chemical kinetics which were in exceptionally good agreement with test bench observations. However, indications are given in the literature that under certain circumstances other root causes than droplets may be an explanation for initial pre-ignition events. This will be discussed in the following.

8.7.1. Hot Solid Particles

As was already discussed in Section 2.2.2, there are several experimental studies claiming that hot solid particles may play a key role for pre-ignition. Hence, a modelling approach on particle induced ignition was also developed and can be found in [112]. The main outcome is, that similar to the evaporation of oil droplets, a critical range of soot particle sizes is found, for which the temperature can rise sufficiently during a regular burning cycle to exceed the self-ignition limit of soot in the following cycle, see full coloured lines in [Figure 8.26](#).

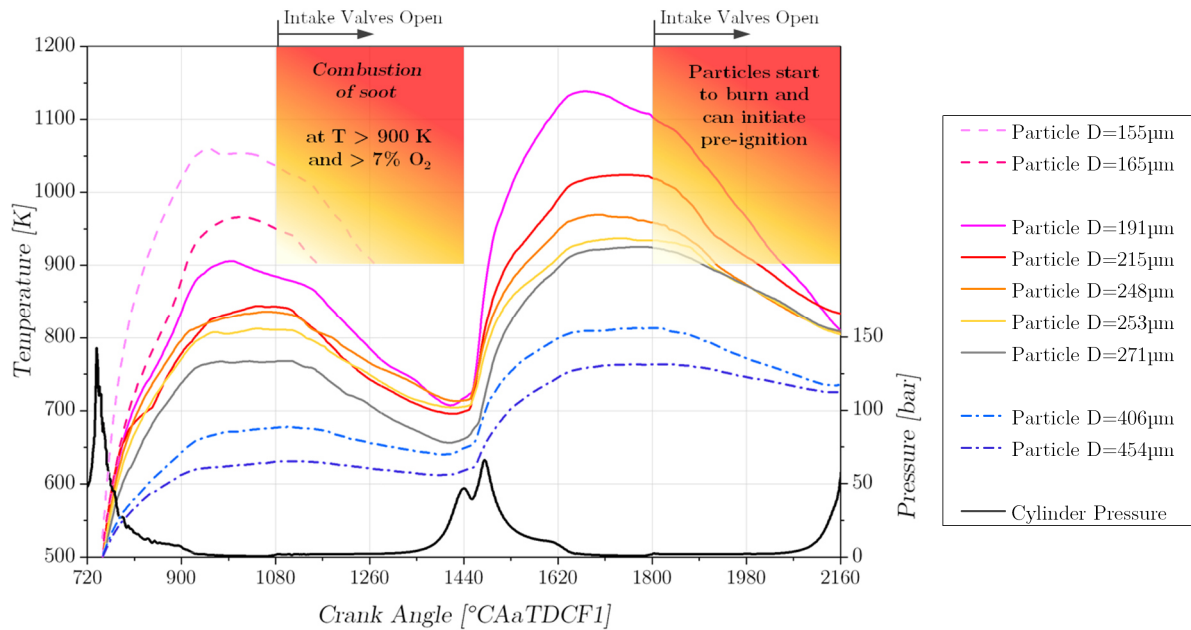


Figure 8.26: Temperature history of soot particles with different sizes [112]

Small particles (dashed lines) are immediately heated and are therefore directly consumed in the hot flame. For large particles (dash-dotted lines), the higher heat capacity prevents a distinct heat-up and consequently inhibits ignition relevant particle temperatures. For the engine used in the present thesis, glowing particles preceding a pre-ignition could only be confirmed with optical diagnostics for follow-up events. Therefore, high pressure peaks as associated with super-knocking

combustion are obviously an essential requirement for detaching deposit flakes from the walls. Nevertheless, if engines exhibit an unfavourable and excessive formation of combustion chamber deposits, the separation of larger particles would become increasingly likely under regular conditions. Thus, initial pre-ignition events induced by particles cannot be fully excluded but appear unlikely for current engines with advanced injection and combustion strategies.

8.7.2. Supercritical Effects

There have been investigations on fuel droplets (n-pentane) burning at high pressures and supercritical conditions [113,114]. It was reported that if the ambient pressure approaches the critical pressure of the fluid, effects like the reduction of the heat of vaporisation become important and the evaporation rate increases, while ignition and combustion time of the fuel droplets decrease. For a better visualization, the phase boundaries of n-heptane as an average hydrocarbon that is representative for gasoline, are depicted in [Figure 8.27](#). The three regimes liquid, vapour and supercritical are labelled in the diagram. In addition, the thermodynamic condition of the charge during compression is plotted as a black line.

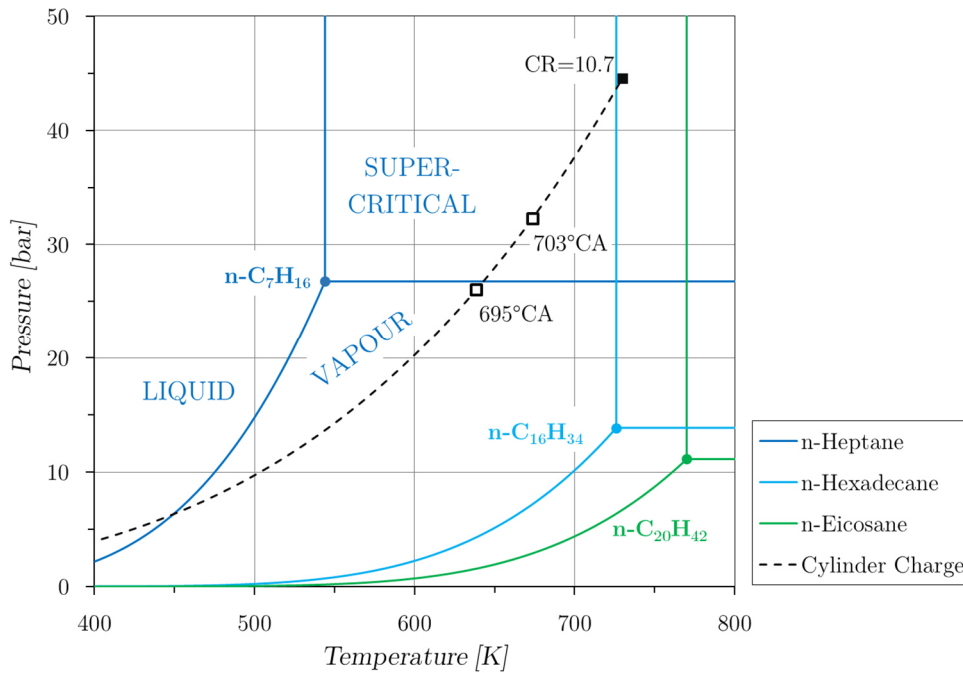


Figure 8.27: Phase diagram shown for n-heptane representing fuel and the long chain hydrocarbons n-hexadecane and n-eicosane standing for the light-end components of oil

It becomes obvious that the mixture exceeds the critical properties of n-heptane towards the end of the compression stroke. Most of the fuel components are located well within the vapour regime during compression what results in high evaporation rates. Fuel drops being exposed to the charge are therefore expected to be removed completely during compression before they can reach the critical state at approximately 695 °CAaTDC. Although no evidence was found in the investigations, a potential source for critical droplets would be a late separation of fuel, possibly due to injector leakage. According to [114], the main reason for an accelerated chemistry under supercritical

conditions is found in the intense mixing of fuel molecules and oxygen. The analyses on fuel reactivity carried out in Section 7.4 assumed an ideal mixing between fuel vapour and air. Even for very rich mixtures around Λ 0.25, what possibly approaches the conditions at a supercritical spot, autoignition of n-heptane didn't occur before TDC, see also Figure 7.10. Taking into account that the used reaction mechanism is experimentally validated by the authors for critical conditions until 1200 K and 50 bar [101], it seems that n-heptane or fuel in general is not reactive enough to explain pre-ignitions distinctly before TDC.

In contrast to fuel, oil was shown to be highly reactive even in extremely low quantities. The phase boundaries of typical light-end components of PCEO oil are given as cyan and green line in Figure 8.27. As can be seen, long-chain alkanes have a lower critical pressure but a substantially higher critical temperature. Therefore, in the present case, the supercritical regime of oil is hardly reached, except for n-hexadecane at the very last moment of compression. In this way, pre-ignition would become more likely around TDC but supercritical effects of oil droplets are also unlikely as reason for early pre-ignition events. Due to a lack of suitable fluid models particularly for mixtures of hydrocarbons, supercritical effects were not considered in the simulations but it should be kept in mind that the high pressures in the combustion chamber could additionally promote the ignition of droplets.

9. Conclusion

Previous work on the pre-ignition phenomenon indicated that the presence of oil or oil-fuel droplets is the most probable explanation for the observed pre-ignition events. It is assumed that impingement of the injected spray on the cylinder liner results in an oil-fuel wall film that collects in the piston crevice volume of the top land during the compression stroke. Obviously, portions of the oil-fuel mixture are released from the top land due to inertia forces acting on the liquid what is further aggravated by the reverse gas flow passing the top ring crevice.

Though attempts have been published about the droplet hypothesis, there is still a lack of knowledge on the particular evaporation and autoignition behaviour of oil droplets inside the combustion chamber. Although a reactive impact was confirmed in standardized experimental studies, a strong uncertainty still exists on the implementation of the complex oil chemistry in numerical approaches.

Therefore, the present work comprises a systematic study of the entire process chain leading to droplet induced pre-ignition. In a first step, endurance test runs were conducted on a turbocharged direct injection spark-ignition engine under pre-ignition critical operating conditions to statistically evaluate the phenomenon. Additionally, high-speed images of pre-ignition events recorded through an endoscopic access were interpreted to describe the spatial characteristics of the ignition processes and to derive an appropriate modelling approach. For that reason, engine process simulation, 3D-CFD simulation and reaction kinetic simulation were combined to account for the physical as well as the chemical processes leading to a premature ignition of the charge. The detailed evaporation behaviour of fuel and oil in the hot cylinder charge was considered by introducing multi-component surrogate fluids for CFD. Due to the obvious importance of wall film regarding pre-ignition, a considerable effort was invested to gain a realistic representation of the fuel impingement process. Critical fuel impingement leading to oil dilution was further analysed in view of a potential separation of oil-fuel droplets. The resulting dispersion of such droplets and their probability to survive until compression-end and to serve as an igniting spot was investigated. An approach was developed to capture the autoignition behaviour of oil with detailed chemical kinetics. A calibration with experimental single droplet studies was conducted to allow statements about the critical oil vapour fraction which was necessary for pre-ignition.

It was confirmed that initial pre-ignitions frequently cause follow-up events. Video observations on pre-ignition series suggested that the first pre-ignition was initiated by oil-fuel droplets while the following events were triggered by hot particles. Obviously, during the first event, deposits were detached from the cylinder walls, which were heated up in the following cycle and finally served as ignition source in the next cycle. Although different root causes could be stated with optical diagnostics, the specific characteristics, such as pre-ignition timing or knock intensity were comparable between initial events and follow-up events. In the literature it is often not distinguished between both types of events what may explains the confusing statements about droplet and particle hypothesis. However, for the studied engine, no evidence was given for particles or glowing objects before any initial event. The main focus of the simulation work was therefore laid on the modelling and validation of oil droplet induced pre-ignition.

The ignition of air-borne droplets requires an appropriate mixture of vapour and oxidiser which usually forms in a certain distance away from the drop surface due to diffusion and convection

processes. The evaporation of oil is therefore a fundamental aspect in the pre-ignition process chain. For that reason, a five component oil model consisting of long-chain hydrocarbons from C16 – C37 was determined with a simplified calculation approach to match the distillation curve of the synthetic PCEO oil that was run in the test engine. The reactive impact of long-chain hydrocarbons was investigated with reaction kinetic simulations. Shortest ignition delay times as experimentally observed for lubricating oil couldn't be attained even with the largest hydrocarbon available in the reaction mechanism. Consequently, somewhat more reactive components included in the oil, such as additives like Calcium, are supposed to accelerate the oil chemistry. The chemical impact of such substances on the oxidation of long-chain hydrocarbons has not yet been sufficiently understood and is, therefore, not available in current reaction mechanisms.

In the present thesis, a novel approach was developed to capture the elevated reactivity of oil with detailed reaction kinetics. Injected droplets were seeded with a stable ketohydroperoxide, which is usually formed by low temperature oxidation processes and is highly reactive already in smallest quantities. The ketohydroperoxide content was calibrated with CFD and reaction kinetic simulations of single oil droplet evaporation and ignition experiments carried out in an RCM. Thus, the link could be established between oil reactivity and the associated fraction of oil vapour. This approach has the clear advantage that the oil chemistry can be approximated using widely available TRF mechanisms without the requirement of detailed reaction kinetics data of the specific oil components. This method was therefore considered as practical for future applications.

The seeding method was further investigated in a stochastic reactor model of the studied test engine to derive the critical oil concentrations necessary for premature ignition. It could be stated that lowest oil fractions of about $1\text{E-}4$ were already sufficient to trigger pre-ignition around TDC. In contrast, oil fractions of at least $1\text{E-}3$ were necessary to induce early pre-ignition at $-17\text{ }^{\circ}\text{CAaTDC}$. An even higher seeding level didn't result in a further advance of the pre-ignition timing. This behaviour was in exceptionally good agreement with the observations at the test bench, because the earliest events were detected at the same time. This additionally justified the adopted seeding approach, as obviously the basic oxidation behaviour of the oil model was comparable with the ignition mechanism in the experiments. Furthermore, the temperature in close proximity to the droplet remained on a low level until exothermic pre-reactions set in rather late, shortly before autoignition. This explained the video observations of the visible short-term ignition sources of the initial pre-ignitions.

All validated models were combined to analyse the evaporation and ignition tendency of oil droplets inside the combustion chamber with CFD. Since the RANS formulation didn't allow for a predictive modelling of the drop separation process from the piston crevice volume, the properties and the motion of virtually inserted droplets were studied to determine the pre-ignition critical parameters. It was shown that trajectory endpoints of droplets which were released from crevice regions with intensified fuel impingement showed a high tendency to lie close to the experimentally observed pre-ignition origins. This confirmed the finding from the literature that the pre-ignition probability increased significantly for injector sprays targeting more at the liner and the piston crevice. Hence, the dilution of the lubricating film with impinging fuel is strongly indicated to be the essential basis for the separation of droplets.

A statistical approach was employed to evaluate the impact of the separation timing on the droplet temperature and hence the probability for high oil evaporation rates. It was shown that the drop temperatures adjusting towards TDC are largely independent on the moment of droplet entrainment. In fact, the drop size and the gas temperatures during compression were shown to be the determining factors for the droplet thermal state at a potential pre-ignition timing. The resulting local oil fractions originating from the evaporating droplet were further evaluated. It was shown that a premature ignition before TDC was most likely for drop diameters between 30 and 100 μm , whereas earliest pre-ignition could exclusively be expected for drop sizes lying close to the critical diameter of 50 μm . This explains why early events are generally observed extremely rare at the test bench and a significantly higher pre-ignition probability is stated towards TDC.

High boost pressures and compression ratios adopted for downsizing concepts severely aggravate the probability for the autoignition of oil. Resulting high compression temperatures facilitate the evaporation of high-boiling lubricant droplets, whereas in addition, high pressures significantly accelerate the oxidation chemistry of oil. Therefore, the performed investigations make clear that oil droplets are the most probable initiation mechanism for initial pre-ignitions.

Many aspects of pre-ignition were observed and modelled to explain the main mechanisms. However, there are still several unknown factors that should be focussed in future research:

- The reactive components included in the oil and their chemical reactions are widely unknown. Although the chemistry of the oil could be appropriately modelled via adding reactive species, knowledge of the basic mechanism would be of highest interest to improve the pre-ignition propensity of future oils without at the same time deteriorating other important oil properties. A filtering of the emitted light to detect intermediate species during the ignition process could be helpful to explain the details of the oil chemistry.
- The used RANS formulation of the CFD simulation provided an average solution of the flow field and the spray. Cyclic variations were not included and therefore their impact on the separation and ignition process of the droplets was not considered. If extensive computational capacities were available, LES simulations would deliver details how drop separation could be effectively avoided. This would require a modelling of the piston crevice volume together with detailed boundary conditions including the gas flow over the piston top ring.
- The exact ignition process was not part of the numerical models due to the lack of enhanced fluid properties. This is particularly important for highly boosted engines where the cylinder charge reaches the critical state of the fluid towards the end of the compression. Supercritical effects of fuel and oil should therefore be further investigated for improved descriptions of the fluid.
- Moreover, the presented method allows for studying the evaporative cooling impact of the fuel contained in oil-fuel droplets inside the cylinder. A critical fuel fraction is expected at which droplet heating and therefore evaporation of highly reactive oil is effectively inhibited.

These should be the next steps for a comprehensive approach to model and to describe the pre-ignition process more accurately in order to realize higher fuel efficiency potentials for future gasoline engines.

10. Bibliography

- [1] Miller, J. D., Façanha, C.: The State of Clean Transport Policy., The International Council on Clean Transportation, Washington (2014).
- [2] Façanha, C., Blumberg, K., Miller, J.: Global Transportation Energy and Climate Roadmap., The International Council on Clean Transportation, Washington (2012).
- [3] Mock, P.: European Vehicle Market Statistics 2014., The International Council On Clean Transportation, Berlin.
- [4] Golloch, R.: Downsizing bei Verbrennungsmotoren. Springer Verlag, Berlin (2005).
- [5] Spicher, U.: Analyse der Effizienz zukünftiger Antriebssysteme für die individuelle Mobilität. In: MTZ (2012), Vol. 2, pp. 98-105.
- [6] Vidmar, K. et al.: Real Driving Emissions – A Challenge for GDI Engines? In: Conference Proceedings of the 8th International Exhaust Gas and Particulate Emissions Forum, pp.176-185, Ludwigsburg (2014).
- [7] Haenel, P. et al.: Systematic approach to analyze and characterize pre-ignition events in turbocharged direct-injected gasoline engines. In: SAE Technical Paper 2011-01-0343.
- [8] Prochazka, G.: Selbstzündungsphänomene bei hochaufgeladenen Ottomotoren - Einflussfaktoren, Wirkmechanismen und Abhilfemaßnahmen. Dissertation, Vienna University of Technology (2007).
- [9] Clerk, D.: The Theory of the Gas Engine. In: Minutes of Proceedings of the Institution of Civil Engineers, Vol. LXIX, London (1882).
- [10] Bobicic, N.: Internal Measurements. Technical report, Institute for Powertrains and Automotive Technology, Vienna University of Technology (2014).

-
- [11] Ricardo, H. R.: Paraffin as a Fuel. In: *The Automotive Engineer*, Vol.9, Nr.2, pp.2-5 (1919).
- [12] Ricardo, H. R.: *The Internal-Combustion Engine Vol II*. Blackie and Son, Bombay and Glasgow (1923).
- [13] Withrow, L., Rassweiler, G.: Slow Motion Shows Knocking and Non-Knocking Explosions. In: *SAE Technical Paper 360126*, 1936, doi:10.4271/360126.
- [14] Miller, C.: Roles of Detonation Waves and Autoignition in Spark-Ignition Engine, Knock as shown by Photographs taken at 40, 000 and 200, 000 Frames per Second. In: *SAE Quarterly Transactions 1947*, Vol. 1, Nr. 1, pp.98-143.
- [15] Ricardo, H. R.: The Progress of the Internal Combustion Engine and its Fuel. In: *Shell Aviation News*, No. 56 (1936), pp. 16-20.
- [16] Sparrow, S. W.: *Fuels for High-Compression Engines*. Rep. No. 232., NACA (1925).
- [17] Grandin, B., Denbratt, I.: The Effect of Knock on Heat Transfer in SI Engines. In: *SAE Technical Paper 2002-01-0238*, 2002, doi:10.4271/2002-01-0238.
- [18] Kapus, P. E., Philipp, H., Fraidl, G. K.: Entwicklungsschwerpunkte für verbrauchoptimierte Otto-Turbomotoren. In: *Proceedings of the 14th Aachen Colloquium*, pp.881-900 (2005).
- [19] Han, K.-M., Sauter, W., Spicher, U.: 3D visualization of spark-ignition combustion: practical examples of flame propagation, abnormal combustion and controlled compression ignition. In: *8th International Symposium on Combustion Diagnostics*, Baden-Baden (2008).
- [20] Vangraefschèpe, F., Zaccardi, J.-M.: Analysis of destructive abnormal combustions appearing at high load and low engine speed on high performance gasoline engines. In: *SIA Conference: The Spark Ignition Engine of the Future*, Strasbourg (2007).
- [21] Zahdeh, A. et al.: Fundamental Approach to Investigate Pre-Ignition in Boosted SI Engines. In: *SAE Technical Paper: 2011-01-0340*.

-
- [22] Kieberger, M.: Untersuchung des Phänomens der Vorentflammung bei der ottomotorischen Verbrennung zur Bestimmung von Einflussfaktoren und von Auslösemechanismen. Dissertation, Vienna University of Technology (2012).
- [23] Hülser, T. et al.: Optical Investigation on the Origin of Pre-Ignition in a Highly Boosted SI Engine Using Bio-Fuels. In: SAE Technical Paper 2013-01-1636, 2013, doi:10.4271/2013-01-1636.
- [24] Günther, M. et al.: Characterization of gasoline biofuels regarding combustion anomalies. In: Proceedings of the 14th Stuttgart International Symposium - Automotive and Engine Technology, pp.417-434 (2013).
- [25] Dahnz, C. ., Schießl, R., Maas, U.: Investigations on Pre-Ignition in Highly Supercharged SI Engines. In: SAE Int. J. Engines 3(1):214-224, 2010, doi:10.4271/2010-01-0355. (2010).
- [26] Palaveev, S. et al.: Premature Flame Initiation in a Turbocharged DISI Engine - Numerical and Experimental Investigations. In: SAE Technical Paper 2013-01-0252.
- [27] Birkigt, A.: Analyse von Vorentflammungsphänomenen an hoch aufgeladenen Ottomotoren mit Direkteinspritzung. Dissertation, Universität Erlangen-Nürnberg (2011).
- [28] Hadler, J., Lensch-Franzen, C., Gohl, M.: Concept for Analysing and Optimising Oil Emission. In: MTZ Worldwide (2014), Vol. 1, pp. 24-29.
- [29] Amann, M., Mehta, D., Alger, T.: Engine Operating Condition and Gasoline Fuel Composition Effects on Low-Speed Pre-Ignition in High-Performance Spark Ignited Gasoline Engines. In: SAE Int. J. Engines 4(1):274-285, 2011, doi:10.4271/2011-01-0342.
- [30] Amann, M. et al.: The Effects of Piston Crevices and Injection Strategy on Low-Speed Pre-Ignition in Boosted SI Engines. In: SAE Int. J. Engines 5(3):1216-1228, 2012, doi:10.4271/2012-01-1148.
- [31] Dec, J. E., Sjöberg, M.: Isolating the Effects of Fuel Chemistry on Combustion Phasing in an HCCI Engine and the Potential of Fuel Stratification for Ignition Control. In: SAE Technical Paper 2004-01-0557, 2004, doi:10.4271/2004-01-0557.

-
- [32] Palaveev, S. et al.: Vorentflammung bei Ottomotoren II. Abschlussbericht FVV Vorhaben Nr. 1051, Heft R566 (2014).
- [33] Yasueda, S., Takasaki, K., Tajima, H.: Abnormal Combustion caused by Lubricating Oil in High BMEP Gas Engines. In: MTZ Industrial (2013), Vol. 3, pp. 34-39.
- [34] Luef, R. et al.: Development of a New Test Procedure to Determine Fuel and Oil Impact on Irregular Combustion Phenomena with Focus on Highly Boosted Downsized S.I. Engines. In: 23rd Aachen Colloquium Automobile and Engine Technology, pp.1169-1204 (2014).
- [35] Takeuchi, K. et al.: Investigation of Engine Oil Effect on Abnormal Combustion in Turbocharged Direct Injection-Spark Ignition Engines. In: SAE Technical Paper: 2012-01-1615.
- [36] Fujimoto, K. et al.: Engine Oil Development for Preventing Pre-Ignition in Turbocharged Gasoline Engine. In: SAE Technical Paper 2014-01-2785.
- [37] Ohtomo, M. et al.: Pre-Ignition of Gasoline-Air Mixture Triggered by a Lubricant Oil Droplet. In: SAE Technical Paper 2014-01-2627.
- [38] Amann, M., Alger, T., Mehta, D.: The Effect of EGR on Low-Speed Pre-Ignition in Boosted SI Engines. In: SAE Int. J. Engines 4(1):235-245, 2011, doi:10.4271/2011-01-0339.
- [39] Withrow, L., Bowditch, F.: Flame Photographs of Autoignition Induced by Combustion-Chamber Deposits. In: SAE Technical Paper 520265, 1952, doi:10.4271/520265.
- [40] Schünemann, E. et al.: Pre-ignition analysis on a turbocharged gasoline engine with direct injection. In: Conference Proceedings on Knocking in Gasoline Engines, pp.380-393, Berlin (2013).
- [41] Okada, Y. et al.: Study of Low-Speed Pre-Ignition in Boosted Spark Ignition Engines. In: SAE Technical Paper 2014-01-1218.

-
- [42] Döhler, A., Pritze, S.: A contribution to better understanding the pre-ignition phenomenon in highly charged internal combustion engines with direct fuel injection. In: Conference Proceedings on Knocking in Gasoline Engines, pp.41-61, Berlin (2013).
- [43] Bae, J. H., Avedisian, C. T.: Experimental study of the combustion dynamics of jet fuel droplets with additives in the absence of convection. In: Combustion and Flame (2004), Vol. 137, pp. 148–162.
- [44] Livengood, J. C., Wu, P. C.: Correlation of autoignition phenomena in internal combustion engines and rapid compression machines. In: Symposium (International) on Combustion (1955), Vol.5(1), pp. 347-356.
- [45] Dahnz, C., Spicher, U.: Irregular combustion in supercharged spark ignition engines - pre-ignition and other phenomena. In: International Journal of Engine Research (2010), Vol. 11, pp. 485-498.
- [46] Stauch, R., Lipp, S., Maas, U.: Detailed numerical simulations of the autoignition of single n-heptane droplets in air. In: Combustion and Flame 145 (2006), Vol. 145, pp. 533-542.
- [47] Westbrook, C. H. et al.: A comprehensive detailed chemical kinetic mechanism for combustion of n-alkane hydrocarbons from n-octane to n-hexadecane. In: Combustion and Flame (2009), Vol.156(1), pp. 181-199.
- [48] Blin-Simiand, N. et al.: Ketohydroperoxides and ignition delay in internal combustion engines. In: Combustion and Flame (1998), Vol. 112(1-2), pp. 278-282.
- [49] Kalghatgi, G. T., Bradley, D.: Pre-ignition and 'super-knock' in turbo-charged spark-ignition engines. In: International Journal of Engine Research (2012), Vol. 13(4), pp. 399-414.
- [50] Glassman, I., Yetter, R. A.: Combustion. Elsevier (2008).
- [51] Pilling, M. J., Compton, R. G., Hancock, G. (eds.): Low-Temperature Combustion and Autoignition. In: Comprehensive Chemical Kinetics Vol. 35. Elsevier, Amsterdam (1997).

-
- [52] Heywood, J. B.: Internal Combustion Engine Fundamentals. McGraw-Hill, New York (1988).
- [53] Peters, N. et al.: Temperature Cross-Over and Non-Thermal Runaway at Two-Stage Ignition of N-Heptane. In: Combustion and Flame (2002), Vol. 128, pp. 38-59.
- [54] Peters, N.: Technische Verbrennung. Lecture Notes, RWTH Aachen, Aachen (2006).
- [55] Westbrook, C. H.: Chemical kinetics of hydrocarbon ignition in practical combustion systems. In: Proceedings of the Combustion Institute (2000), Vol. 28(2), pp. 1563-1577.
- [56] Wijaya, C. D.: Developing Fundamentally Based Models for Autoignition. Dissertation, Massachusetts Institute of Technology (2005).
- [57] Curran, H. J. et al.: A comprehensive modeling study of iso-octane oxidation. In: Combustion and Flame (2002), Vol. 129(3), pp. 253-280.
- [58] Curran, H. J. et al.: A Comprehensive Modeling Study of n-Heptane Oxidation. In: Combustion and Flame (1998), Vol. 114(1-2), pp. 149-177.
- [59] Mohamed, C.: Suppression of reaction during rapid compression and its effect on ignition delay. In: Combustion and Flame (1998), Vol. 112(3), pp. 438-444.
- [60] Minetti, R. et al.: A rapid compression machine investigation of oxidation and auto-ignition of n-Heptane: Measurements and modeling. In: Combustion and Flame (1995), Vol. 102(3), pp. 298-309.
- [61] Warnatz, J., Maas, U., Dibble, R. W.: Technische Verbrennung. Springer Verlag, Berlin Heidelberg (2001).
- [62] Zhao, P., Law, C. K.: The Role of Global and Detailed Kinetics in the First-Stage Ignition Delay. In: Combustion and Flame (2013), Vol. 160(11), pp. 2352-2358.
- [63] Griffiths, J. F., Halford-Maw, P. A., Rose, D. J.: Fundamental features of hydrocarbon autoignition in a rapid compression machine. In: Combustion and Flame (1993), Vol. 95(3), pp. 291-306.

-
- [64] Mohamed, C.: Autoignition of Hydrocarbons in Relation to Engine Knock. PhD thesis, University of Leeds (1997).
- [65] Warnatz, J.: Hydrocarbon oxidation high-temperature chemistry. In: Pure Appl. Chem. (2000), Vol. 72(11), pp. 2101-2110.
- [66] Frohn, A., Roth, N.: Dynamics of Droplets. Springer Verlag, Berlin (2000).
- [67] Chauveau, C. et al.: An experimental study on the droplet vaporization: Effects of heat conduction through the support fiber. In: ILASS Technical Paper 4-1 (2008).
- [68] Godsave, G. A. E.: Studies of the combustion of drops in a fuel spray: The burning of single drops of fuel. In: Fourth Symposium (International) on Combustion (1953), Vol.4(1), pp. 818-830.
- [69] Spalding, D. B.: The combustion of liquid fuels. In: Fourth Symposium (International) on Combustion (1953), Vol.4(1), pp. 847-864.
- [70] Schnaubelt, S.: Numerische Analyse des Selbstzündverhaltens einzelner Brennstofftropfen. Dissertation, Universität Bremen (2005).
- [71] Semenov, N. N.: Chemical Kinetics and Chain Reactions., Oxford University Press (1935).
- [72] Frank-Kamenetskii, D. A.: Diffusion and Heat Exchange in Chemical Kinetics., Princeton University Press (1955).
- [73] Zeldovich, Y. B., Barenblatt, G. I., Librovich, V. B. .: The Mathematical Theory of Combustion and Explosions., Consultants Bureau, New York (1985).
- [74] Metgalchi, M., Keck, J. C.: Burning Velocities of Mixtures of Air with Methanol, Iso-octane, and Indolene at High Pressure and Temperature. In: Combustion and Flame (1982), Vol.48, pp. 191-210.

-
- [75] Damköhler, G.: Der Einfluss der Turbulenz auf die Flammengeschwindigkeit in Gasgemischen. In: Zeitschrift für Elektrochemie (1940), Vol.46, pp. 601-652.
- [76] Pischinger, F. (ed.): Abschlußbericht Sonderforschungsbereich 224 "Motorische Verbrennung"., Aachen (1995).
- [77] Borghi, R.: On the Structure and Morphology of Turbulent Premixed Flames. In Bruno., C., Casci, C., Crocco, L. (eds.): Recent advances in aerospace sciences, New York (1985).
- [78] Abdel-Gayed, R. G., Bradley, D., Lung, F. K.-K.: Combustion regimes and the straining of turbulent premixed flames. In: Combustion and Flame (1989), Vol.76(2), pp. 213-218.
- [79] Bradley, D. et al.: Amplified Pressure Waves During Autoignition: Relevance to CAI Engines. In: SAE Technical Paper 2002-01-2868.
- [80] Zeldovich, Y. B.: Regime classification of an exothermic reaction with nonuniform initial conditions. In: Combustion and Flame (1980), Vol. 39, pp. 211-214.
- [81] Gu, X. J., Emerson, D. R., Bradley, D.: Modes of reaction front propagation from hot spots. In: Combustion and Flame (2003), Vol. 133(1-2), pp. 63-74.
- [82] Lutz, A. E. et al.: Dynamic effects of autoignition centers for hydrogen and C1,2-hydrocarbon fuels. In: Proceedings of the Combustion Institute, Vol. 22, pp.1683-1693 (1988).
- [83] Rudloff, J. et al.: Analysis of pre-ignition in highly charged SI engines: Emphasis on the auto-ignition mode. In: Proceedings of the Combustion Institute (2012), Vol. 34(2), pp. 2959-2967.
- [84] Pan, J., Sheppard, C. G. W.: A Theoretical and Experimental Study of the Modes of End Gas Autoignition Leading to Knock in S. I. Engines. In: SAE Technical Paper 942060.
- [85] Pöschl, M., T., S.: Influence of temperature inhomogeneities on knocking combustion. In: Combustion and Flame (2008), Vol. 153, pp. 562-573.

-
- [86] Reitz, R. D., Diwakar, R.: Effect of drop breakup on fuel sprays. In: SAE Technical Paper 860469 (1986).
- [87] Batteh, J. J., Curtis, E. W.: Modeling Transient Fuel Effects with Alternative Fuels. In: SAE Technical Paper: 2005-01-1127.
- [88] Curtis, E. .: A New Port and Cylinder Wall Wetting Model to Predict Transient Air/Fuel Excursions in a Port Fuel Injected Engine. In: SAE Technical Paper 961186.
- [89] Bai, C., Gosman, A.: Development of Methodology for Spray Impingement Simulation. In: SAE Technical Paper 950283 (1995).
- [90] CD-adapco: Methodology STAR-CD Version 4.18. (2012).
- [91] White, F.: Heat and Mass Transfer. Addison-Wesley (1988).
- [92] Fest-Santini, S.: Wärmeübergang bei der Spraykühlung mit intermittierenden Sprays. Dissertation, Otto-von-Guericke-Universität Magdeburg (2009).
- [93] Wruck, N.: Transientes Sieden von Tropfen beim Wandaufprall. Dissertation, RWTH Aachen (1998).
- [94] Fischer, S.: Simulation of the Urea-Water-Solution Preparation and Ammonia-Homogenization with a Validated CFD-Model for the Optimization of Automotive SCR-Systems. Dissertation, Vienna University of Technology (2012).
- [95] Panão, M. R. O., Moreira, A. L. N.: Thermo- and fluid dynamics characterization of spray cooling with pulsed sprays. In: Experimental Thermal and Fluid Science 11/2005; 30(2), pp.79-96.
- [96] Holly, W.: Untersuchung der Gemischaufbereitung unter Berücksichtigung der Wandfilmbildung im Einlasssystem eines Ottomotors mit Saugrohreinspritzung für ROZ95 und E85. Bachelor Thesis, Vienna University of Technology (2010).

-
- [97] Holly, W.: Reaktionskinetische Analyse der klopfenden Verbrennung an einem aufgeladenen Ottomotor mit Direkteinspritzung. Master thesis, Vienna University of Technology (2012).
- [98] Heiss, M., Lauer, T.: Simulation of the Mixture Preparation for an SI Engine using Multi-Component Fuels. In: STAR Global Conference, Amsterdam (2012).
- [99] Lauer, T., Heiss, M., Klein, M.: Impact of the Wall Film Formation on the Full Load Performance of an Engine Operated with the Ethanol Blend E85. In: SAE Technical Paper: 2011-32-9535.
- [100] cmcl innovations: User manual kinetics & srm engine suite Version v8.2.13., Cambridge (2015).
- [101] Andrae, J. C. G. et al.: Autoignition of toluene reference fuels at high pressures modeled with detailed chemical kinetics. In: Combustion and Flame (2007), Vol.149(1-2), pp. 2-24.
- [102] Andrae, J. C. G. et al.: HCCI experiments with toluene reference fuels modeled by a semidetalled chemical kinetic model. In: Combustion and Flame (2008), Vol. 155(4), pp. 696–712.
- [103] Morgan, N. et al.: Mapping surrogate gasoline compositions into RON/MON space. In: Combustion and Flame (2010), Vol. 157, pp. 1122-1131.
- [104] Klaiß, T.: Selbstzündung und Wärmeübergang an der Klopfgrenze von Ottomotoren. Dissertation, Universität Hannover (2004).
- [105] Heiss, M., Lauer, T., Geringer, B.: A detailed Analysis of Engine Knock Initiation by means of a Stochastic Reactor Model. In: European Congress on Computational Methods in Applied Sciences and Engineering (ECCOMAS), Vienna (2012).
- [106] Heiss, M. et al.: A Detailed Analysis of the Initiation of Abnormal Combustion with Reaction Kinetics and Multi-Cycle Simulation. In: Proceedings of the FISITA 2012 World Automotive Congress, Vol. 190, pp.1007-1018, Beijing (2012).

-
- [107] Fuller, E. N., Giddings, J. G.: A Comparison of Methods for Predicting Gaseous Diffusion Coefficients. In: Journal of Gas Chromatography (1965), Vol.3, Nr. 7, pp. 222-227.
- [108] VDI-Gesellschaft Verfahrenstechnik u. Chemie-Ing.: VDI-Wärmeatlas - Berechnungsblätter für den Wärmeübergang 5. Auflage. VDI-Verlag, Düsseldorf (1988).
- [109] Nomura, H. et al.: Experimental study on high-pressure droplet evaporation using microgravity conditions. In: Proceedings of the 26th Symposium (International) on Combustion, pp.1257-1273 (1996).
- [110] Yuen, M. C., Chen, L. W.: On drag of evaporating liquid droplets. In: Comb. Sci. Tech. (1976), 14, pp. 147-154.
- [111] Magar, M. et al.: Numerical study on the impact of stable intermediates on engine combustion. In: 4th European Combustion Meeting, Vienna (2009).
- [112] Heiss, M., Lauer, T.: Analysis of Pre-ignition Initiation Mechanisms using a Multi Cycle CFD-Simulation. In: International Multidimensional Engine Modeling User's Group Meeting (IMEM), Detroit (2014).
- [113] Shuen, J. S., Yang, V., Hsiao, C. C.: Combustion of Liquid-Fuel Droplets in Supercritical Conditions. In: Combustion and Flame (1992), Vol. 89, pp. 299-319.
- [114] Yang, V.: Modeling of supercritical vaporization, mixing, and combustion processes in liquid-fueled propulsion systems. In: Proceedings of the Combustion Institute, 28, pp.925-942 (2000).

Publications and Conference Contributions

Heiss, M.; Bobicic, N.; Lauer, T.; Pritze, S.: Modellansatz zur Entstehung von Vorentflammungen. In: MTZ - Motortechnische Zeitschrift, Vol. 75, Issue 1 (2014), pp 64-71.

Lauer, T.; **Heiss**, M.; Bobicic, N.; Pritze, S.: A Comprehensive Simulation Approach to Irregular Combustion. In: SAE Technical Paper 2014-01-1214 (2014).

Heiss, M., Lauer, T.: Analysis of Pre-ignition Initiation Mechanisms using a Multi Cycle CFD-Simulation. In: International Multidimensional Engine Modeling User's Group Meeting (IMEM), Detroit (2014).

Heiss, M., Lauer, T.: Analysis of Particle Separation with Respect to Pre-Ignition in an SI-Engine. In: 6th European Conference on Computational Fluid Dynamics (ECFD), Barcelona (2014).

Heiss, M.; Lauer, T.: Investigation on Particle-Induced Pre-Ignitions in an SI Engine. In: STAR Global Conference, Vienna (2014).

Holly, W.; **Heiss**, M.; Bobicic, N.; Lauer, T.; Pritze, S.: Investigation on Knocking Combustion with Reaction Kinetics for a Turbocharged SIDI Engine. In: 4th International Conference on Knocking in Gasoline Engines, Berlin (2013).

Heiss, M.; Bobicic, N.; Lauer, T.: A Detailed Analysis of the Initiation of Abnormal Combustion with Reaction Kinetics and Multi-Cycle Simulation. In: Proceedings of the FISITA 2012 World Automotive Congress, Vol. 190, pp.1007-1018, Beijing (2012).

Heiss, M., Lauer, T., Geringer, B.: A detailed Analysis of Engine Knock Initiation by means of a Stochastic Reactor Model. In: European Congress on Computational Methods in Applied Sciences and Engineering (ECCOMAS), Vienna (2012).

Heiss, M.; Lauer, T.: Simulation of the Mixture Preparation for an SI Engine using Multi-Component Fuels. In: STAR Global Conference, Amsterdam (2012).

Lauer, T., **Heiss**, M., Klein, M.: Impact of the Wall Film Formation on the Full Load Performance of an Engine Operated with the Ethanol Blend E85. In: SAE Technical Paper: 2011-32-9535 (2011).

Lauer, T., **Heiss**, M., Fischer, S.; Klein, M.: Prediction of the Wall Film Formation and Performance of an Engine Operated with the Ethanol Blend E85. In: 13th EAEC European Automotive Congress, Valencia (2011).

Curriculum Vitae

Michael Heiß

Born 29th of March 1984 in Steyr, Austria

Since 09/2015 BMW Steyr, Austria

11/2009 – 09/2015 Vienna University of Technology, Austria: PhD Student and Project Assistant at the Institute for Powertrains and Automotive Technology

10/2004 - 10/2009 Vienna University of Technology, Austria: Studies of Mechanical Engineering (Diploma)

09/1998 - 06/2003 Higher Technical College Steyr (HTL), Austria: Educational Focus on Automotive Engineering (Matura)

09/1994 - 06/1998 Public Monastery Secondary School Seitenstetten, Austria

09/1990 - 06/1994 Primary School St. Peter / Au, Austria